National Library of Canada
Bibliothèque nationale du Canada

Canadian Theses Service
Service des thèses canadiennes

Ottawa, Canada
K1A 0N4

NOTICE

The quality of this microform is heavily dependent upon the quality of the original thesis submitted for microfilming. Every effort has been made to ensure the highest quality of reproduction possible.

If pages are missing, contact the university which granted the degree.

Some pages may have indistinct print especially if the original pages were typed with a poor typewriter ribbon or if the university sent us an inferior photocopy.

Previously copyrighted materials (journal articles, published tests, etc.) are not filmed.

Reproduction in full or in part of this microform is governed by the Canadian Copyright Act, R.S.C. 1970, c. C-30.

AVIS

La qualité de cette microforme dépend grandement de la qualité de la thèse soumise au microfilmage. Nous avons tout fait pour assurer une qualité supérieure de reproduction.

S'il manque des pages, veuillez communiquer avec l'université qui a conféré le grade.

La qualité d'impression de certaines pages peut laisser à désirer, surtout si les pages originales ont été dactylographiées à l'aide d'un ruban usé ou si l'université nous a fait parvenir une photocopie de qualité inférieure.

Les documents qui font déjà l'objet d'un droit d'auteur (articles de revue, tests publiés, etc.) ne sont pas microfilmés.

La reproduction, même partielle, de cette microforme est soumise à la Loi canadienne sur le droit d'auteur, SRC 1970, c. C-30.

NL-339 (r. 88/04)

Canada

THE UNIVERSITY OF ALBERTA

SEISMIC TOMOGRAPHY IN OIL SANDS FOR MONITORING THERMAL RECOVERY PROCESSES .

by

(C) Costas G. Macrides

A THESIS

SUBMITTED TO THE FACULTY OF GRADUATE STUDIES AND RESEARCH

IN PARTIAL FULFILMENT OF THE REQUIREMENTS FOR THE DEGREE

OF DOCTOR OF PHILOSOPHY

IN

GEOPHYSICS

DEPARTMENT OF PHYSICS

EDMONTON, ALBERTA

FALL 1987

Permission has been granted to the National Library of Canada to microfilm this thesis and to lend or sell copies of the film.

The author (copyright owner) has reserved other publication rights, and neither the thesis nor extensive extracts from it may be printed or otherwise reproduced without his/her written permission.

L'autorisation a été accordée à la Bibliothèque nationale du Canada de microfilmer cette thèse et de prêter ou de vendre des exemplaires du film.

L'auteur (titulaire du droit d'auteur) se réserve les autres droits de publication; ni la thèse ni de longs extraits de celle-ci ne doivent être imprimés ou autrement reproduits sans son autorisation écrite.

ISBN 0-315-41032-9

THE UNIVERSITY OF ALBERTA

RELEASE FORM

NAME OF AUTHOR Costas G. Macrides

TITLE OF THESIS SEISMIC TOMOGRAPHY IN OIL SANDS FOR MONITORING THERMAL RECOVERY PROCESSES .

DEGREE FOR WHICH THESIS WAS PRESENTED DOCTOR OF PHILOSOPHY

YEAR THIS DEGREE GRANTED FALL 1987

Permission is hereby granted to THE UNIVERSITY OF ALBERTA LIBRARY to reproduce single copies of this thesis and to lend or sell such copies for private, scholarly or scientific research purposes only.

The author reserves other publication rights, and neither the thesis nor extensive extracts from it may be printed or otherwise reproduced without the author's written permission.

(SIGNED) C. Macrides

PERMANENT ADDRESS:

74-6915 Ranchview Dr.
N.W. Calgary, ALTA
Canada

DATED June 15 1987

We shall not cease from exploration
And the end of all our exploring
Will be to arrive where we started
And know the place for the first time

T.S. Eliot

THE UNIVERSITY OF ALBERTA

FACULTY OF GRADUATE STUDIES AND RESEARCH

The undersigned certify that they have read, and recommend to the Faculty of Graduate Studies and Research, for acceptance, a thesis entitled SEISMIC TOMOGRAPHY IN OIL SANDS FOR MONITORING THERMAL OIL RECOVERY PROCESSES . submitted by Costas G. Macrides in partial fulfilment of the requirements for the degree of DOCTOR OF PHILOSOPHY in GEOPHYSICS.

E. R. Kanasewich

Supervisor

External Examiner

Date May 25 1987

Dedicated to the fond memory of my brother Dimitris

ABSTRACT

Crosshole seismic measurements before and after steam injection were obtained for the purpose of delineating the heated zone within a tar sand reservoir .

Analysis of an initial well-to-well experiment of limited temporal and spatial sampling showed significant changes on seismic character after steam injection. It was possible to amplitude normalize the 'before' and 'after' seismic records by making use of the tube waves. Extensive computer simulation of realistic and carefully designed experimental geometries was carried out assuming a dense tomographic coverage of the area of interest, and a variety of shapes of the heated zone. Before and after steam injection versions of the field experiment are suggested in order to reduce the dimension of the reconstruction problem. Inversion was by solution of an overdetermined system of linear equations. A direct least squares solution provided acceptable results but superior reconstructions were obtained by using a fully constrained algebraic reconstruction approach employing the method of projections. Further improvements were achieved when the above technique was combined with data interpolation and radial smoothing.

In the field tomography experiment, data were acquired with a DFS-V system recording at 2,000 samples/second from a fixed downhole string of 24 hydrophones. The source was a downhole air gun at a pressure of 2300 PSI. Inversion of the data revealed dispersion effects from which the intrinsic

attenuation of the Clearwater was estimated. Independently, attenuation was determined by using the concept of average frequency, and by the spectral ratio method. Q was found to be close to 30. Attenuation was much greater within the heated zone where Q was close to 10. This has been explained in terms of the dramatic increase of permeability in the heated zone as a result of bitumen mobilization. There is some evidence that attenuation increases at frequencies greater than 150 Hz. The Poisson's ratio within the zone was found to be as high as 0.40 . These findings indicate the presence of large amounts of fluids inside the region of the reservoir affected by the steam stimulation. Optimization of recording techniques will certainly allow one to obtain the spatial variation of the Poisson's ratio and perhaps the attenuation.

ACKNOWLEDGEMENTS

I wish to express my sincere thanks to my supervisor Dr. E.R. Kanasewich for channelling my efforts into the exciting area of seismic tomography. His guidance and encouragement throughout my graduate studies have been invaluable.

My very special thanks are due to the Alberta Oil Sands Technology and Research Authority for awarding me the AOSTRA doctoral scholarship. The award greatly enhanced my concentration on the research project during this period of my studies as a Ph.D. student.

I would like to express my appreciation to Esso Resources Canada Limited for the Cold Lake seismic data in the well-to-well experiments. The efforts of Dr. Sube Bharatha together with his technical and scientific expertise and advice were greatly appreciated.

I would like to thank Mr. Charles McCloughan for sharing with me his expertise in computer software matters. His thoughtful advise on numerous other matters is also appreciated.

Last but by no means least, I am grateful to my wife Kathy Vlahos for her continuous support and encouragement throughout my Ph.D. program. Her scientific advice related to her geological expertise is also appreciated.

Table of Contents

Chapter	Page
LIST OF FIGURES	x
I. INTRODUCTION	1
II. CHAPTER 1	5
A. Geology of the Cold Lake Deposits	5
B. Origin of the Oil Sands	11
C. Structure of the Oil Sands	12
D. Engineering aspects of Steam Injection	14
E. The effect of temperature and varying fluid and steam saturations on seismic waves in porous rocks	18
III. CHAPTER 2	23
A. Hole to hole seismic profiling	23
B. Spectral Analysis of the recorded signals	31
C. Computer simulation of the proposed experiments	36
IV. CHAPTER 3	87
A. A Seismic tomography experiment	87
B. Data processing	103
C. Inversion of the presteam data	107
V. CHAPTER 4	118
A. Introduction	118
B. Q measurements from the presteam tomography experiment	118
C. Calculation of Q within the steam zone	128
VI. CONCLUSIONS	137
BIBLIOGRAPHY	142
APPENDIX	151
Index	177

LIST OF FIGURES

Figure		Page
1	Location of the Alberta Oil Sands deposits and their Geology	10
2	Structure of oil sands	13
3	Schematic view of the initial well-to-well before and after steam injection experiment	25
4	The first 300 ms of the before and after steam injection seismic records	27
5	An alternative way of displaying the before and after seismograms."Before" records in blu and above baseline. "After" records in red and below zero amplitude baseline	29
6	The first 900 ms of the before and after steam injection seismic records. D: Tube wave arrivals	30
7	Power spectra of the P-arrivals,before and after steam injection	33
8	Power spectra of the tube waves	35
9	Geometry for a proposed seismic tomography experiment	38
10	Least squares reconstruction of the steam-zone.Assumed P-wave velocity of the steam-zone in the forward calculation was 2.0 km/s	47
11	Steam zone reconstruction obtained by the method of projections	54
12	Reconstruction as in Figure 11 after introducing random noise of ±0.5 ms into the projection data	56
13	Geometry of the proposed experiment as in Figure 9 but with pixel size of 4 meters	58
14	Reconstruction obtained by the method of projections with pixel size of 4 m	61
15	Convergence diagram showing reconstruction	

error E (Euclidean distance) versus number of iterations..... 62

16 Trade-off diagram showing dependence of the reconstruction error upon the constraints imposed on the solution..... 65

17 Ray diagram showing refraction of the seismic rays within the steam-zone according to Snell's law..... 69

18 Reconstruction based on ray bending synthetic data..... 71

19 Ray diagram of the computer simulation also showing the phantom (two ellipses). Pixel size in the grid is 4 m. Rays penetrating the elliptical zones are plotted with yellow color. Nonpenetrating rays are plotted with blue color..... 77

20 a):The phantom used for the computer modeling; b) Reconstruction (20 iterations) based on fully constrained ART..... 79

21 a): Reconstruction after combining ART with smoothing; b): Reconstruction after combining ART with smoothing and data interpolation (10 iterations)..... 81

22 Diagram showing convergence of the Euclidean distance with number of iterations, for reconstruction in Figure 21 b)..... 86

23 Geometry of the Cold Lake well-to-well seismic tomography experiment (in scale) also showing direct ray paths..... 89

24 On site instrumentation for the well-to-well tomography experiment..... 91

25 A typical example of the recorded data up to 250 ms. Source was at a depth of 405.3 m (source #1)..... 95

26 Ray diagram for primary reflected events..... 97

27 Recorded seismograms-up to 700 ms- showing tube wave arrivals (A,B,C,D). a):Source at depth of 405.3 m; b)same as in a) but for source depth of 432.7 m Notice the smaller time interval separating events A,B,C,D..... 101

28 Trace resulting after internal and external

stacking..... 105

29 Cross-correlation of trace in figure 27 with channels 1 to 12 from source #1..... 107

30 Ray diagram of the presteam experiment. Rays of low signal-to noise ratio are not included in the diagram..... 110

31 Inversion of the recorded presteam P-arrivals using ART. A priori sonic log information was incorporated in the solution for the pixels adjacent to the boreholes..... 113

32 Q calculations versus percent anisotropy corrections for Azimi and Futterman attenuation laws..... 117

33 Power spectra and spectral ratios of the P-wave pulses recorded at receivers #1 and #24 from source #1 of the presteam tomography experiment..... 122

34 Downhole pulse average frequency versus shot to receiver distance for source #1 of the presteam tomography experiment..... 127

35 Before and after power spectra of the P-pulses at receivers #1,#2, and their spectral ratios plotted versus frequency..... 131

36 Before and after power spectra of the S-pulses at receiver #2 and their spectral ratios plotted versus frequency..... 136

I. INTRODUCTION

In recent years the importance of the world's large oil sands accumulations, mainly occuring in Canada and Venezuela, is becoming increasingly more clear. These oil sands reserves amount to about 2.5 trillion barrels of oil in place. This is nearly as much heavy oil as the world's total discovered and today rapidly depleting medium and light gravity oil in place.

Remarkable recovery problems can be encountered in these tar sands accumulations as the oil in place has very high viscosity and is practically immobile within the geologic formations of occurrence. Fortunately, the viscosity of oil sands liquids dramatically decreases at temperatures greater than those encountered under reservoir conditions, and one can resort to thermal oil recovery techniques.

Steam injection into heavy oil and tar sands formations has recently become an integral part of thermal oil recovery operations (Farouq Ali,1982). From the reservoir engineering point of view it is quite important to be able to monitor, as accurately as possible, changes that have occured within the reservoir as a result of the stimulation process. In particular, one would like to determine the size, position, and details of shape of the heated zone around the injection well as well as its prefered direction of growth. Information about the distribution of fluids inside the zone is also highly desirable. Diagnosis of the above features

could lead to improved heavy oil extraction techniques and more efficient field operations.

Some theoretical work has been done by Marx and Langenheim (1959) and Mandl and Volek (1969) attempting to evaluate the heated zone volume on the basis of energy balance arguments. However, the proposed theoretical models are based on a number of assumptions which are really oversimplifications compared to true field conditions. This is true even with today's most sophisticated and expensive simulators.

A more promising approach could be the experimental one using remote sensing geophysical methods. The purpose of this thesis is to demonstrate the feasibility of using a seismic imaging technique employing well-to-well measurements for the purposes of monitoring steam injection and production operations. A dense tomographic seismic coverage of the area under investigation is suggested. Seismic sources and receivers are lowered deep into the observation wells, hence interference from the highly attenuating and resolution degrading surface layers is avoided. Unlike the ordinary geophysical inversion problem which seeks to establish a layered model, the main purpose here is high resolution imaging of highly localized anomalies within a model whose average background velocities and position of reflectors are already known to some extent. The method makes use of the unique capability of differential data analysis by comparing seismic data before

and after steam flooding. Particular emphasis is given in examining experimental geometries that are practical in the field and strictly conform to existing geological, operational and economic constraints.

In another technique, Nyland (1982) has demonstrated that it is possible to use the principles of passive seismicity to monitor the advancing front in a fireflood process, by recording microseismic emissions which occur at the thermal front.

Another approach has been suggested by Wood (1986) who makes use of tiltmeter arrays at the surface for in-situ monitoring of enhanced oil recovery processes. His results are quite promising for discriminating between horizontal and vertical fractures and can identify intermediate orientations. However, the depths of the fractured zones can be established with an accuracy of about 15%, at best, and the method cannot provide any useful information about the distribution of fluids within the zones themselves.

In Chapter 1 the foundations are laid by bringing into focus the medium under investigation i.e. the tar sands reservoirs. Basic aspects of their geology and structure are discussed and the current level of understanding of their response to steam stimulation is presented. Finally, the effects of temperature and varying fluid and steam saturations on seismic waves in such media are summarized.

In Chapter 2 the data of a simple before and after steam injection hole-to-hole seismic survey which made use

of a single explosive source are analyzed. On the basis of the results obtained, a seismic tomography experiment is designed and computer simulation of the proposed geometry is carried out, assuming various shapes of the steam zone. An inversion scheme based on an 'algebraic reconstruction technique' is suggested and is discussed in detail.

In Chapter 3 the data of the actual tomography experiment (presteam) are analyzed, and expand on field experimental procedures and difficulties. The collected data are inverted according to the techniques described in Chapter 2, and the intrinsic attenuation of the Clearwater Formation is estimated on the basis of dispersion effects revealed by the results of the inversion.

In chapter 4 the intrinsic P and S-wave attenuation of the steam zone is calculated by employing a spectral ratio approach. Finally, the Poisson's ratio within the zone is determined. The results obtained are synthesized, and conclusions are reached about the nature of the heated zone around the steam injector, at the time of the experiments.

II. CHAPTER 1

A. Geology of the Cold Lake Deposits

The Alberta Oil Sands Deposits have been delineated through the evaluation of data collected on some 10,000 drill holes. They have been categorized according to the geographical area and geological unit of occurence as the Athabasca, Cold Lake, Peace River, and Wabasca Deposits.

'Oil sands' are sands and other rock materials which contain crude bitumen and other associated mineral substances. This definition does not define the type of rock material and suggests that oil sands may be other than clastic sediments and can be loosely interpreted to include a wide variety of high porosity rocks which contain crude bitumen. The large volumes of carbonate reservoirs which contain crude bitumen can then be called oil 'sands'. Crude bitumen is defined as a naturally occuring viscous mixture mainly of hydrocarbons heavier than pentane that may contain sulfur compounds and that, in their naturally occuring viscous state, are not recoverable at an economic rate through primary production. Generally this material has a density of 0.98 g/cm^3 (12^0 API) or heavier. The API gravity of an oil is related to its specific gravity γ_0 according to the formula $\gamma_0 = 141.5/(^0API+131.5)$ where γ_0 is dimensionless.

The Cold Lake Deposits are in east-central Alberta. The crude bitumen deposits of the Cold Lake area are contained within the Lower Cretaceous Mannville Group which has been

subdivided into the McMurray, Clearwater, and Grand Rapids Formations. The sedimentary rocks of the Cretaceous Period are derived from clastic materials generated in the Canadian Shield area lying east of Alberta and the rising highlands of the Cordillera to the west. From these two widely separated source areas the sediments were transported into the Alberta Basin by fluvial (stream) processes where they were deposited in a variety of continental deltaic and marine environments. The Mannville group of the Cold Lake area lies unconformably on the Woodbend or Beaverhill Lake group of the Devonian Period and is overlain disconformably by marine sediments of mid-Cretaceous Period. There is a gentle regional southwesterly dip. The Cold Lake area was close to the southern limits of the lower Cretaceous Boreal Sea transgression, thus deltaic, transitional and near-shore depositional environments are predominant in the Clearwater-Lower Grand Rapids interval, (Carrigy and Cramers, 1975).

The McMurray Formation is an essentially non-marine quartz sandstone of variable thickness. Sands of the McMurray Formation were deposited under fluvial conditions that grade upward into the marine sands of the Clearwater Formation. The deposits within the McMurray are discontinuous. The thickness ranges from 60 metres in the Paleozoic lows to 6 metres over the Paleozoic highs. The formation thins from north to south in the Cold Lake area. The basal McMurray sands are mainly water bearing; however,

the upper thin sands may contain minor amounts of bitumen when adequately structured.

The bituminous sands of the Clearwater Formation are fairly continuous and massive. The formation is gradational in thickness and ranges from 6 metres in the south to over 60 metres in the north. It is also more shaly in the southern parts. When adequately structured, the Clearwater can be entirely oil bearing and free of any underlying water. This reservoir has been the target of most pilot operations in the Cold Lake area to-date. The Clearwater Formation has been interpreted as deltaic in origin. In contrast with the Athabasca sands which consist almost entirely of quartz grains, the Clearwater sands at Cold Lake are of much more complex composition and contain, in addition to quartz, high percentages of feldspar,volcanic rock fragments and chert, as well as some glauconitic members, (Putnam and Pedskalny,1983). This contrast is due to differences in the depositional environments between the two areas. According to Dusseault (1977) the Athabasca oil sands display higher shear strengths. This is the consequence of a high degree of interlock arising from diagenetic alteration of these geologically older quartzose sands. Artificial dense sands and natural, geologically younger sands do not display similarly high shear strengths. Because of diagenesis, porosity is reduced and density is increased. The result may be higher seismic velocities in such media.

In the Cold Lake area the principal depositional facies are: delta-fringe silts and shales, lower delta-front sands and shales and upper delta-front stream-mouth bar and beach sands. The beach sands are further subdivided into proximal and distal depending upon their nearness to distributary systems. Bitumen saturation appears to be closely related to depositional environments. Sediments assigned to the delta-fringe consist mainly of silts and shales. Mean grain size is low (0.10 mm), fines content (silt and clays) is high (15% by weight) and bitumen saturation is low (less than 6% by weight). In sands associated with the lower delta front environment the mean grain size is higher, fines content is lower, and bitumen saturation is higher. The best quality reservoirs are associated with the sands of the upper delta front and beach facies. In these, mean grain size is 0.15-0.20 mm, fines content is less than 4%, and bitumen saturation can be as high as 14%,(Harrison et al.,1981).

The upper and lower Grand Rapids Members are a non-marine sequence of feldspathic sandstones and some thin coal beds. The Grand Rapids Formation sands are marine to deltaic near the base, to fluvial at the top. The combined thickness ranges from 60 metres in the north to 120 metres in the south. Oil accumulation in the formation is more variable than in the Clearwater, and is generally associated with water-bearing sands.

The total Cretaceous in place reserves of crude bitumen in the Alberta Oil Sands are estimated, by the Energy Resource Conservation Board, close to 1400 billion barrels (ERCB,1984). One fourth of these reserves are deemed ultimately recoverable by existing technologies. The Cold Lake reserves are 180 billion barrels mostly contained in the Lower Grand Rapids and in the Clearwater Formation. These estimates are based on a minimum saturation criterion of 3 weight percent bitumen and no significant thickness cut-off. The average bulk saturation in the Cold Lake deposits is 8% and the average porosity is 30%. Permeability varies from 300 to 1300 md. The API gravity of the bitumen ranges from 10-14,(Outtrim and Evans,1977).

Figure 1 shows the location of the oil sands deposits in Alberta and their geology.

In addition, there are some accumulations of crude bitumen in carbonates of the Devonian, Mississippian, and Permian Periods which underlie the Cretaceous accumulations. The crude bitumen bearing formations are composed of varying amounts of dolomitic limestone, occasionally interbedded with argillaceous limestone, siltstones, sandstones and shales. Where crude bitumen saturation occurs, the rock is generally a clean,vuggy dolomitic limestone. However these accumulations have been very sparsely explored as the majority of drilling is conducted for the evaluation of Cretaceous sediments. Few holes have been drilled to penetrate the entire Paleozoic section. Much more research

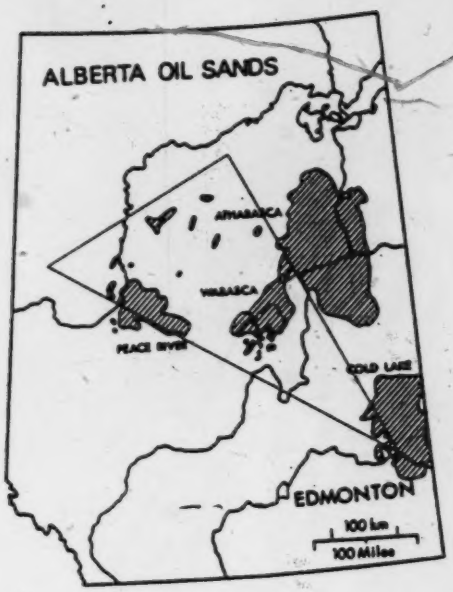

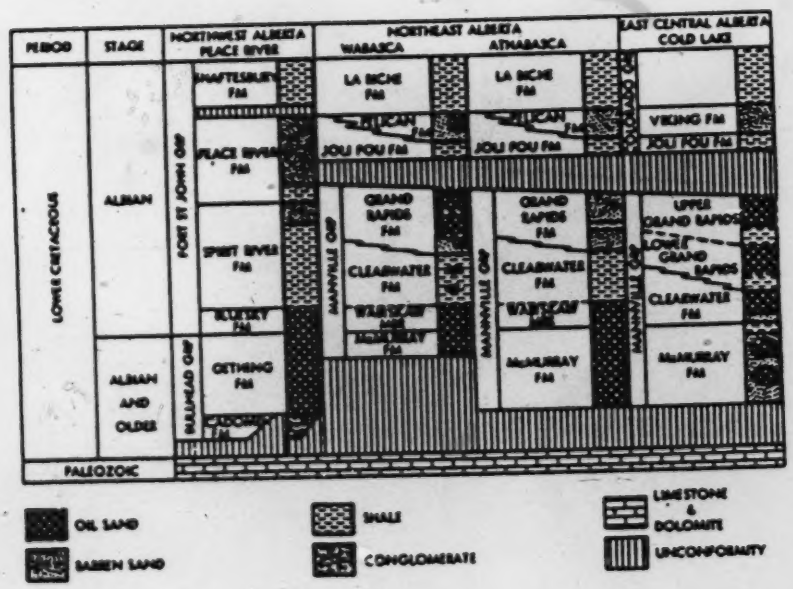

Figure 1.... Location of the Alberta Oil Sands deposits and their Geology. The triangle on the map indicates the location of Carbonate oil sand deposits underlying the Cretaceous tar sands, (modified from Carrigy and Cramers, 1977.)

and field experimentation remains to be done before definitive calculations of recovery are possible on the Paleozoic reserves, but it is believed that some portion of this crude bitumen will ultimately be recovered.

B. Origin of the Oil Sands

The origin of the oil sands has long been a subject of speculation among geologists. The modern concept resulting from major advances in organic geochemistry during the last two decades is that tar accumulations are created by water washing and bacterial degradation of medium gravity crude oils (Bailey et al,1973). Water washing removes the more water soluble light hydrocarbons, especially the aromatics while biodegradation removes preferentially the normal paraffins resulting in an increase in density and sulfur content, the latter being tied to the more bacteria resistant heavy and complex cyclic organic compounds, (Demaison,1977). Common characteristics to all large tar deposits in the world are: 1)their occurence in deltaic or very near shore environments, and 2)the presence of a regional cap, usually a widespread transgressive marine shale overlying the paleo-delta. This cap played an essential role in restraining vertical fluid escape from the basin, thus forcing compaction fluids laterally into the most efficient gathering system present in the basin : the paleo-delta itself. The exception to the deltaic setting is the Siligir deposit in U.S.S.R. which is hosted in Cambrian

carbonates, and the Alberta Carbonate triangle shown in Figure 1.

C. Structure of the Oil Sands

Oil sands may be considered as a four-phase system: a dense interlocked skeleton of predominantly quartz sand grains, with pore spaces occupied by bitumen, water, gas and minor amounts of clay. It is of interest to mention at this point that the results of an experimental study by Han et al. (1986) suggest that both compressional and shear wave velocities decrease with increasing porosity and clay content.

Figure 2 is a diagrammatic representation of a section through a sample of oil sand. The quartz grains are generally hydrophyllic and are surrounded by a thin film of water. The bitumen occupies a portion of the pore space but does not contact directly the quartz grains. Typical Alberta oil sand porosity is 32% with tar saturation 81% and water saturation 19%. The grain density is 2.7 g/cm^3. The bulk density is 2.1g/cm^3. The bitumen in the Alberta oil sands reservoirs is immobile and from a hydrological point of view can be considered as part of the skeleton, because it reduces the permeability of the formation to water by a factor of 100 with respect to the permeability of clean sands similar to the McMurray Formation, (Harris and Sobkowicz,1977). The viscosity of the Cold Lake bitumen is about 100,000 cp, under reservoir conditions (12^{0}C). This

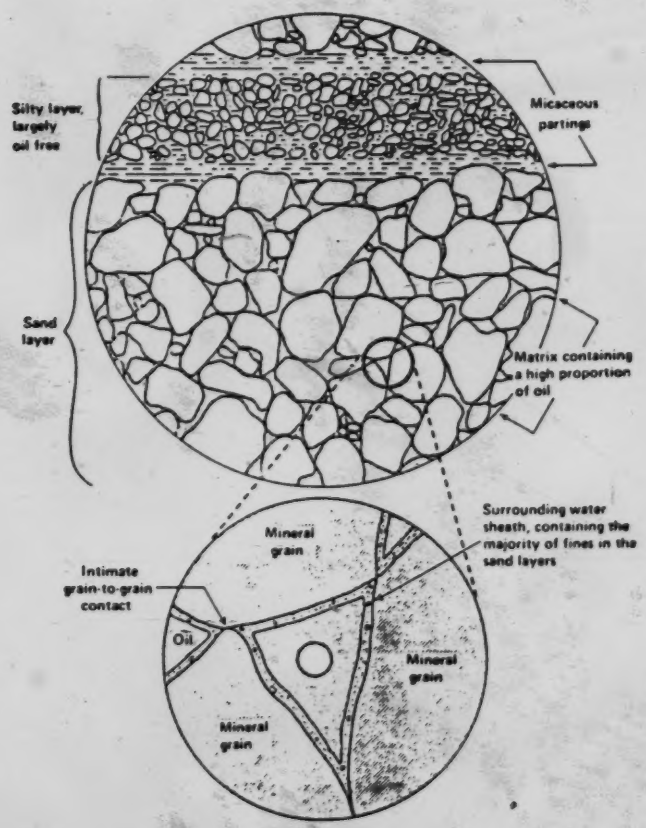

Figure 2.... Structure of oil sands, (after Harris and Sobkowicz (1977) and Dusseault, 1977

drops to less than 10 cp at a temperature of 220°C, (Flock and Lee, 1977).

D. Engineering aspects of Steam Injection

Only 8% of the total in place reserves of oil sands in Alberta are considered suitable for economic surface mining, (Nicholls and Luhning, 1977). The surface mineable reserves are covered by less than 150 feet of overburden and are all located within the Athabasca deposit. The remaining in place bitumen which has more than 500 feet of overburden must be recovered by in situ methods. In order to recover the bitumen by an in situ method, it is necessary to reduce its viscosity in order to mobilize it so that it will flow to the producing well bore. Research into methods for recovering bitumen from the Alberta Oil Sands by in situ methods began in the late 1950's. Today there are several active in situ pilot plants in Alberta. Most of them are located in the Cold Lake area. The main operators are Gulf, Chevron, BP, Esso Resources, and Shell. The principal thermal recovery methods employed are based upon steam injection ,the two basic forms of which are cyclic steam stimulation and steam flooding .In situ combustion has also been considered and tested.

Cyclic steam stimulation (steam soak or huff n' puff) is the most widely used steam injection method for heavy oil recovery at the present time. This popularity derives from the relative ease of application of the method, low initial

investment and quick return. According to this method, steam is injected into a well at the highest possible rate (in order to minimize heat losses) for several weeks. The injected steam heats the rock and the fluids around the wellbore. Vertical inhomogeneities such as shale barriers, cause only partial vertical sweep while maintaining a radial advance of the fluids in the zone that is contacted. These barriers result from clay lamellae that are deposited in cyclic sequences in deltaic deposits (shallow marine) which are common to the Grand Rapids and Clearwater Formations,(Outtrim and Evans, 1977). After injecting the desired volume of steam, the well may be shut in for about two weeks. This is called the 'soak' period. The reasons normally given for soaking a well are to condense steam thus allowing additional conductive heating and also to achieve even distribution of the injected heat. Finally the well is depressured and oil and other fluids are expelled into the same wellbore which may be pumped off. The greater the reservoir presssure the higher the rate of the oil production will be. The production period typically lasts several months. The cycle is then repeated.

Steamflooding or continuous steam injection involves a multiple-well pattern consisting of a center steam injector and several (usually four) corner producers. Steamflooding is recommended when reservoir pressure is low and steam injectivity high, pointing to high permeability, small formations, (Farouq Ali,1982). Steamflooding is more

expensive and time-consuming than cyclic steam stimulation. The principal advantage of a steamflood is the large areal sweep efficiency which is unattainable in steam stimulation. Today, cyclic steam stimulation is regarded as the first stage in steam-flooding.

The following mechanisms take place when high temperature (250°C) steam is injected into the formation at pressures equal or even greater to the formation pressure:

The rising temperature near the well vaporizes the distillable components out of the oil. The steam then carries these lighter components further into the reservoir, which condense because of a drop in temperature, (Coats and Ramesh,1977). As a result, hot and highly mobilized oil is displaced away from the well to create an increase in oil saturation -(an oil bank) ahead of the steam zone. In addition, some of the steam condenses because of loss of heat to the oil and the rock, (Finbow and Koop,1977). The final picture is a steam zone, approximately at a constant temperature Ts, characterized by a reduced oil saturation (residual saturation) of about 15%, typically. Outside the steam zone, temperature drops with radial distance away from the well within a zone characterized by high concentration of water (steam condensate) and oil. Outside this region normal reservoir conditions are encountered. Typically, Ts (saturation temperature) is 280°C corresponding to a pressure of 1,000 PSI within the steam zone. The above model has been well documented by experimental investigations in

the laboratory (for example, Flock and Lee,1977). Notice that the extent of the steam zone can be calculated using the Marx Langenheim or the Mandl-Volek model. The calculation, for typical Cold Lake conditions is presented in the appendix. The model assumes a cylindrically shaped and radially symmetric steam zone around the injection well. While the model is known to give reasonable steam growth approximate values, the precise shape, position, and volume of the zone in actual field operations remain uncertain.

Invasive techniques (drilling observation wells around the injection well) can provide some information about the heated zone. However, high cost and limited spatial resolution are the obvious limitations of these techniques. Furthermore, the drilling fluids circulating within the observation wells are known to alter the conditions of the medium in the immediate vicinity of the well. The result is that the obtained measurements are not believed to give an accurate representation of the changes that have occured within the reservoir.

It is becoming increasingly more clear that non-invasive methods, i.e. remote sensing geophysical techniques, should be employed for monitoring such changes during enhanced oil recovery (EOR) operations. The use of seismic waves for such purposes appears to be a strong candidate for two reasons: 1)high resolution attainable by a broadband source, and 2)the sensitivity of seismic velocities and amplitudes to changes in rock properties,

particularly the replacement of oil or water by gas or steam.

E. The effect of temperature and varying fluid and steam saturations on seismic waves in porous rocks

The basis for proposing the use of seismic waves as a tool in reservoir monitoring during thermal recovery operations is the large amount of laboratory measurements of seismic velocities and attenuation in core samples from a wide variety of reservoir rocks. The basic findings of these efforts are reviewed here.

Compressional wave velocity $-V_p-$ is nearly constant (decreases slightly) from zero water (or oil) saturation to a saturation of approximately 90% above which the velocity increases abruptly, (Domenico, 1976). In contrast, shear wave velocity $-V_s-$ continues to decrease at fluid saturations higher than 90% because of the increase in the bulk density and the indepenence of the shear modulus on the degree of saturation, $(V_s=(\mu/\rho)^{1/2})$. The reason for the behavior of V_p is the stiffening, at complete saturation, of the pore space by a relatively incompressible pore fluid such as water or oil. In contrast, the presence in the pore space of even a small fraction (10%) of a very compressible phase such as gas or steam, causes the rock as a whole to be more compressible. This results in a marked decrease of V_p. V_p is proportional, among other parameters, to the square root of the incompressibility of the rock k:

$$V_p = \{(k+4/3\mu)/\rho\}^{1/2}.$$

The drop in V_p decreases with depth (Gardner, 1974). This velocity contrast between sands containing gas, and sands saturated with oil or water is responsible for the observation of high amplitude reflections-'bright spots'-at interfaces bounding such media. The bright spot technique has been successfully used by geophysicists since the early 1970's for direct detection of hydrocarbon accumulations (Dobrin, 1976).

Seismic attenuation (Q_p^{-1} and Q_s^{-1}) follows a similar pattern. Q is a measure of the intrinsic attenuation and is defined as

$$Q = 2\pi E/\Delta E$$

where ΔE is the energy dissipated per wave cycle and E is the total elastic energy of a wave cycle. Fluid flow within the pore spaces under seismic excitation is believed to play an important role in controlling the attenuation of seismic waves in rocks with partially saturated cracks or pores. Both Q_p^{-1} and Q_s^{-1} increase with increasing fluid saturation. At saturation higher than 90%, attenuation dramatically decreases for P-waves while Q_s^{-1} continues to increase uniformly, (Mavko and Nur, 1979) . The attenuation is found to be extremely sensitive to the aspect ratios of the pores with flatter pores resulting in higher attenuation. It seems that pores with aspect ratios around 10^{-4} dominate the dissipation even though these pores may be a relatively small percentage of total porosity (Palmer and Traviolia,

1980). Smaller aspect ratios do exist but due to electrochemical effects they do not contribute to attenuation. At complete saturation, squirting flow between interconnected pores is claimed to be the dominant cause of attenuation, (O'Connel and Budiansky, 1977). The implication, in this case, is that there is a direct link between permeability and attenuation, higher permeability resulting in higher attenuation. Furthermore, attenuation for both P and S waves decreases with effective pressure presumably due to crack closure, (Nur et al., 1980).

A large body of evidence suggests that Q for solids is frequency independent in seismic frequencies. Q for liquids varies as w^{-1} (Nyland, 1985). To obtain the effect of attenuation on a wave solution such as $\exp\{i(kx-wt)\}$ one can replace k by a complex-valued wavenumber K. Then

$$K=w/v(w)+ia(w).$$

Then, the principle of causality and Kramers-Kronig relations suggest that Q cannot be constant over all frequencies. Hence one must tolerate a frequency-dependent Q with an attenuation factor a(w) chosen to make Q effectively constant over the seismic frequency range. A popular law is

$$a(w)=a_0 w/(1+a_1 w)$$

where $a_1 w$ is much smaller than 1 for all seismic frequencies. The above arguments are strictly mathematical. One can further constrain the problem by considering physics and add the concept of a Boltzmann creep function. Kjartansson (1979) presented a linear model for attenuation

with Q exactly independent of frequency using Boltzmann's superposition principle. His model is causal since the creep function he used vanishes for negative times. Liu et al. (1976) have shown that a superposition of different creep mechanisms with different relaxation peaks gives an effectively constant Q over seismic frequencies. However, if there is a single relaxation time or a very narrow distribution of relaxation times , viscoelasticity theory predicts that, for a linear solid, a plot of Q^{-1} versus frequency will appear very similar to a Zener or Debye peak. Laboratory measurements showing such a resonance-like frequency dependence of Q have been carried out by Jones and Nur (1983). The pore fluid was water in their experiments. Their results may indicate that only a narrow range of pore aspect ratios are responsible for the attenuation.

Tosaya et al. (1984) conducted an extensive laboratory study on a number of tar sands samples in order to determine the effect of elevated temperatures and varying bitumen content on seismic velocities. The results indicate that at high temperatures the magnitude of the drop in V_p appears to be qualitatively related to the decrease in oil viscosity with temperature. For instance, the drop in V_p for an Athabasca tar sand sample at 200^0C was 70%, compared to a base temperature of 20^0 but for a tar sample with characteristics similar to Cold Lake conditions the drop was between 20% and 30%. It should be noted that viscosities of both the Athabasca and Cold Lake bitumen drop to about 10 cp

at 200°C but at initial reservoir conditions the viscosity of the Athabasca bitumen is about ten times greater.

Furthermore, the temperature dependence of the drop in compressional velocities was proportional to bitumen content. At zero bitumen content there was no dependence of seismic velocity on temperature for the range considered (20 to 200°C). Dependence was maximum at 100% bitumen saturation and intermediate at lower saturations.

III. CHAPTER 2

A. Hole to hole seismic profiling

An initial seismic experiment was carried out in the Cold Lake area at the end of 1982 and is schematically shown in Figure 3. The experiment was under the supervision of Dr. Sube Bharatha of Esso Resources Research Department. The two wells were deviated from the vertical so the experiment was not confined to a vertical plane. The bottom hole separation of the two wells was 200 m. The seismic source was 100 grams of Primacord charge, shot repeatedly at a fixed depth of 440 m, within the source well, for various positions of a receiver. The receiver was a well-locking vertical component seismometer positioned at true vertical depths ranging from 372 to 457 m within the receiver well.

The recording was carried out by an independent contractor (Schlumberger) and the data was later supplied to the seismology laboratory of the University of Alberta for analysis and interpretation. The bottom hole location of the injection well was mid-way between the source and receiver well. Steam was injected in the Clearwater formation whose top and bottom were at 415 m and 465 m respectively. According to the sonic logs the Clearwater Formation had the same velocity as the formation above (Grand Rapids) hence no refraction of the seismic rays is expected to occur at the interface. The perforations were at depths between 442 m and 450 m as indicated in Figure 3 by the small horizontal

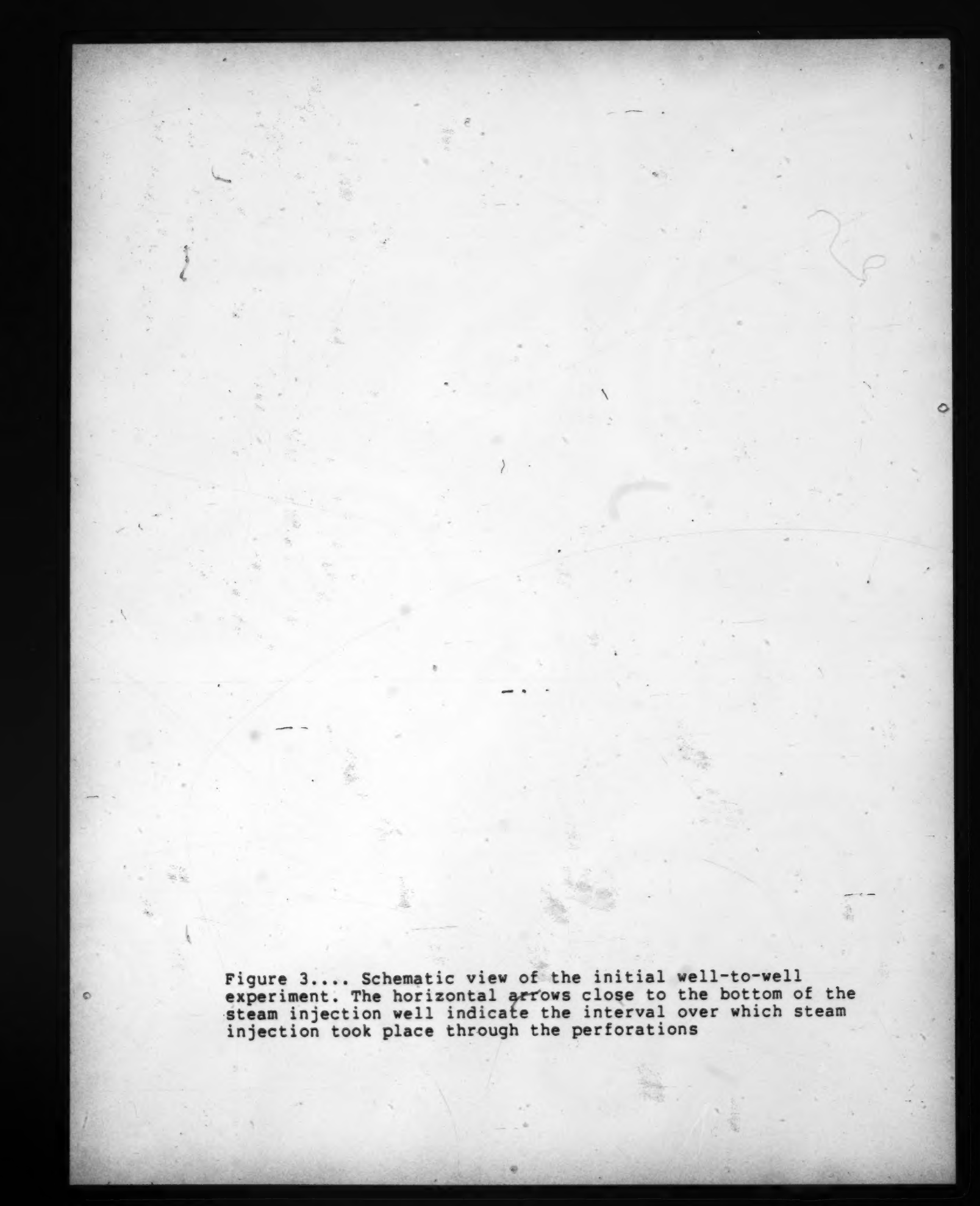

Figure 3.... Schematic view of the initial well-to-well experiment. The horizontal arrows close to the bottom of the steam injection well indicate the interval over which steam injection took place through the perforations

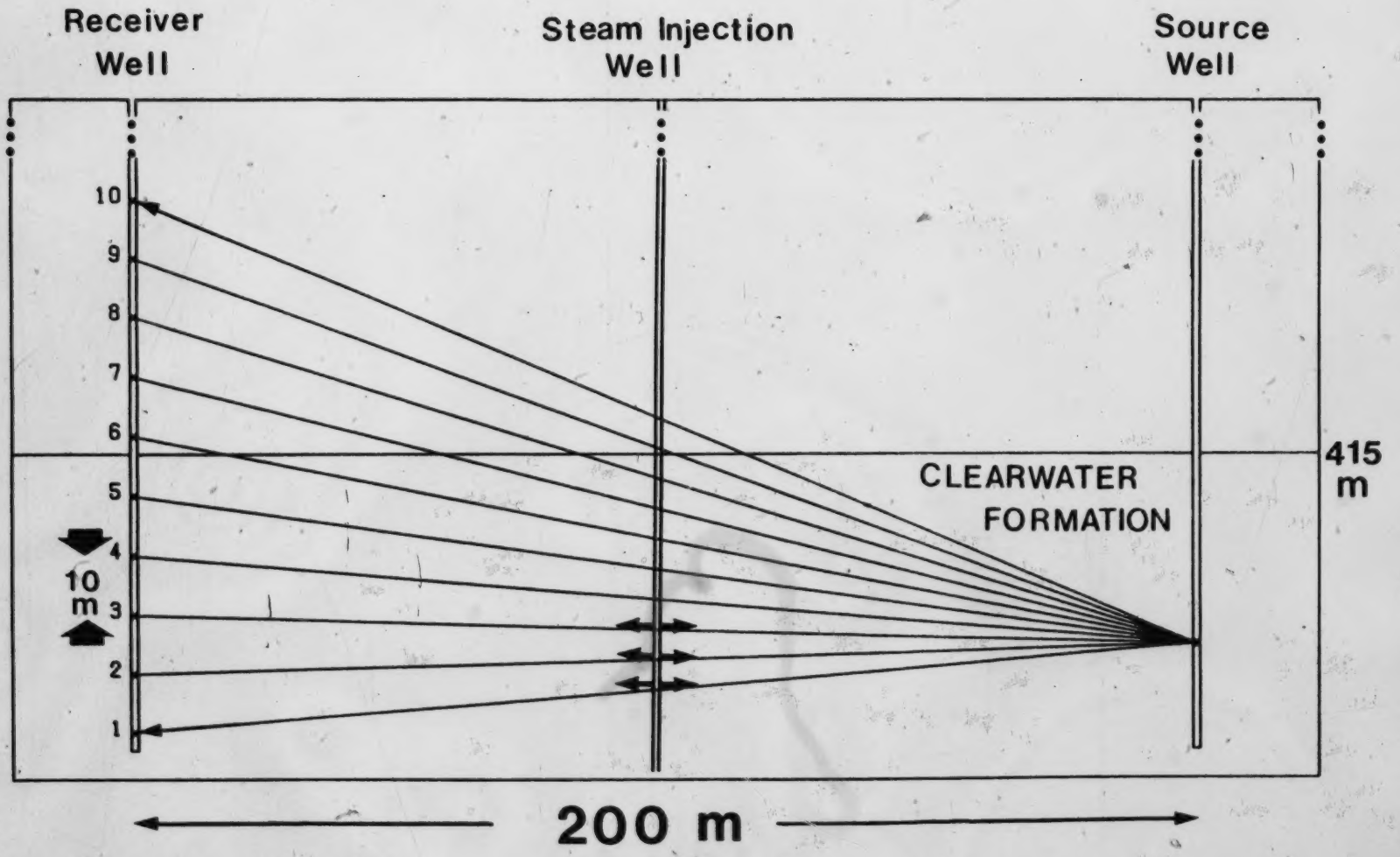
Receiver Well
Steam Injection Well
Source Well
10
9
8
7
6
5
4
3
2
1
10 m
CLEARWATER FORMATION
415 m
200 m

arrows close to the bottom of the injection well. The sampling rate of the seismic recording was 1,000 Hz. The experiment was conducted twice: once before steam injection and once again (in an identical manner) after injecting 10,100 m^3 of water equivalent of steam at a pressure of 10 Mpa, for a total of 48 days. The first 300 ms of the seismic records of both experiments, superimposed on each other, are shown in Figure 4.

An alternative way of displaying these records is suggested in Figure 5 The seismic signals are rectified in such a way as to allow plotting the 'before' records (blue color) entirely above the zero amplitude baseline and the 'after' records (red color) entirely below it.

Figure 6 shows the first 900 ms of the seismic signals to include the tube wave arrivals. Comparison of the records shows substantial similarity between the before and after injection recorded signals for the upper five receivers, indicating that probably the associated seismic rays had not encountered the steam invaded zone. This is not the case for the bottom five records which show significant amplitude changes after the injection . Notice, in these records, (figures 4 and 5) the very low amplitudes of the S-waves after injection. Furthermore there are time delays of up to 2 ms on the P-arrivals after the injection. The P-wave seismic velocity V_p within the reservoir is 2.4 km/s. This information was obtained from the P-wave arrival times of the "before" records. The sonic logs indicate zero velocity

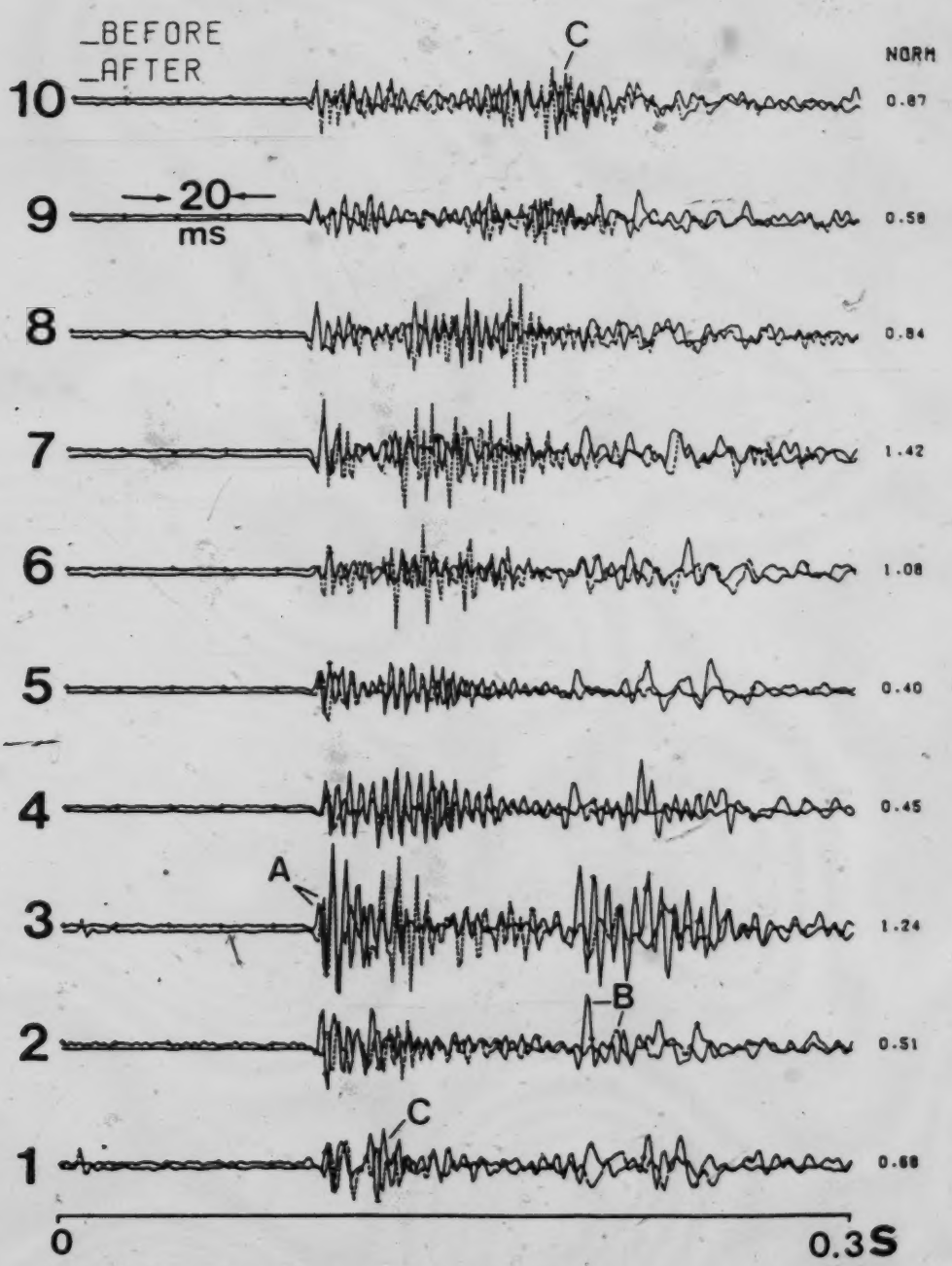

Figure 4.... The first 300 ms of the before and after steam injection seismic records. A: P-arrivals, B: S-arrivals, C: Reflection from the top of the Paleozoic. Before records with solid line . After records with dashed line.

Figure 5.... An alternative way of displaying the before and after seismograms. The seismic signals are rectified in such a way as to allow plotting the 'before' records (blue color) entirely above the zero amplitude baseline and the 'after' records (red color) entirely below it.

FSSO Cold Lake Hole to Hole Experiment 1982

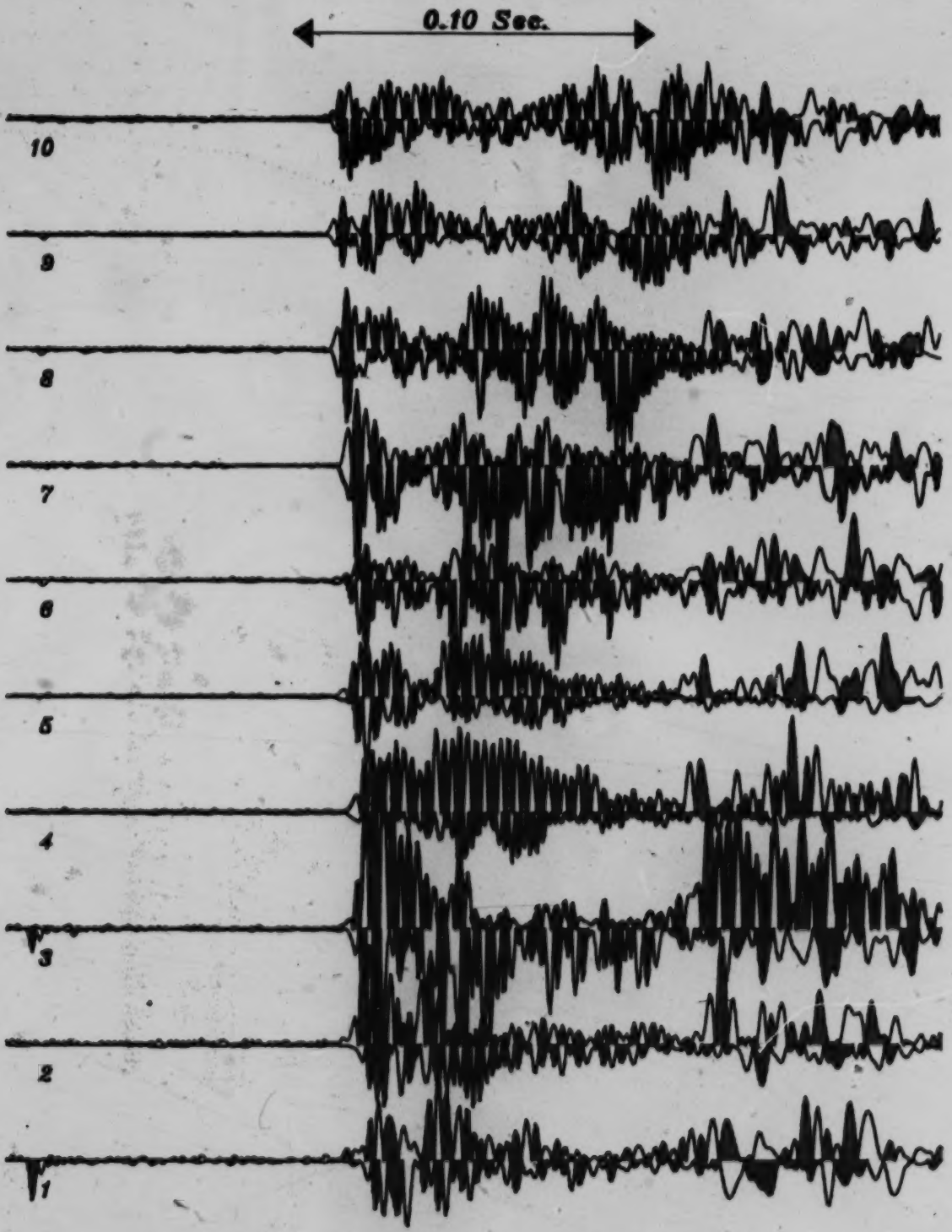

Pre steam : In blue and above baseline
Post steam : In red and below baseline
Original positive regions shaded

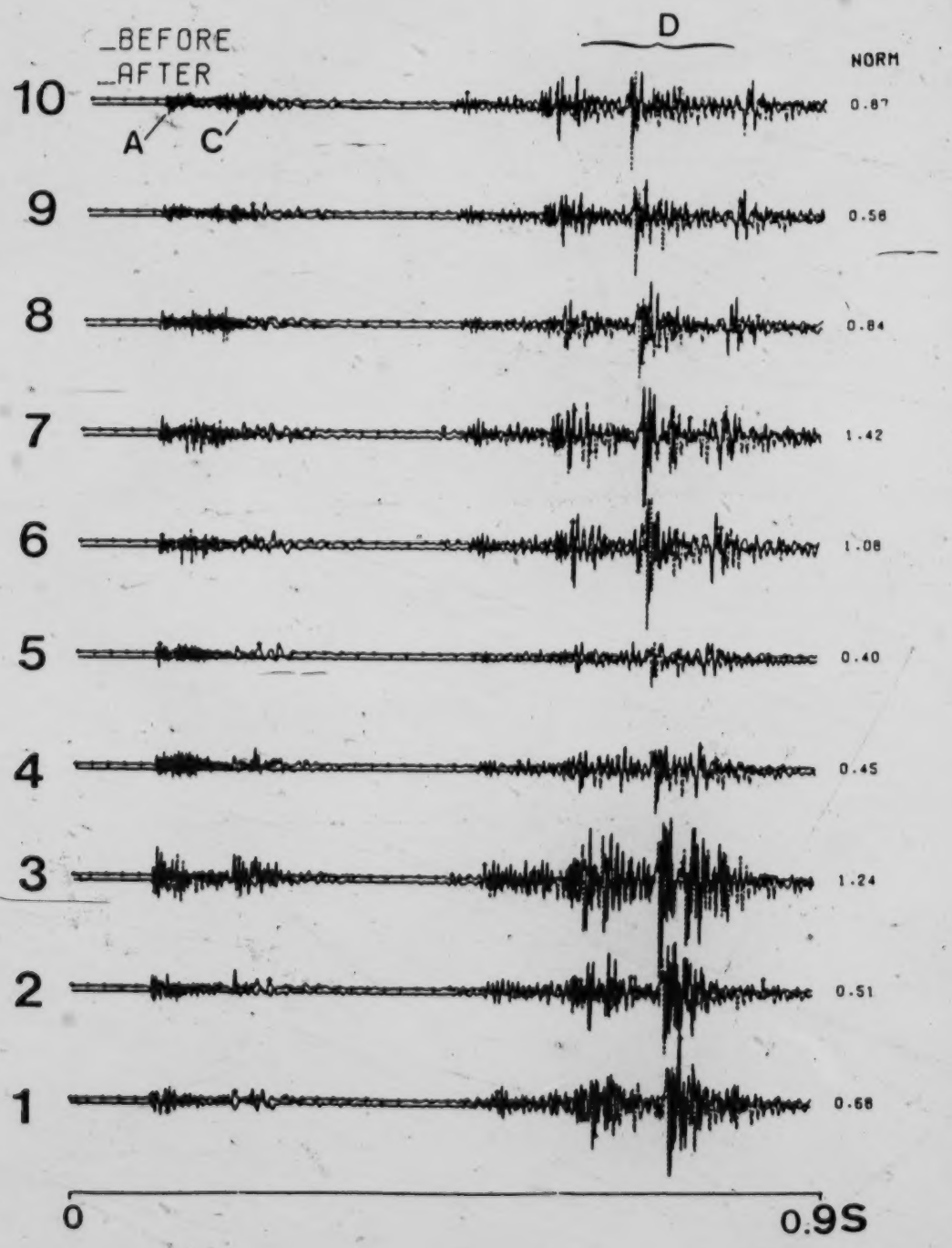

Figure 6.... The first 900 ms of the before and after steam injection seismic records. D: Tube wave arrivals.

contrast at the top of the Clearwater. On the other hand, supportive evidence from theoretical and experimental studies as described in chapter 1 (Tosaya et al.,1984,Nur et al.,1980) indicates that with the inclusion of the steam phase in the formation, the velocity drops by about 20%, at least. Hence we may possibly assume, to a first approximation, a compressional seismic velocity V_p' of 2.0 km/s within the steam zone. Henceforth the terminology 'steam zone' will be used to denote the zone of the seismic anomaly caused by steam injection and production. It should be noted that the steam zone will not necessarily coincide with a zone in which steam is present as vapour in the pore space. With these two velocities in mind one can easily show that a delay ΔT of 2 ms is associated with a steam-zone 24 m wide according to the formula:

$$\Delta T=\Delta H(1/V_p'-1/V_p),$$

ΔH being the width of the zone.

B. Spectral Analysis of the recorded signals

For studying the spectral content of the signals auto- and cross-spectral analyses were carried out. A time window of 100 ms was used for each phase analysed. The data were tapered with cosine bells and a Daniell (1946) window was applied in the frequency domain for weighting the periodograms. Trailing zeros were added as described in Kanasewich (1981). The power spectra for the "before" and

"after" P-phases are shown in Figure 7 It is clear that the 'after' spectra differ largely from the 'before', both in amplitude and in character. It is of interest to mention that comparison of the before and after spectra of the tube waves did not show these differences. These spectra had basically the same spectral content before and after injection apart from an amplitude factor.

Tube waves are interfacial waves traveling along the cylindrical fluid-solid boundary of the borehole (Hardage,1981). Their amplitude is large within the well but decays exponentially with radial distance away from it, (Cheng and Toksoz, 1982). The large amplitude events arriving late in our records -Figure 6- are explained as follows: first a tube wave is generated by the seismic source within the fluid column of the source well. This, generates at the surface a Rayleigh wave which,in turn, excites a tube wave at the top of the fluid column of the receiver well. This downgoing tube wave along with its upgoing reflection from the bottom of the receiver well is picked by our geophone clamped within the well. It is clear now that these events do not pass through the area affected by steam stimulation.

Because of this, their power should be the same before and after steam injection. This was not observed in the original seismograms due to differences in the gain settings,coupling of the seismometers to the well, and source differences from shot to shot. However, the tube

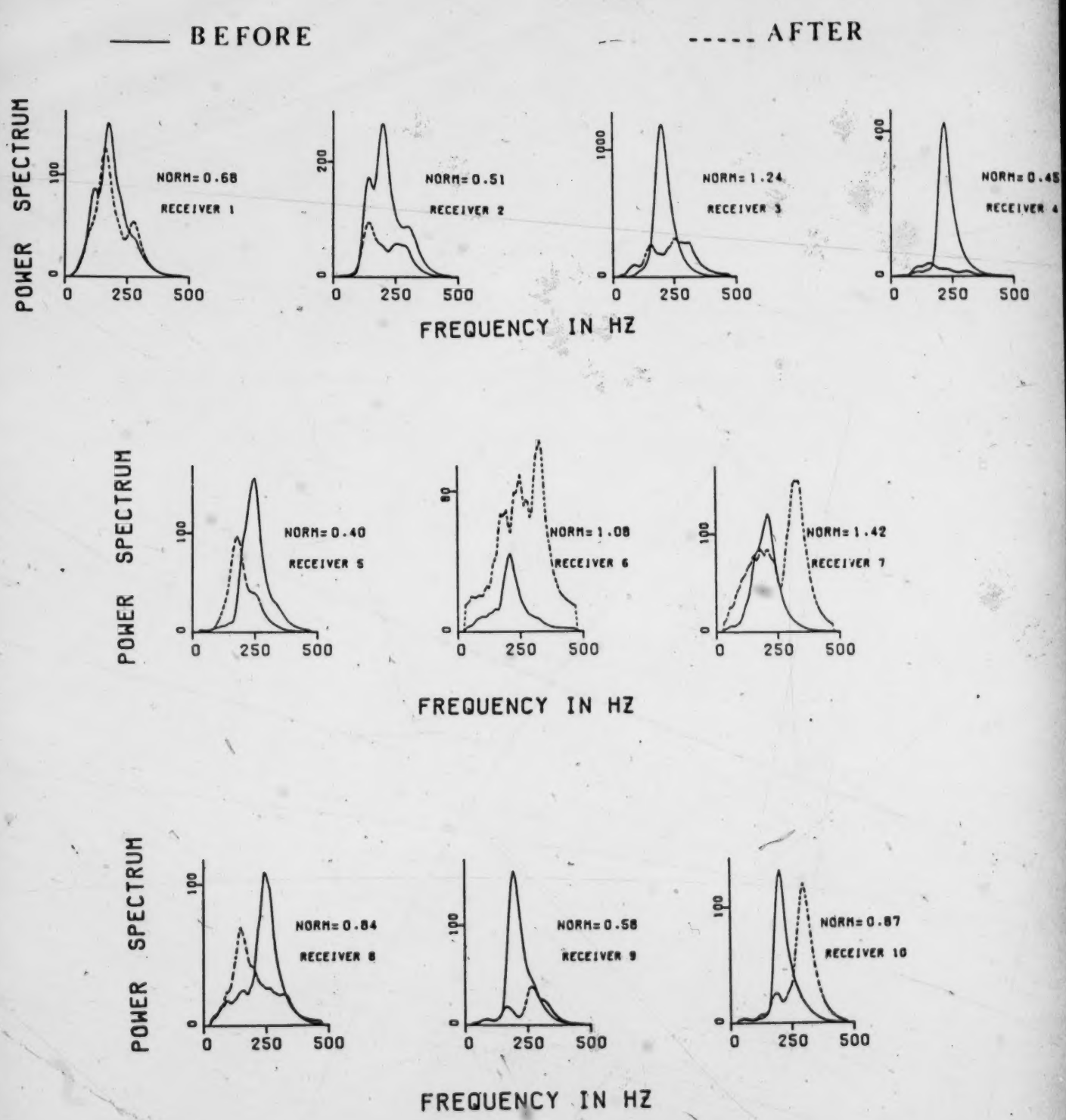

Figure 7.... Power spectra of the P-arrivals,before (solid line) and after (dashed line) steam injection.

waves can be used for calibrating the recorded seismograms . This can be achieved by calculating a normalization factor for each channel to make the power of the "after" tube waves equal to the "before". Then, the same normalization factor can be applied to any other region of the seismogram. The normalization factors are shown at the end of each seismogram in Figures 4 and 6. The spectra of the normalized tube waves are shown in Figure 8 indicating striking similarity in their spectral characteristics before and after steam injection.

The same normalization factors were used for the spectral estimates of the P-waves which were shown in Figure 7. In comparing the P-wave spectra of different channels after normalization, a more consistent picture was obtained. As a general rule the "before" spectra show a single peak concentrated around 220 Hz. In contrast, the "after" spectra are more complex. They are usually bimodal and in some cases shifted to higher or lower frequencies. Most important, the "after" spectra are severely attenuated with respect to their "before" counterparts. An exception to this is observed in the P-wave spectra of records 6 and 7. Their anomalous appearance (high attenuation of the "before" spectra) must be attributed to large local changes in the medium. Notice that the "before" and "after" spectra of the tube waves for these records are in excellent agreement (see Figure 8). It is possible that a localized high water saturation zone, later swept away by the injected steam, is

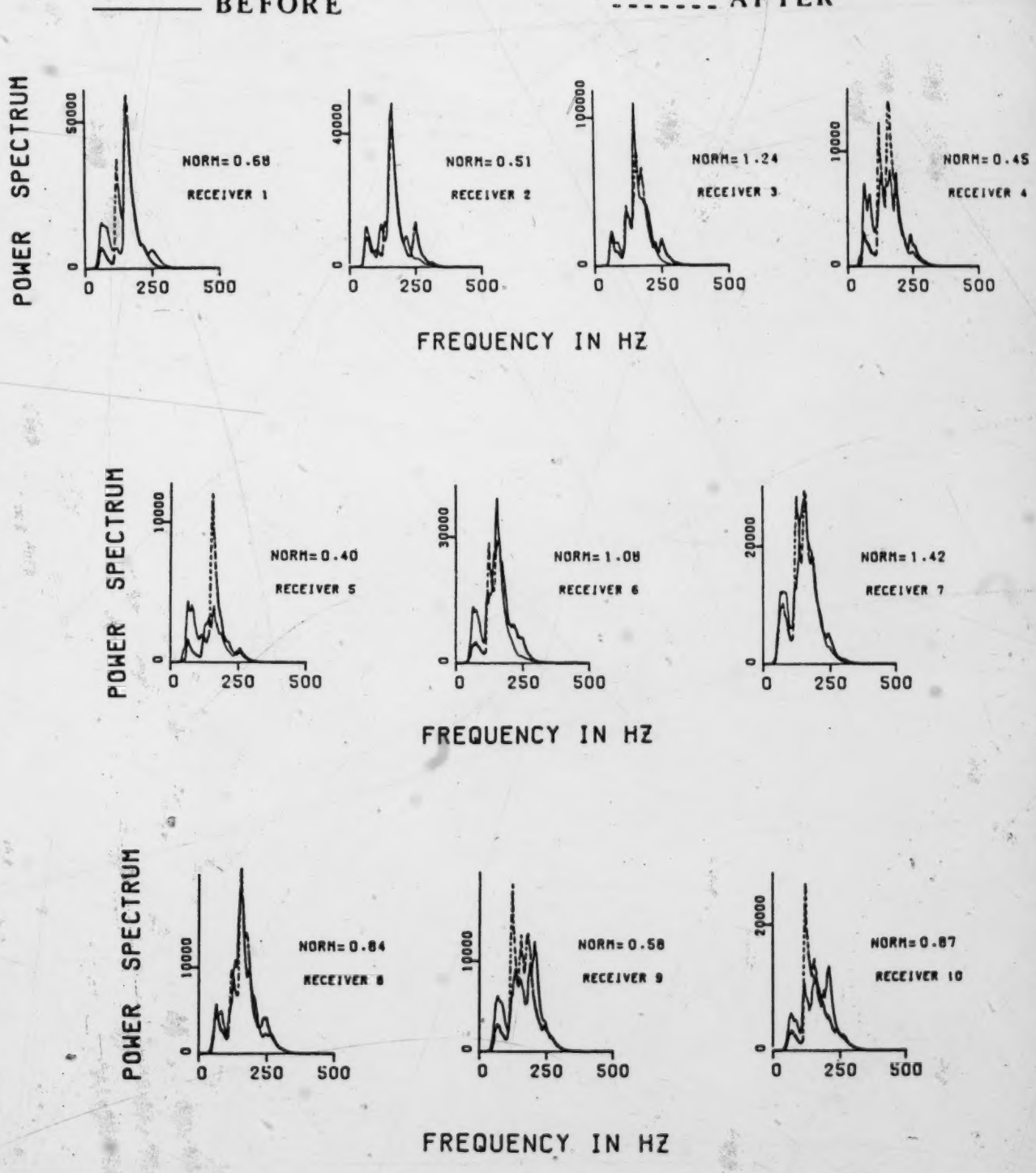

Figure 8.... Power spectra of the tube waves

responsible for these anomalous spectra.

In conclusion,regarding this initial experiment, significant changes in amplitudes, frequency content, and arrival times were found in the "after" seismic signals when comparison was made with their "before" counterparts. The dramatic changes of the "after" seismic spectra reflect the complex modifications the medium has undergone after steam injection. Scattering of the seismic energy from the steam-zone itself is probably an important factor responsible for these spectral changes. These findings along with the high quality of the records encouraged further study.

C. Computer simulation of the proposed experiments

a).Design of the experiments.

It is true that one may proceed to invert the observed delay times and determine the shape of the steam-zone using a simplistic geometric technique and assuming a symmetric distribution of the steam zone around the injection well. However, such a solution will be highly nonunique and of questionable value. For higher resolution and for additional constraints on the reconstructed image a more sophisticated experiment was designed as shown in Figure 9. The two boreholes are vertical so that the experiment is confined to a vertical plane. The distance between the two boreholes is

Figure 9.... Geometry for the proposed seismic tomography experiment . Spacing at sources and receivers is 5 meters. Well-to-well distance is 180 m. Rays penetrating the steam zone are with solid lines. Nonpenetrating rays are plotted with dashed lines

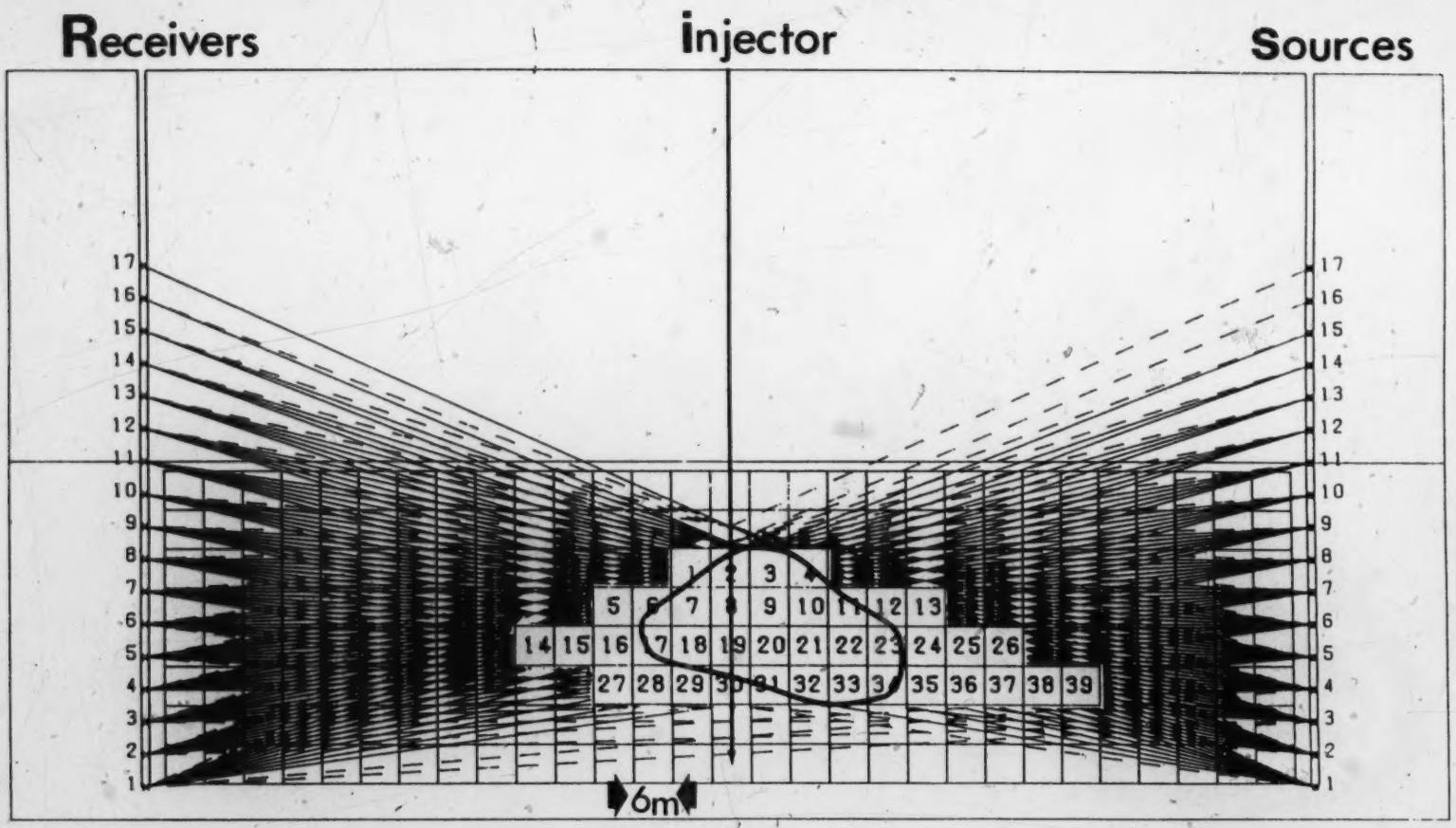
Receivers
Injector
Sources
17
16
15
14
13
12
11
10
9
8
7
6
5
4
3
2
1
1 3
5 6 7 8 9 10 11 12 13
14 15 16 17 18 19 20 21 22 23 24 25 26
27 28 29 30 31 32 33 34 35 36 37 38 39
6m

180 m. Seventeen sources and seventeen receivers are positioned in the boreholes at a spacing of 5 m. The thickness of the target formation (Clearwater) is 50 m. This system of sources and receivers could be extended into the third dimension to provide data for a 3-D seismic tomography study.

Tomography (from the Greek word 'tomo' meaning cut or slice) is a technique of mathematically combining information from numerous raypaths, observed from different angles, into a three-dimensional image of the medium through which the rays have travelled. Chiu et al. (1986) have developed a computerized seismic tomography method based on a damped least-squares inversion scheme for a 3-D. determination of structure and velocity from surface data. Wong et al. (1987) and Bregman (1987) have used cross-hole seismic scanning for tomographic imaging of the space between the boreholes. In medical tomography it is possible, with little or no difficulty and at a very low cost, to position the sources and receivers in such a way as to achieve full angular coverage of the target zone. However this is not usually feasible in geotomography (Dines and Lytle, 1979; McMechan, 1983) mainly because of geological constraints amd also because of cost considerations. The scale of the experiment is also important. In medical tomography the size of the imaged body is in the order of a several centimeters and a resolution better than 1 mm is required. In geotomography, in particular for steam-zone

imaging, the size of the target zone is a few tens of meters and a reconstruction capability to within a few meters would be sufficient. It should be pointed out that in the proposed geometry of Figure 9 the sources and receivers above the Clearwater formation are of particular value as they provide the only ray paths substantially deviating from the horizontal.

As mentioned before, a steam-zone 24 m wide will cause a minimum delay of 2 ms in P-wave arrival times. Hence an event timing accuracy of 1 ms will give an uncertainty of ±12m in the reconstructed images. Therefore we suggest that a sampling rate of at least 0.5 ms must be attained which will give an image resolution of 6m provided of course that the received signals have broad power spectra. Resolution is often thought to be $\lambda/4$ (Widess,1973) where λ is the predominant wavelength computed from the seismic velocity in the medium under investigation. In the presence of noise the determination of travel-time delays will contain some error and as a consequence the quality of the reconstructed picture of the steam-zone will deteriorate accordingly. This value of 6m is also in agreement with the wavelength of the higher frequency components (around 300 Hz) in the observed signals.

b).Least Squares Solution-First approximation

A computer simulation of the experiment was carried out on a the steam-zone assuming the shape shown in Figure 9.

This shape was carefully chosen for our simulation. First it is totally asymmetrical with respect to the injection well. It is this particular asymmetry that we would like to be able to reconstruct, because any preferred direction of growth of the steam-zone is of particular interest to the reservoir engineers. Second, the selected shape has a tendency to be flat which is probably true for steam-zones in flat layered sandstone and shale sequences. And thirdly, its dimensions (maximum width of about 40m) is in general agreement with theoretically predicted values as indicated by the calculations in the Appendix. There are 104 seismic rays penetrating the zone and these are plotted using solid lines in Figure 9. The nonpenetrating rays are shown in dashed lines. Given the shape of the steam-zone and a simple straight ray path assumption it is easy to compute the P-wave travel-time delays by the formula

$$T_i'-T_i = \frac{W_{ST}(V_P-V_P')}{V_P \cdot V_P'} = q_i \qquad i=1,2,\ldots,M=104 \qquad (1)$$

where V_p'=2.0 km/s, V_p=2.4 km/s and W_{st} is the distance the i'th ray has travelled through the steam-zone. After generating this synthetic set of projections, $T_i'-T_i$, our purpose was to invert them, and attempt to reconstruct the correct shape and position of the steam-zone .

As a first step towards this direction, a rectangular grid of pixel size of 6 m by 6 m was superimposed on the Clearwater formation. In this case the travel-time delays

obtained by eq.(1) will be given by a summation of linear terms as:

$$T_i' - T_i = W_{11}F_1 + W_{12}F_2 + \ldots W_{1N}F_N \qquad N=232 \qquad (2)$$

It should be obvious at this point that our intention is to use a series expansion technique for inverting the data. In medical X-ray tomography transform methods of reconstruction, for example the filtered backprojection technique of Shepp and Logan (1974), are very popular and efficient. However the standard formulas require a dense and complete angular coverage of the region of interest if meaningful images are to be obtained. Therefore it appears that these methods are still difficult to use for the irregular and sparse ray path patterns that often appear in seismic applications.

The coefficients W_{ij} in (2) represent the distance the i'th ray has travelled through the j'th pixel and were determined by a computer program we wrote. The quantity F_j to be determined in each pixel j is the differential slowness field:

$$F_j = \frac{1}{V'_{Pj}} - \frac{1}{V_{Pj}} = \frac{V_{Pj} - V'_{Pj}}{V_{Pj} \cdot V'_{Pj}} \qquad , \; j=1,2,\ldots N=232 \qquad (3)$$

where V_{pj} and V_{pj}' are the P-wave velocities within each pixel j before and after steaming, respectively. The summation in (2) must be carried over the total number of pixels in the grid which was 232 in this case. Our purpose was to determine the value of the function F_j for each

pixel. Once this is known, equation (3) can be solved for the unknown velocity, V_{pj}', in this particular pixel. The velocity anomaly can then be associated with the distribution of the steam phase in the reservoir.

If a certain pixel does not lie within the steam-zone then the correct reconstruction should give us $F_j=0$ for this pixel since $V_p'=V_p$ in this case. Negative values for F_j are physically unacceptable since seismic velocities in the steam-zone were lower than than velocities outside the zone, in our model. Also, if F_j were to exceed a certain upper limit (say 0.25) then V_p' would be unacceptably low (less than 1.5 km/s). Ideally, every component of the solution vector $\vec{F}=(F_1,F_2,..F_N)$ must comply with the above physical bounds, so that $0 \leq F_j \leq F_{max}$.

Let us now describe how one can reduce the dimension of this vector $\vec{F}$. If a seismic ray does not penetrate the steam-zone, then for this ray Ti'-Ti=0. This means that no pixel along its path was occupied by the steam-zone, hence all the pixels the ray has encountered must be characterized by $F_j=0$. The pixels occupied by the steam-zone, but not crossed by that ray, will be characterized by $F_j \neq 0$ and $W_{ij}=0$. Hence, by making use of the rays that do not penetrate the steam-zone one can eliminate a large number of unknown pixels and finally define a reconstruction space containing only 39 unknown pixels as shown in Figure 9. Notice how important the ray paths obtained by the sources and receivers situated above the Clearwater formation are, for

the purpose of confining the solution. The conclusion here is that by combining the data of the two experiments ("before" and "after") one achieves a substantial reduction of the dimension of the problem. While previously we had an underdetermined system of equations, now we have a system of 104 equations and only 39 unknowns, hence an overdetermined set of equations because of the additional physical constraints on the problem. The matrix of coefficients W_{ij} is very sparse. This is because each ray penetrates only few of the pixels of the reconstruction domain. In reality, our computations show that only 20% of the elements of the matrix W are nonzero. Obviously, such a matrix is too ill-conditioned for an exact inversion. One could attempt to solve this matrix equation iteratively using Gauss-Seidel or similar methods. However iterative methods for solving matrix equations may be divergent if the matrix is not diagonally dominant. For the seismic imaging problem using cross-hole data, there is no guarantee that the matrix will be diagonally dominant or non-singular. However the system of equations (4)

$$
\begin{aligned}
&W_{11}F_1 + W_{12}F_2 + \ldots W_{1N}F_N = T_1'-T_1 \\
&W_{21}F_1 + W_{22}F_2 + \ldots W_{2N}F_N = T_2'-T_2 \\
&\ldots\ldots\ldots\ldots\ldots\ldots \qquad (N=39) \qquad (4) \\
&\ldots\ldots\ldots\ldots\ldots\ldots \qquad (M=104) \\
&W_{M1}F_1 + W_{M2}F_2 + \ldots W_{MN}F_N = T_M'-T_M
\end{aligned}
$$

can be solved in a least squares sense using standard IMSL subroutines serving this purpose (Lawson and Hanson, 1974). After obtaining the components F_j we solved for the unknown velocities, V_{pj}', and assigned a certain grey level for each range of values of the reconstructed velocities. The Euclidean distance E between the observed (synthetic) projections and the computed projections of the estimated image was calculated by

$$E = \sum_{i=1}^{M=104} (p_i - q_i)^2 \qquad (5)$$

where q_i are the observed projections (delay times Ti'-Ti) and p_i are the computed ones. These (p_i) were calculated by substituting the obtained components F_j back into the original set of equations (4). The solution obtained is shown in Figure 10 as a grey scale reconstructed image of the steam-zone. The diagram also shows the initially assumed shape of the sream zone and the position of the injection well.

The reconstructed image reproduces some of the features of the original shape. However, it contains an artifact at the right end side and some empty spaces within the zone. These may be filled in by solving the problem for a few slightly different positions of the grid and combining the solutions obtained. The assumed seismic velocity within the zone (2.0 km/s) is not accurately reproduced in the reconstructed image. Only very few pixels show the correct velocity. Nevertheless, the deviations are

Figure 10.... Least squares reconstruction of the steam-zone. Assumed P-wave velocity of the steam-zone in the forward calculation was 2.0 km/s.

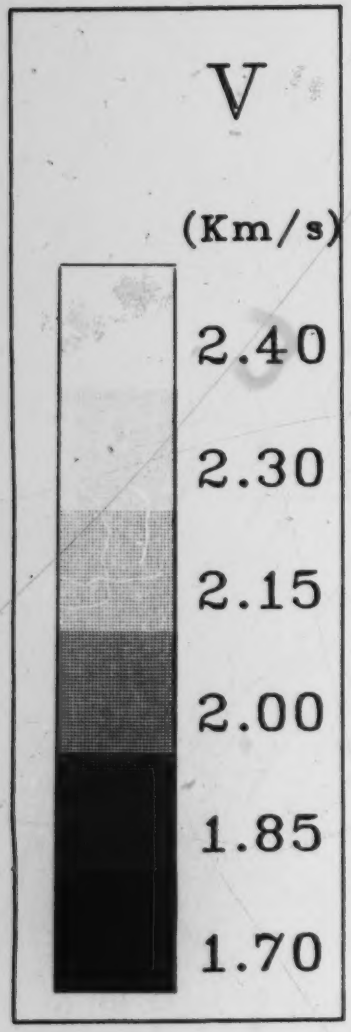

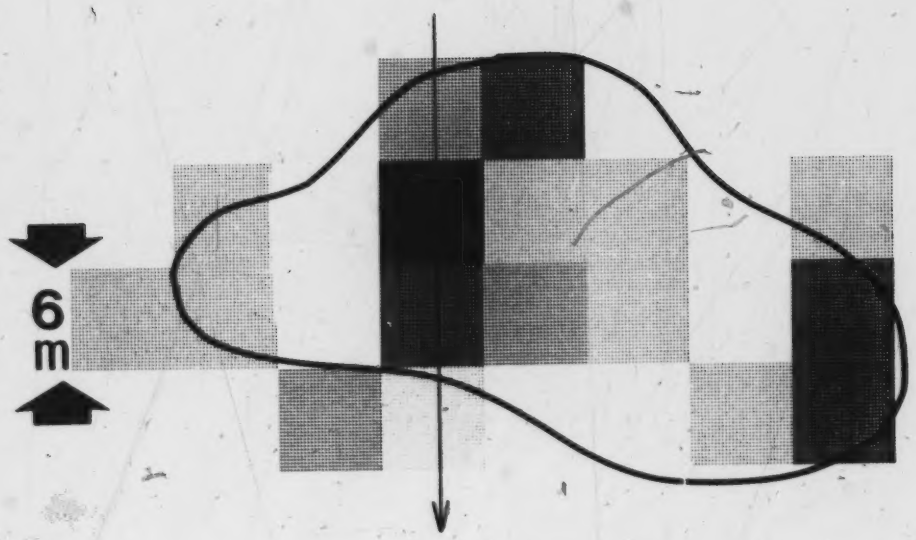

$E = 4.96\ ms^2$

small and even the lowest velocity in the image (1.7 km/s) is still a physically acceptable value. It should be noted that constraining the components of the solution vector within the context of the previously discussed bounds, is beyond the cababilities of the least squares approach. With actual data (measured delay times) it is quite possible that due to the presence of noise and to the finite sampling interval, negative values F_j may appear in our solution. This actually occured when we repeated the above least squares reconstruction after introducing a random noise of ±0.5 ms in the synthetic data. If a pixel has a negative F_j this will affect the solution in many other pixels and the reliability of the final solution will remain questionnable.

c).Applying the Method of Projections

As a means of improving the quality of the reconstructions an algebraic reconstruction technique (ART) was employed. A modern account of ART and its variation known as SIRT (simultaneous iterative reconstruction technique) is given by Ivansson (1986). Usually ART converges more rapidly than SIRT. The image represented by $\vec{F}=(F_1,F_2,\ldots F_N)$ may be considered to be a single point in an N-dimensional space. In this space each of the equations (4) represents a hyperplane. When a unique solution to these equations exists, the intersection of all these hyperplanes is a single point giving the solution. Hence the Káczmarz method of projections (Kaczmarz,1937,Rosenfeld and Kak,1982)

can be applied for solving the system of equations. An arbitrary initial guess at the solution $\vec{F}$ can be made and let us call this $\vec{f}^{(0)}=(f_1^{(0)},f_2^{(0)},\ldots f_N^{(0)})$. This initial guess is projected on the hyperplane represented by the first of the equations in (4) giving the first projection $\vec{f}^{(1)}$

$$\vec{f}^{(1)} = \vec{f}^{(0)} - \frac{(\vec{W}_1 \cdot \vec{f}^{(0)} - q_1)\vec{W}_1}{\vec{W}_1 \cdot \vec{W}_1} \qquad (6)$$

where $\vec{W}_1=(W_{11},W_{12},\ldots W_{1N})$. After $\vec{f}^{(1)}$ is obtained we take its projection on the hyperplane represented by the second equation in (4) which gives the second projection $\vec{f}^{(2)}$. This process is repeated with the third hyperplane and so on. The projection on the j'th hyperplane may be obtained from that on the (j-1)'th hyperplane by

$$\vec{f}^{(j)} = \vec{f}^{(j-1)} - \frac{(\vec{f}^{(j-1)} \cdot \vec{W}_j - q_j)\vec{W}_j}{\vec{W}_j \cdot \vec{W}_j} \qquad (7)$$

where $\vec{W}_j=(W_{j1},W_{j2},\ldots W_{jN})$. The process of taking projections on different hyperplanes is continued until one obtains $\vec{f}^{(M)}$ by taking the projection on the last equation in (4). One then iterates by projecting $\vec{f}^{(M)}$ on the first hyperplane again. This process continues until all the M hyperplanes have again been cycled through, resulting in $\vec{f}^{(2M)}$. The

second iteration is started by projecting $\vec{f}^{(2M)}$ onto the first hyperplane again, and so on. It has been shown by Tanabe (1971) that if a unique solution $\vec{f}_s$ to the system of equations exists, then

$$\lim_{K \to \infty} \vec{f}^{(KM)} = \vec{f}_s \qquad (8)$$

If the system of equations (4) is overdetermined and the data $q_1, q_2, \ldots q_M$ are corrupted by noise no unique solution exists. Then, instead of converging to a single point, the solution will oscillate in the neighborhood of the region of the intersection of the hyperplanes. If the error in the data is too large the equations may be inconsistent in which case the algorithm will diverge. If the system is underdetermined, an infinite number of solutions is possible . Furthermore, Tanabe has shown that, in this case, the solution obtained by the iterative procedure described above strongly depends on the choice of the initial guess.

In typical radiology applications the size of the matrix W can be enormous (10^{11} - 10^{17}) as thousands of projections are usually available. In such cases serious difficulties with exact implementation of (7) can be encountered with respect to storage and fast retrieval of the weight coefficients W_{ij}. To get around these difficulties a myriad of approximations to (7) have been suggested in the literature (Herman, 1980, Rosenfeld and Kak,1982). A further approximation, known to result in a substantial increase in computer speed, is to consider W_{ij}

as being a simple function of the perpendicular distance between the center of the j'th pixel and the i'th ray. If the ray intersects the pixel then W_{ij} is set equal to 1, otherwise it is set equal to zero. In the geotomography applications suggested in this thesis, the size of the matrix is expected to be modest (around 10^4). Hence we proceeded with an exact implementation of (6) and accurate calculation of the coefficients W_{ij}.

A very attractive feature of this method of projections which makes it particularly suitable for our problem is that it is very easy to impose upon the solution the previously discussed constraints (Gordon,1974,Rangayyan,1984). If a component F_j of a projection is negative, it is set equal to zero and if $F_j > F_{max}$ then F_j is set equal to F_{max}. We set $F_{max}=0.095$ which prevented any values of V_p' to be lower than 1.92 km/s. Even without imposing the above restrictions only slight violations of the limits F_{min} and F_{max} were observed. This shows that by implementing the above bounds one perturbes slightly,when necessary, the positions of the projections on the hyperplanes. Another advantage of the method is that it is not affected by the sparseness of the matrix W. The above method of projections was applied to our problem of inverting the computed delay times by choosing a zero initial guess ($F_j=0$) for all the pixels in the reconstruction space and by programming in the computer the recursive formulas (6) and (7). The solution was constrained according to $F_{min} \leq F_j \leq F_{max}$. A value of F_{min} slightly above zero

gives optimum results. The solution obtained (Figure 11 shows a substantial improvement over the least squares reconstruction. There are no artifacts or empty spaces within the image and agreement with the correct shape of the steam-zone is better . Futhermore the mosaic of seismic velocities observed in the least squares solution has now been replaced by a uniform reconstruction showing only minor deviations from the correct velocity of 2 km/s. As mentioned earlier, the initial guess on the solution was zero ($F_j=0, j=1,2,...N$, i.e. $V_{pj}'=V_{pj}$) We also experimented with nonzero initial guesses. One of them was the solution previously obtained by the least squares reconstruction. All these attempts provided inferior solutions indicating that biasing of the initial guess should probably be avoided. For further testing of the algorithm, random noise of ±0.5 ms was introduced into the projection data and the reconstruction procedure was repeated. The solution obtained is shown in Figure 12 The quality of the solution is quite similar to the quality of the previous reconstruction which was obtained on the basis of ideal data. This result was a further indication that a sampling frequency of 2,000 Hz during the seismic recording would probably be sufficient for the performance of our reconstruction algorithm.

As mentioned before, the resolution of the images shown so far was 6 m. Let us now use a finer grid composed of pixels 4 meters by 4 meters, as shown in Figure 13. This does not affect the number M (=104) of the seismic rays

Figure 11.... Steam zone reconstruction obtained by the method of projections.

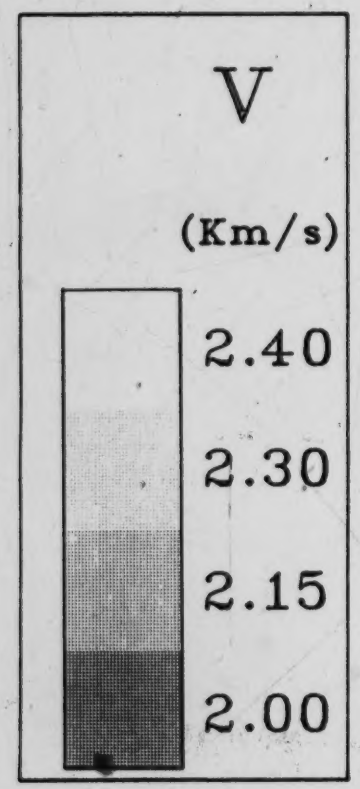

$E = 4.90\,ms^2$

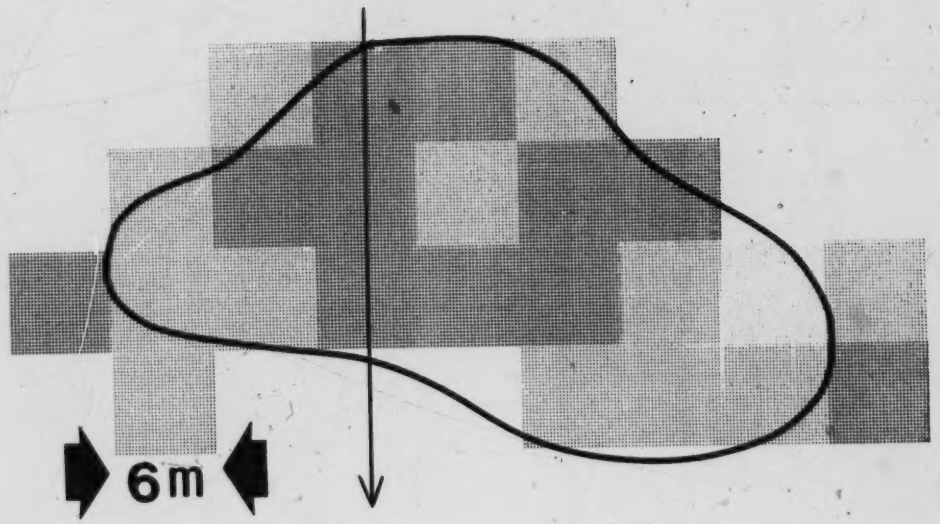

Figure 12.... Reconstruction as in Figure 11 after introducing random noise of ±0.5 ms into the projection data.

$E = 5.92 ms^2$

Figure 13.... Geometry of the proposed experiment as in Figure 9 but with pixel size of 4 meters

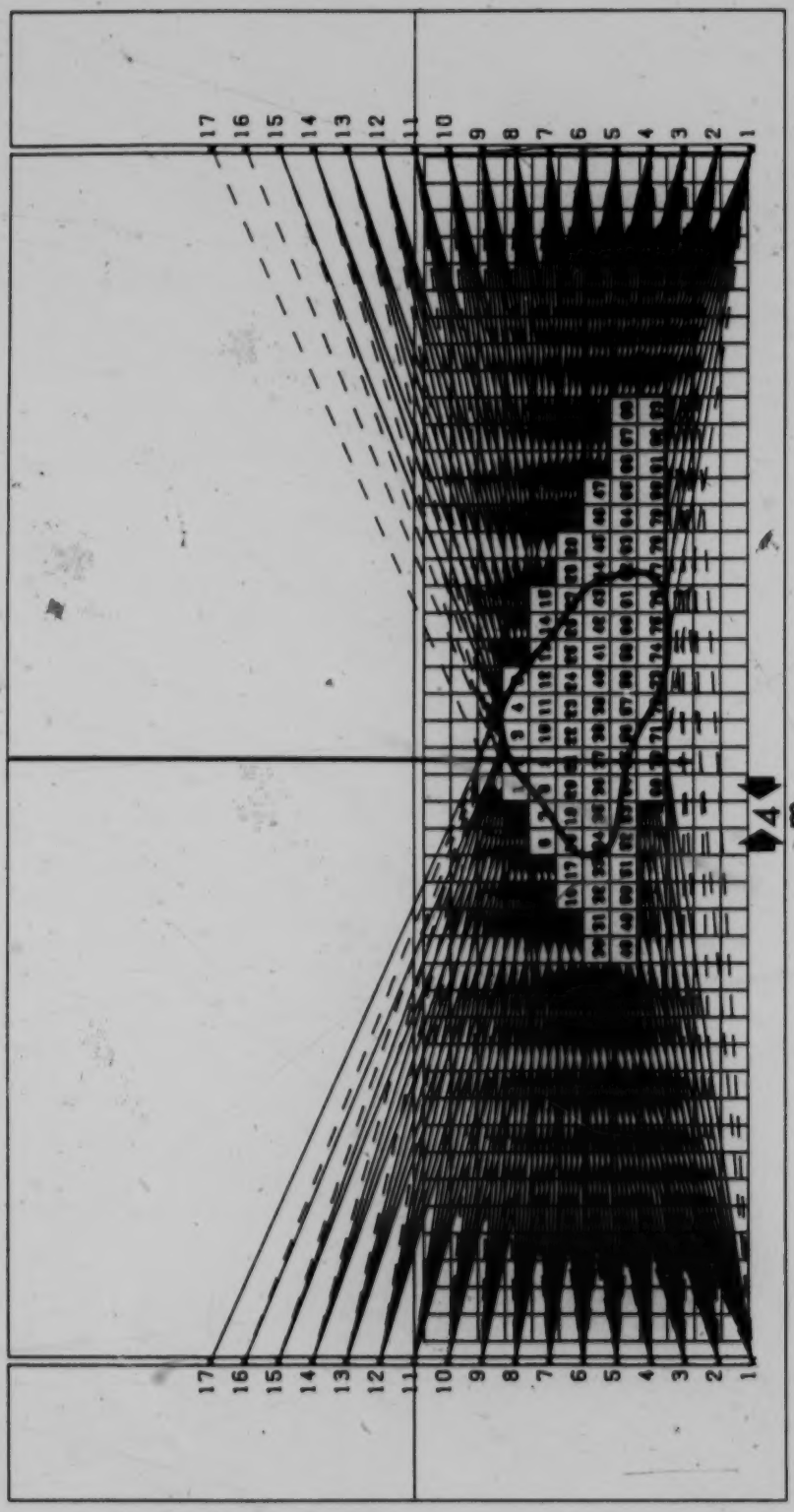
17
16
15
14
13
12
11
10
9
8
7
6
5
4
3
2
1
4 m

penetrating the target but it affects the dimension N of the reconstruction space which now contains as many as 83 unknown pixels. The system of equations (4) is still overdetermined and was solved using the fully constrained method of projections as described in the previous paragraphs. It should be pointed out that the least squares solution for this finer grid failed: The Euclidean distance was small (2.20) but unacceptable because of the presence of several large negative values within the solution. The ART reconstruction is shown in Figure 14. Although the demands upon the data are greater (greater number of unknowns) the result is a superior reconstruction. The details of the shape as well as the correct seismic velocity within the zone have been reproduced more efficiently. The value of the Euclidean distance also improves to 2.53, about half of the values previously obtained. This value translates (by dividing by the number M of equations and taking the square root) into an average discrepancy between observed and computed projections of 0.15 ms.

The method is computationally fast and efficient as shown in Figure 15 which indicates that convergence is achieved after 10 to 15 iterations, whereupon the Euclidean distance is minimized and remains practically constant thereafter. As mentioned before, the components F_j of the solution were fully constrained to lie within the limits F_{min} and F_{max} (=0.094). F_{min} must be nonnegative and initially was

Figure 14.... Reconstruction obtained by the method of projections with pixel size of 4 m.

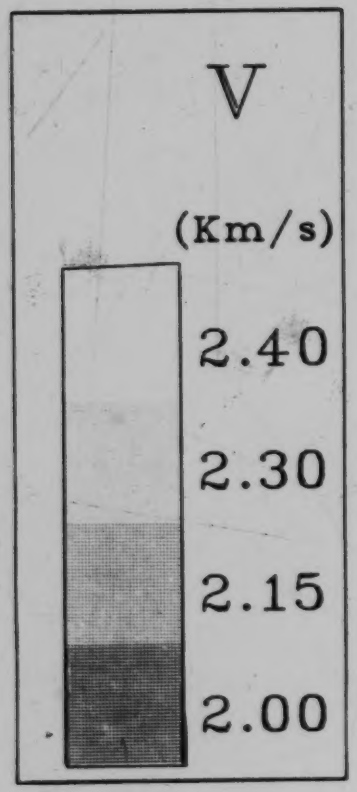

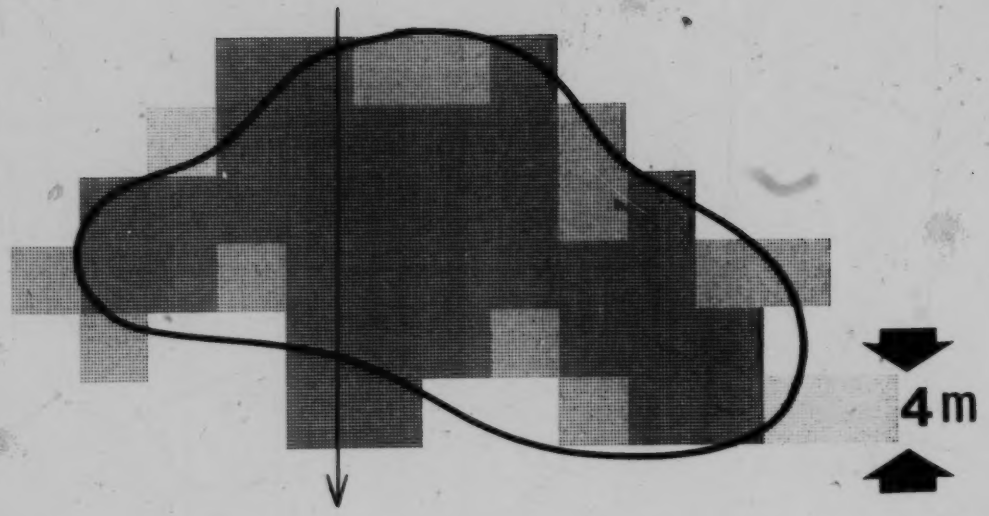

$E = 2.53\ ms^2$

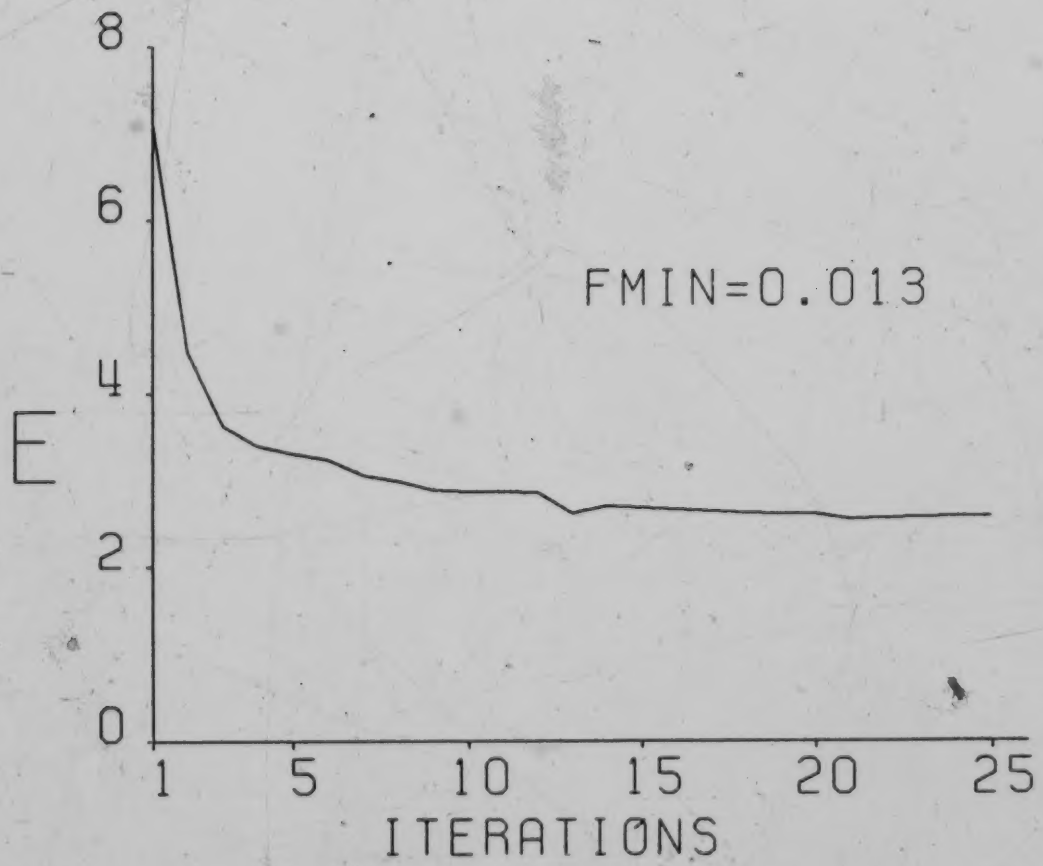

Figure 15.... Convergence diagram showing reconstruction error E (Euclidean distance) versus number of iterations

taken to be zero. However it was found that for F_{min}=0.014 (V_p'=2.31 km/s) one obtains a more accurate reconstruction as shown in Figure 16. Figure 16 also shows that if one attempts to overconstrain the solution by making the limits of the inequality $F_{min} \leq F_j \leq F_{max}$ too narrow, then the solution is of questionnable quality as shown by the large values of the Euclidean distance.

The resolution and the quality of the reconstructed images are related to the spacing of the sources and receivers. As seen in the simulation, superior results were obtained when a finer grid was used. However, the ability to apply finer and finer grids depends on the density of the coverage of the target area and the availability of short wavelengths in the elastic wave source. If in the above simulation with station spacing of 5 m, one had applied a grid with pixel size smaller than 4m by 4m one would arrive at a reconstruction space containing greater number of unknown pixels than the number (104) of available equations. A denser system of sources and receivers would have allowed us to apply a finer grid and still keep the system of equations overdetermined. In fact, the above arguments led us to the decision to use a station spacing of 3 m in the new field experiment.

As mentioned, an image resolution of 4 m was attained in the reconstructions while the wavelength of the higher frequency components of the recorded signals in the field experiment is not expected to be shorter than 6 m. However,

Figure 16.... Trade-off diagram showing dependence of the reconstruction error upon the constraints imposed on the solution

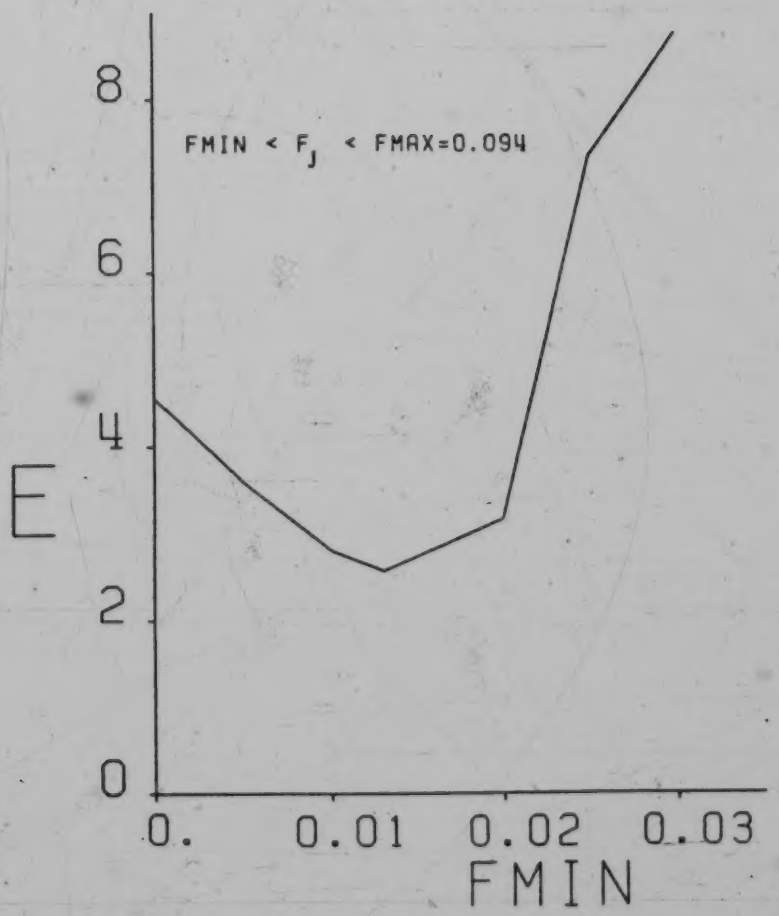
8
6
4
2
0
E
FMIN < F_J < FMAX=0.094
0.
0.01
0.02
0.03
FMIN

the resolving power obtainable with a broad-band source is not identical to that given by the arbitrary Rayleigh criterion using a monochromatic source. Small anomalous phase differences in the recorded analog signal on individual receivers can be used to detect the presence of pixels with anomalous velocities. For instance, the use of phase shifts is critical in resolving small (1 or 2 ms) vertical closures of anticlines in reflection seismology even though the signal wavelet has dominant periods of 40 or 50 ms. In another technique, in astronomy, one can detect the presence of binary stars or the size of disks from a Michelson mirror interference pattern (Sommerfeld, 1964).

d.Ray Bending

So far we have assumed straight path propagation for the seismic rays. In fact most tomography reconstruction algorithms are based on this assumption. In medical X-ray and emission tomography where the measured quantity is the attenuation along the ray path this is not a limitation. However in ultrasound tomography where the measured quantity is time of flight this assumption is approximately satisfied only for soft-tissue structures. For parts of the body containing bone, severe beam refraction at tissue-bone interfaces occurs and the method fails. Refraction occurs even between different soft-tissue structures. However, time of flight ultrasound tomography based on the straight ray path assumption is known to provide satisfactory

reconstructions in these cases (Greenleaf and Johnson, 1978). Let us now relax the straight ray path assumption in our case of seismic imaging of the steam-zone and let us consider more realistic ray paths obeying Snell's law. A computer simulation ray diagram of this situation is shown in Figure 17. The steam zone has been approximated by a large number of horizontal segments interconnected by vertical ones. This design is justified by the fact that highly pressurized steam is injected into a horizontally stratified medium. The diagram reveals a number of interesting possibilities. Ray bending is weak but it can also be severe causing some energy scattering away from the receivers. It is also possible to have arrivals at the same receiver from two different paths: a weakly refracted and a more severely refracted one which according to our calculations arrives about half a millisecond later for the P-phase. The next step was to generate, using the computer, a synthetic set of data (delay times caused by the steam-zone) according to the ray bending model. These synthetic data can be interpreted as being due to straight paths and were given as input to our reconstruction algorithm. The purpose was to see whether or not ray bending introduces any substantial distortion into the solution and if so, to explore iterative ray tracing techniques imposing step-by step corrections to the reconstructed image. The reconstruction based on ray bending synthetic data is shown in Figure 18. After comparing Figures 14 and 18, we can see

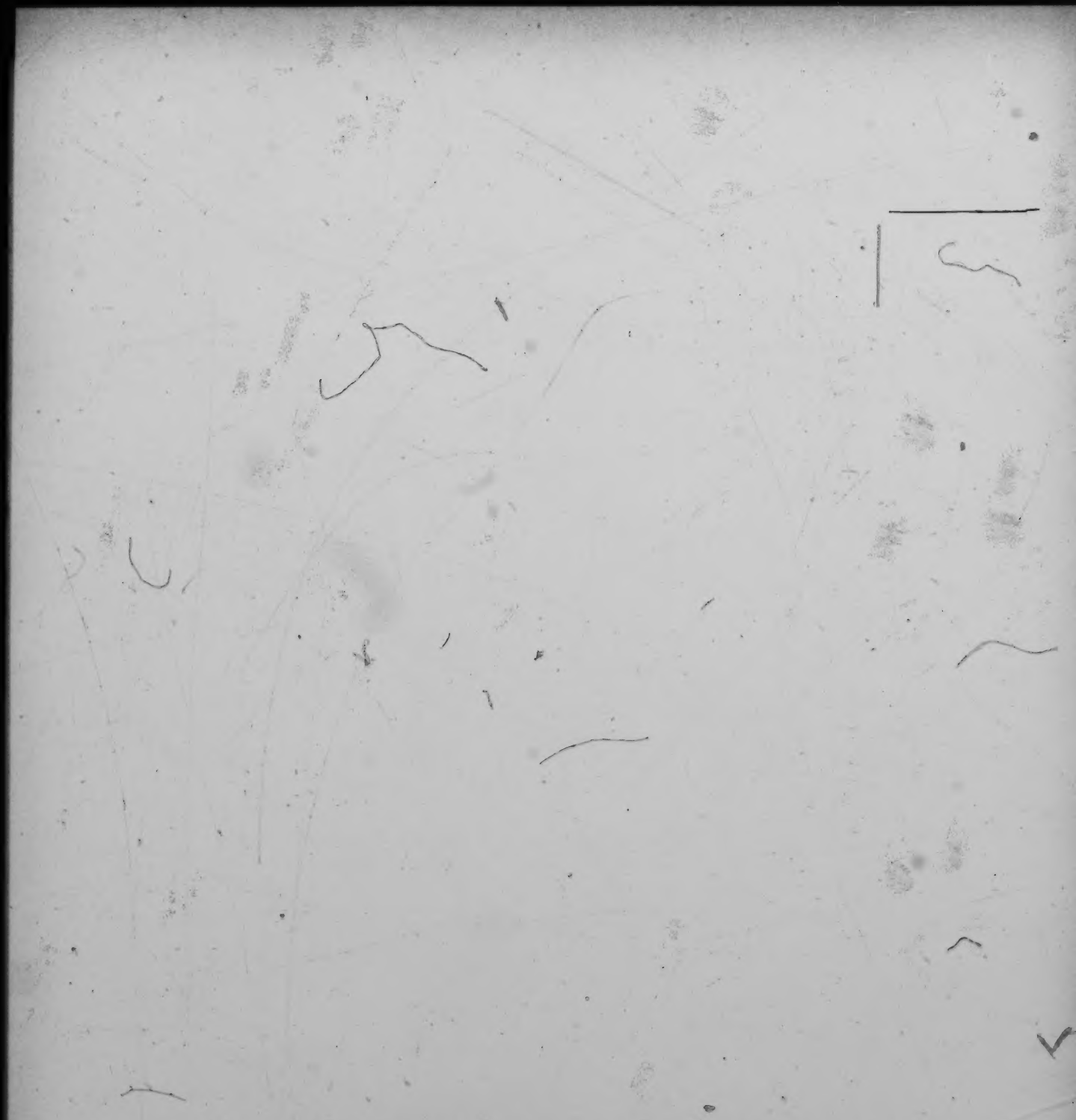

Figure 17.... Ray diagram showing refraction of the seismic rays within the steam-zone according to Snells law.

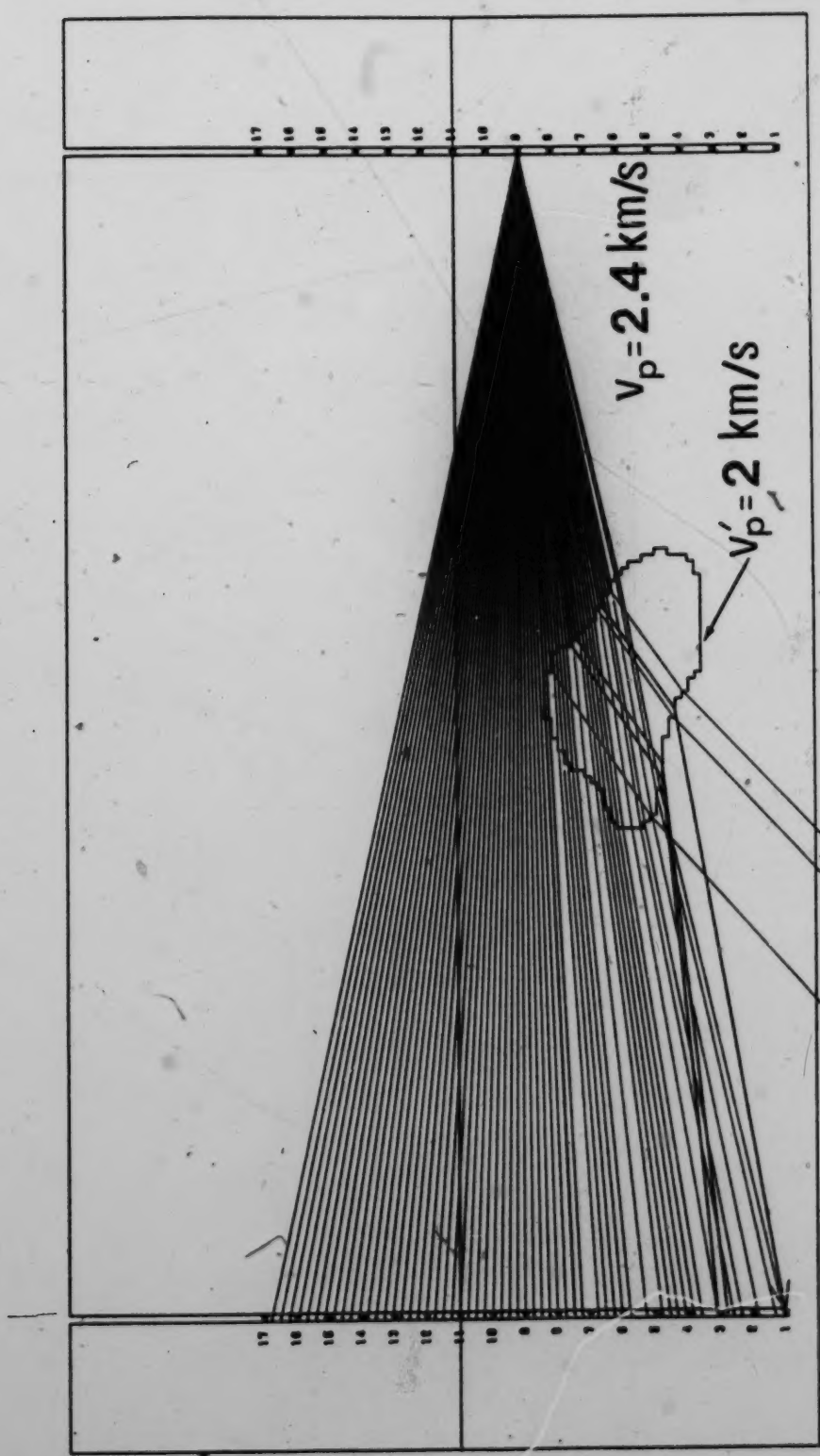
V_p=2.4 km/s
V'_p=2 km/s

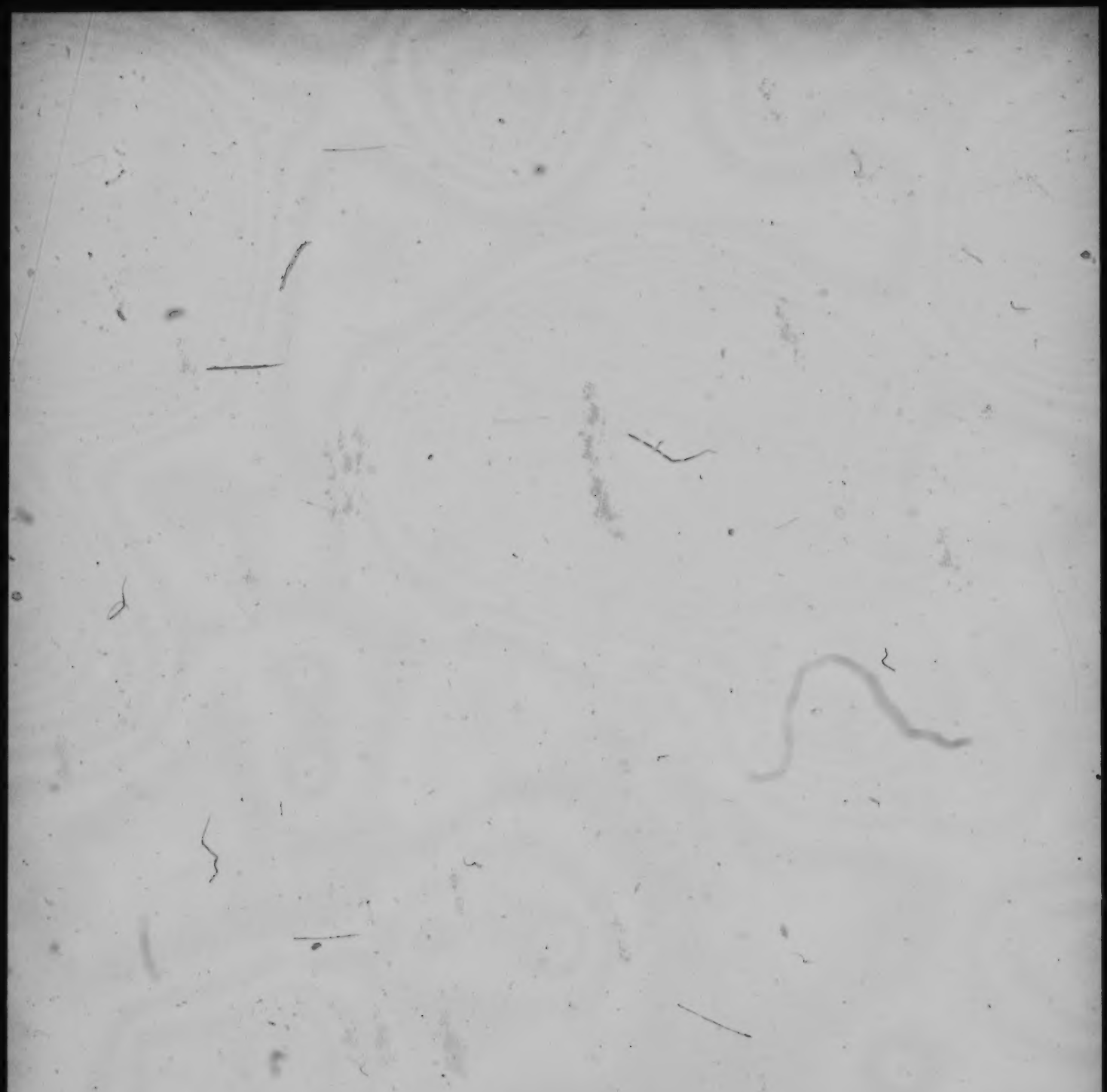

Figure 18.... Reconstruction based on ray bending synthetic data

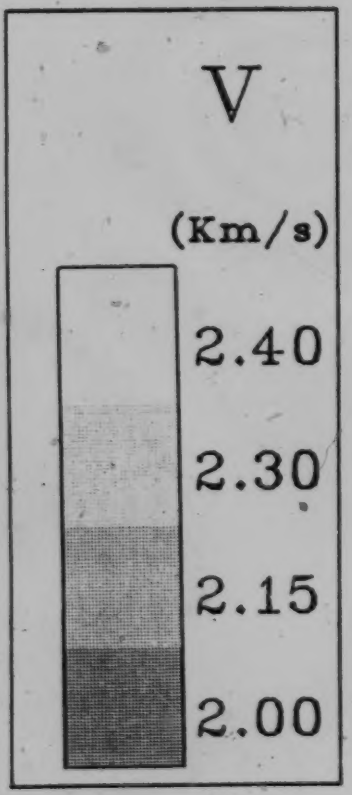

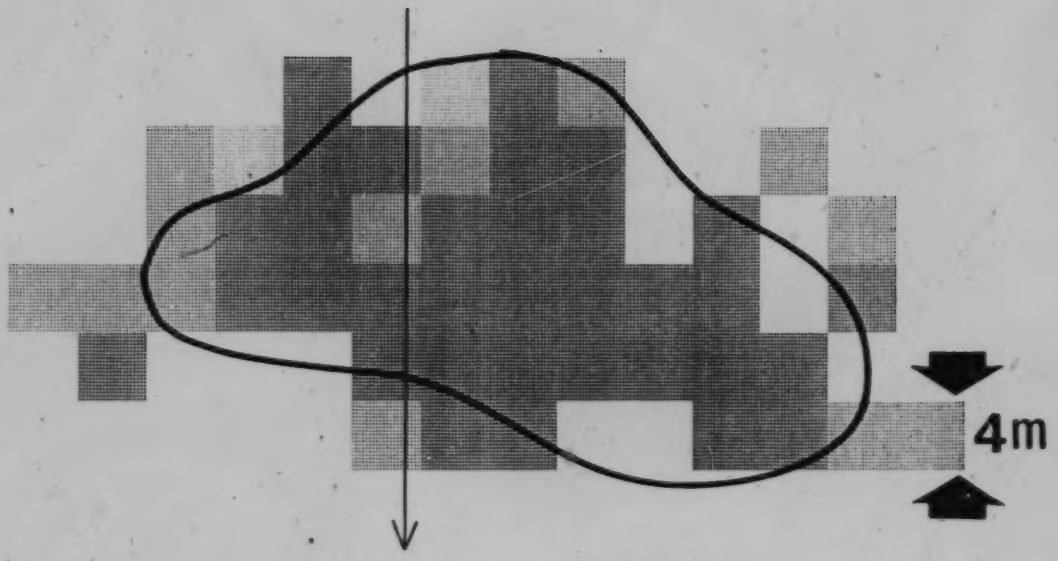

$E = 2.89\ ms^2$

that only minor distortion-mainly in the shape of the anomalous zone-is introduced in the reconstructed image. This, along with the fact that the Euclidean distance E=2.89 is only slightly higher than the previous value of 2.53, indicates that ray bending, for the assumed velocity contrast of 20%, probably plays a second order effect in the quality of the reconstruction. A similar conclusion has been reported by Dines and Lytle (1979). If the velocity differences become larger, ray bending should be taken into account.

A final comment about the quality of the reconstructions is in order. One might wonder why even the best solution (Figure 11) is not in perfect agreement with the ideal reconstruction. The answer to this question lies in the fact that angular coverage of the target zone is quite limited, (maximum 25°) in our proposed tomography experiment, and relatively few rays substantially deviate from the horizontal. In particular, notice that reconstruction imperfections occur at the bottom of the steam-zone where density of coverage is lower. To state it in other words, if the experiment had yielded only horizontal ray paths it would have been impossible to reconstruct the steam-zone within any reasonable degree of accuracy and uniqueness. It would be desirable to bring into the analysis the reflections from the Paleozoic which is situated 60 meters below the Clearwater. However, as our ray tracing calculations indicate, these reflections do not pass

through the steam invaded zone.

We could, of course, for the purposes of the simulation,include sources and receivers below the Clearwater Formation and thus increase the angle of coverage substantially. However, wells are not generally drilled below the Clearwater in order to avoid the possibility of the steam entering the water zone below the Clearwater Formation.

e)Further computer experimentation For further testing the reconstruction algorithm we carried out computer simulation on the basis of a slightly modified geometry. This was similar to the geometry in Figure 13 except that the spacing of sources and receivers was set more optimally at 3 meters resulting to a more dense ray coverage of the space between the two wells. Angular coverage of the Clearwater was slightly increased. Furthermore,the phantom consisted, in this case, of three seismically distinct zones: two zones elliptically shaped, caused by the steam injection, imbedded into an otherwise homogeneous medium characterized by a uniform P-wave velocity of 2.4 km/s. The inside ellipse represents the steam zone in which the P-wave velocity has dropped to a value of 1.8 km/s. The zone between the inside and outside ellipse corresponds to a zone dominated by steam condensation and high saturation of heated oil. P-wave velocity in this zone was 2.1 km/s in the model. This picture of two distinct zones created around a steam

injector, in response to steam stimulating a tar sand formation, is in general agreement with theoretically and experimentally predicted models of formation heating by steam injection, as was outlined in Chapter 1. It was indicated in those paragraphs that both temperature and pressure are expected to be constant within the steam zone. Since these are the two important parameters that control seismic velocity, it seems justifiable to consider a constant velocity within the steam invaded zone. In the heated zone around the steam zone, temperature and pressure gradually decrease until undisturbed reservoir conditions are encountered. This could lead to seismic velocity gradients in the zone. For the purposes of simplicity however we have assumed in our model an average constant velocity within this zone.

Our purpose was to investigate the capability of our algorithm to discriminate between closely spaced diverse seismic zones within the reconstruction space. Again the first step was to solve the forward problem of computing delay times. This, assuming a straight ray path model, was accomplished by using the following simple equation:

$$T_i' - T_i = W_i(V_1 - V_2)/V_1V_2 + W_i'(V_1 - V_3)/V_1V_3 \qquad (9)$$

where V_1=2.4 km/s, V_2=2.1 km/s and V_3=1.8 km/s. W_i is the

distance the i'th ray has travelled within the condensation zone and W_i' is the distance travelled within the steam zone. The first term in (9) is the contribution to the delay time from the condensation zone. The second term is the contribution from the steam zone. Upon computing these synthetic delay times our purpose was to invert them and reconstruct the seismic velocity distribution between the boreholes. Again, full use was made of the nonpenetrating rays to effectively confine the reconstruction domain shown with bright yellow color in Figure 19. The pixel size of the superimposed grid was 4 by 4 meters resulting to a system of 299 equations and 171 unknown pixels. The result of the reconstruction (20 iterations) is shown in Figure 20b). The initial guess on the solution was zero differential slowness in all the pixels. The values F_j were constrained according to $0.013 \leq F_j \leq 0.16$ i.e. 1.7 km/s$\leq V_{pj}' \leq$2.32 km/s. There is some indication in the center of the image of the existence of a low velocity zone. However the quality of the reconstruction is not satisfactory.

At this point one has to be fully aware of the difficulties inherent with the task of inverting the data. We are dealing with a limited angle tomography problem, the main limitation being that only a narrow angular coverage of the field (maximum 35°) was achieved by the scanning geometry in the experiment. Stratigraphic complications as well as serious cost considerations precluded a broader angular coverage of the area under investigation. To reduce the degree of nonuniqueness of the solution both horizontal

Figure 19. Ray diagram of the computer simulation also showing the phantom (two ellipses). Pixel size in the grid is 4 m. Rays penetrating the elliptical zones are plotted with yellow color. Nonpenetrating rays are plotted with blue color. Reconstruction space is the bright yellow region. Redundancy is indicated by the green colored area which surrounds the reconstruction domain and results from overlapping of the nonpenetrating and penetrating rays.

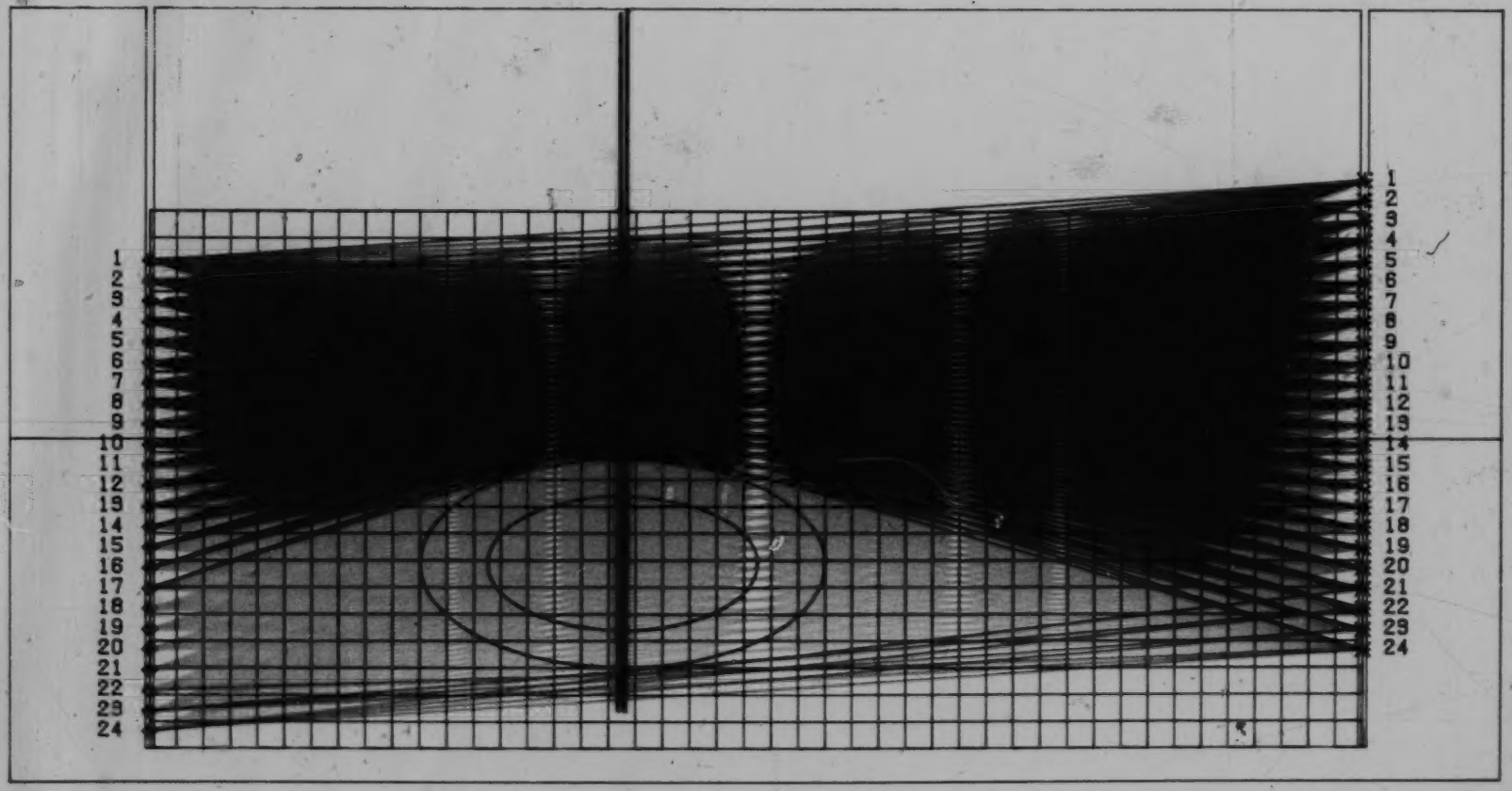
RECEIVERS
SOURCES
1 2 3 4 5 6 7 8 9 10 11 12 13 14 15 16 17 18 19 20 21 22 23 24
1 2 3 4 5 6 7 8 9 10 11 12 13 14 15 16 17 18 19 20 21 22 23 24

Figure 20.... a).The phantom used for the computer modeling; b) Reconstruction (20 iterations) based on fully constrained ART.

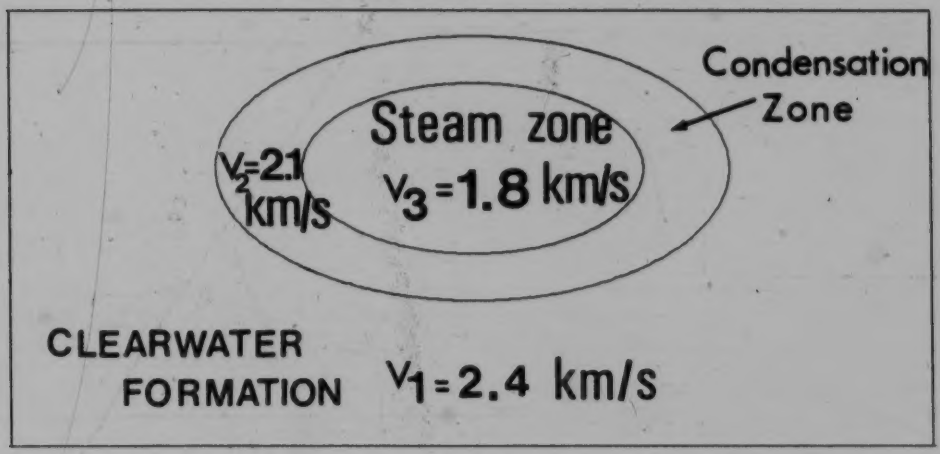
Condensation
Zone
Steam zone
V_3=1.8 km/s
V_2=2.1
km/s
CLEARWATER
FORMATION
V_1=2.4 km/s

a

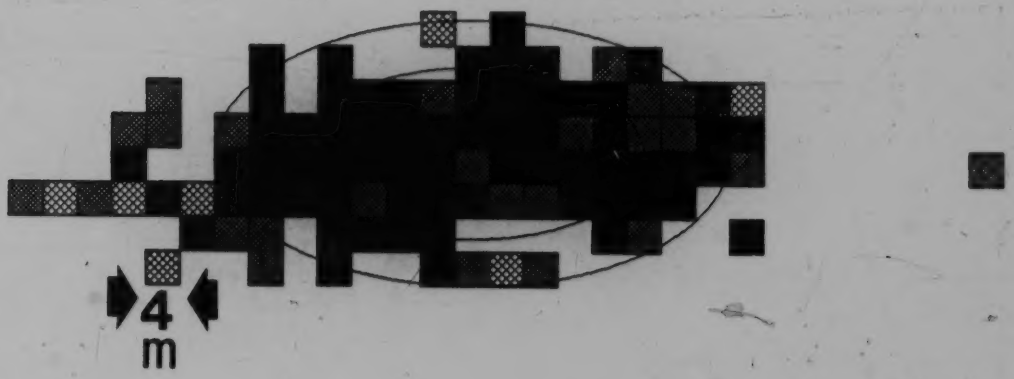
4
m

1.80 1.95 2.10 2.25 2.40 KM/S

b

E = 0.50 MS

Figure 21.... a): Reconstruction after combining ART with smoothing; b): Reconstruction after combining ART with smoothing and data interpolation (10 iterations)

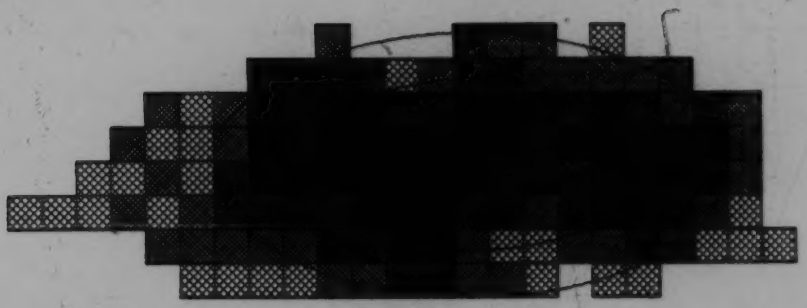

E = 0.44 MS

a

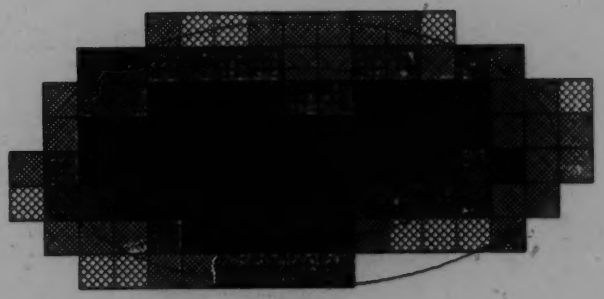

b

E = 0.34 MS

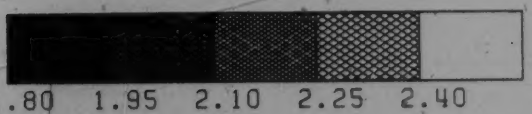

and deviating rays are needed. Another source of error in the solution is introduced by the discretization of the reconstruction space by using pixels of finite size. The Euclidean distance of the solution would not be zero even if each pixel in the reconstruction had precisely the correct velocity value. This is because the exact shape of the anomalous zone can only be approximated when using a pixel by pixel image provided that the size of the pixels remains finite. One of course can make the size of the pixels arbitrarily small but then a too large number of unknown parameters (larger than the number of the available equations) will have to be determined. The effect of space discretization on the error of the solution was well demonstrated by the first computer simulation example. When subdivision of the reconstruction domain was made finer, the error of the solution decreased drastically although a substantially larger number of unknown parameters had to be determined. Other sources of uncertainty are of course the finite spacing of sources and receivers, which gives rise to a finite amount of data, and the presence of noise in the recorded signals. Incompleteness of the data set is introduced by the narrow angular coverage of the target area. Missing data is also a possibility in real recordings. Notice also that the spacing at the sources and receivers will control the vertical resolution while the degree of deviation of the rays from the horizontal will control the lateral resolution of the reconstructed image (Menke,1984).

The position and the shape of the target object also have a role to play for the quality of the reconstruction. Vertically erected features will be resolved less satisfactorily than horizontal ones in a pure crosshole geometry. The resolution will be best for features near the center between the two wells reflecting the fact that many rays cross at that region. In conclusion we cannot expect a perfect solution to the problem at hand. However every effort has to be made, when necessary, to improve the quality of the reconstruction and make the Euclidean distance of the solution as small as possible. Here we will describe, in particular, two techniques that proved promising for improving the quality of the reconstructions. The first is smoothing, the second is data interpolation.

Smoothing was applied as follows: the value of the reconstructed velocity in each pixel in the final solution was substituted by an average velocity the average being taken between the current velocity value in the pixel and the velocities of the immediately neighbouring pixels. Such an averaging procedure is equivalent to a low-pass filtering operation which eliminates high frequency variations within the image. The effect of smoothing is shown in Figure 21a). The quality of the solution has improved and the Euclidean distance has been reduced, however artifacts are still present in the image. We also experimented with weighted smoothing according to which extra weight, when averaging, was given to the center pixel of each cluster. However, the

the resulting improvement of the solution was rather negligible-not more than 1% reduction in the Euclidean distance. The next step was to apply data interpolation by which we mean the following: There are observations of delay times only at the positions of the available hydrophones. However one could interpolate between the available data points to estimate the data at locations between those sampled by the hydrophones. The effect of this is to expand the data set by providing a larger number of equations available for the inversion (corresponding to a more dense ray coverage of the area), while keeping the number of unknown parameters in the problem the same. The interpolation was carried out by using a standard cubic spline technique and an extra data point was introduced midways between each pair of adjacent receivers. The result of the reconstruction after interpolation and smoothing is shown in figure 21 b) demonstrating a drastic improvement in the quality of the reconstructed image. The Euclidean distance has been further reduced and the shape and position of the steam zone have been efficiently established in the solution. Furthermore, the artifacts previously present in the reconstructions have now been eliminated. It took not more than 10 iterations to obtain convergence for this solution, as illustrated in Figure 22. The method is computationally efficient and fast and required only 10 seconds of C.P.U. time-for the solution in figure 21 b)- in the Amdahl mainframe computer at the University of Alberta.

Figure 22.... Diagram showing convergence of the Euclidean distance with number of iterations, for reconstruction in Figure 21 b)

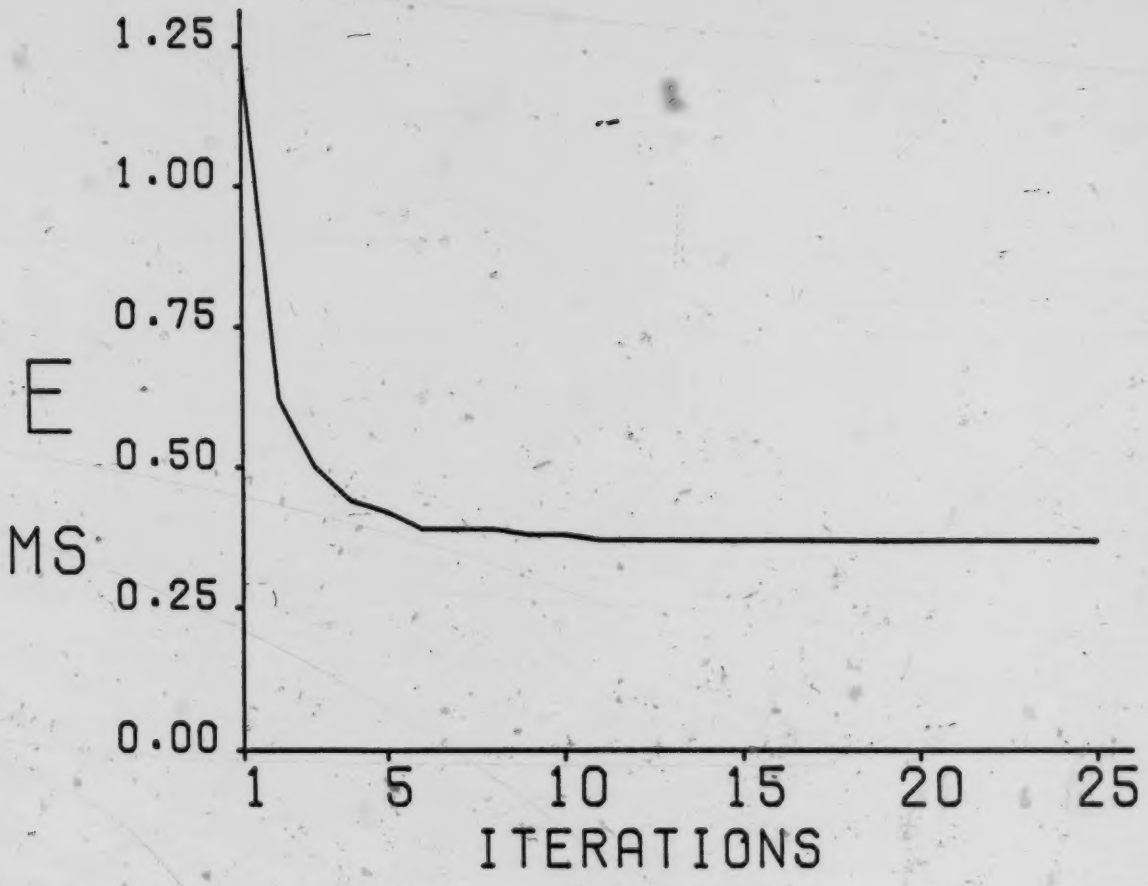
1.25
1.00
0.75
E
0.50
MS
0.25
0.00
1
5
10
15
20
25
ITERATIONS

IV. CHAPTER 3

A. A Seismic tomography experiment

The geometry of the presteam experiment as was executed in the Cold Lake area on June 1985 is shown, in scale, on Figure 23 Two vertical boreholes (source well OB-1 and receiver well OB-4) separated by a distance of 180 m were employed. The wells were cased (7'' casing) but did not have tubing or perforations. Tools were run through 4'' gate valves installed on both the wells. Before proceding with the experiment it was made sure that there was no pressure on the wells. Cement evaluation and correlation logs were run were run in wells OB-1 and OB-4 in the first day of the experiment. The sonic logs, obtained before the wells were cased , are displayed in the Appendix.

The on site equipment during the operation is shown schematically in Figure 24. Seismic data were acquired by a DFS-V seismic recording instrument recording from a fixed downhole string of 24 hydrophones. The sampling fequency was 2,000 samples/second. Low cut filters with a corner frequency of 12 Hz and roll-off 36 db/octave were employed during the recording. Because of limitations in the recording system related to the speed of the A/D converter, only 12 channels could be recorded at a time without having to reduce the sampling frequency. Two additional channels were recorded for timing purposes. The first (auxiliary 1) was recorded from a hydrophone attached to the air gun in

Figure 23.... Geometry of the Cold Lake well-to-well seismic tomography experiment (in scale) also showing direct ray paths.

Air gun pressure 2,300 PSI

Hydrophone spacing 3 m

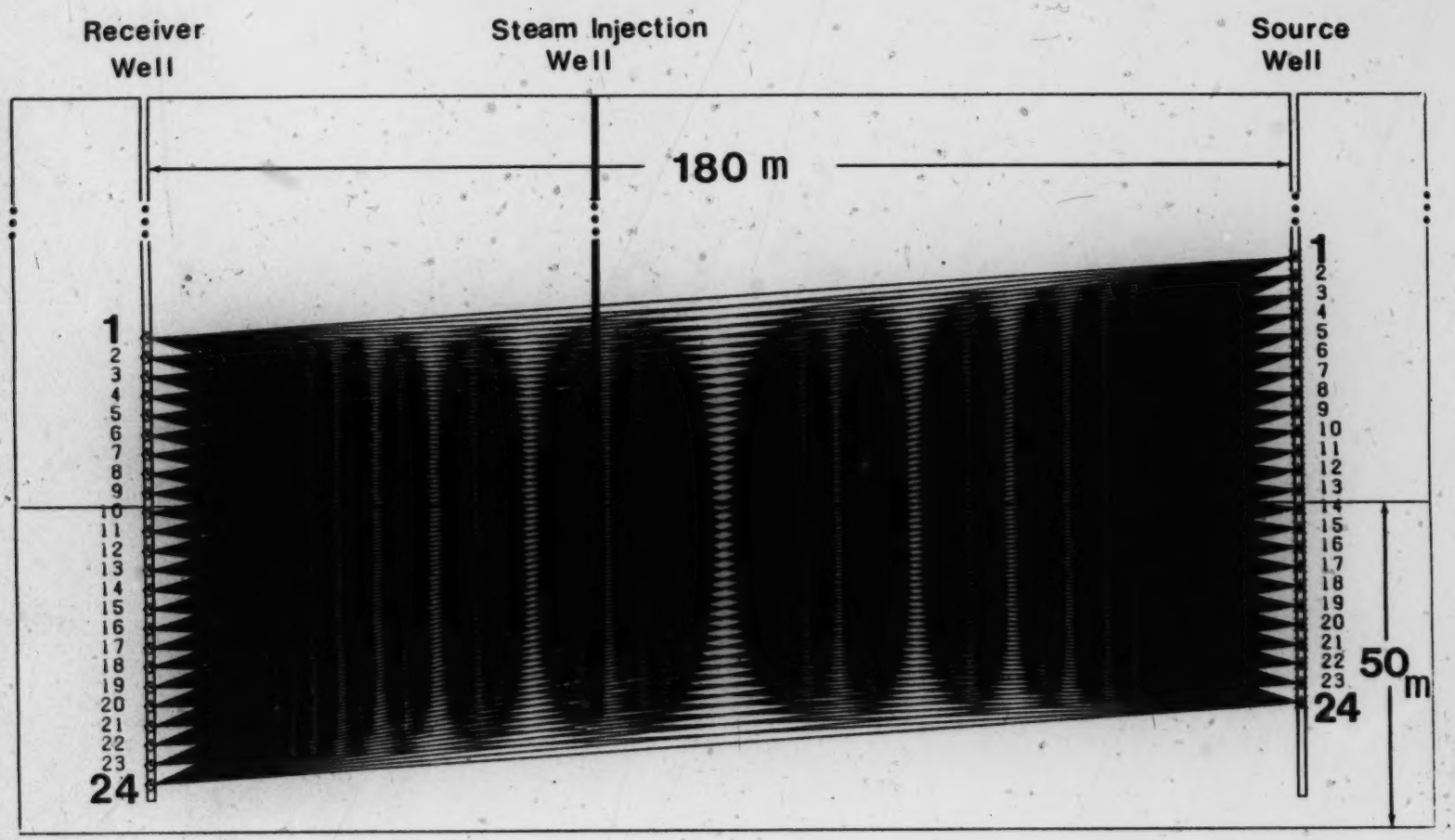

Figure 24.... On site instrumentation for the well-to-well tomography experiment

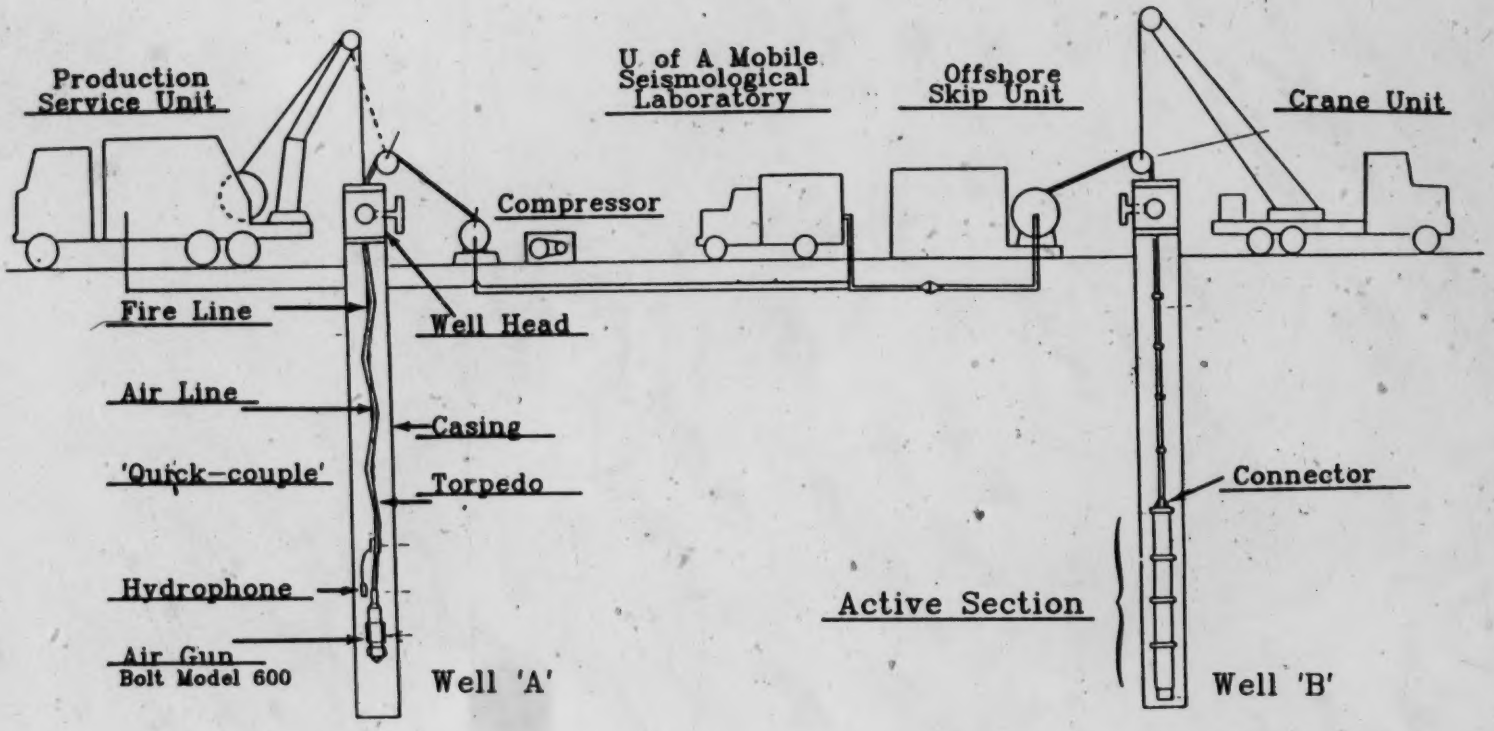
Production Service Unit
U of A Mobile Seismological Laboratory
Offshore Skip Unit
Crane Unit
Compressor
Fire Line
Well Head
Air Line
Casing
'Quick-couple'
Torpedo
Connector
Hydrophone
Active Section
Air Gun
Bolt Model 600
Well 'A'
Well 'B'

order to obtain information on the time break. The time break interval was 5 ms and was found to be consistent throughout the experiment. The second time channel (auxiliary 2) was the shot fire command.

The seismic source was a downhole airgun operating at multiple depths at a pressure of 2,300 PSI. Considerable problems were encountered during the experiment with respect to loading the air gun to the desired pressure of 2,300 PSI. These problems were particularly serious at greater depths (greater than 450 m). No problems were encountered when test shooting the air gun from the surface. It appears that at greater depths proper sealing of the instrument becomes a decisive factor for an efficient operation as the air gun is subjected to the increased pressure of the overlying water column in the borehole. Notice that at depths around 500m the overpressure (pressure of the airgun minus ambient pressure in the borehole) is about 1600 PSI considering a gradient of 0.5 PSI/ft in the fluid column. The spacing at both the sources and hydrophones was 3 m.

The system of 24 sources and 24 receivers provided a dense tomographic coverage of the area under investigation. Source locations spanned the depth interval from 405.3 m to 475.4 m while the string of hydrophones covered depths from 421.4 m to 491.5 m. All depths were measured from the Kelly Bushing (K.B.). To account for the difference between the two K.B. elevations, a small (4m) correction was applied in order to reduce the depth measurements to a common reference

datum plane. The target formation was the Clearwater which has a thickness of 50 m. The experiment will be repeated in an identical manner after several months of steam injection into the Clearwater Formation. The steam injection well was also vertical,positioned 70 m away from the receiver well as shown in figure 23. Furthermore it was offset by 5 meters away from the vertical plane defined by wells OB-1 and OB-4.

Figure 25 shows a typical example of the recorded signals. Clear first arrivals (direct P waves) have been recorded. These are of particular importance for the inversion as we will discuss later. Other prominent arrivals in the records are the events R1 and R2 in figure 25 and the events denoted by 'A','B','C', and 'D' in (Figure 26). All these arrivals have very large amplitudes -as compared with the P-wave amplitudes- and low apparent velocities (1370±70 m/s). They have been interpreted to be tube waves. Notice their lack of a geometrical spreading factor. Events 'A' start as a downgoing tube wave generated from the air gun within the fluid column of the source borehole . At the bottom of the well, an S-wave is generated -according to our ray tracing and time calculations - which is reflected as an S-wave from the basement and impinges at the bottom of the receiver well. At that point an upgoing tube wave is generated which gives rise to the events 'A' of Figure 26. Reverberations of tube waves within the source borehole are also possible in the following sense: upon impinging at the bottom of the source well, the tube wave may also be reflected upwards. Travelling upwards it encounters the

Figure 25.... A typical example of the recorded data up to 250 ms. Source was at a depth of 405.3 m (source #1).

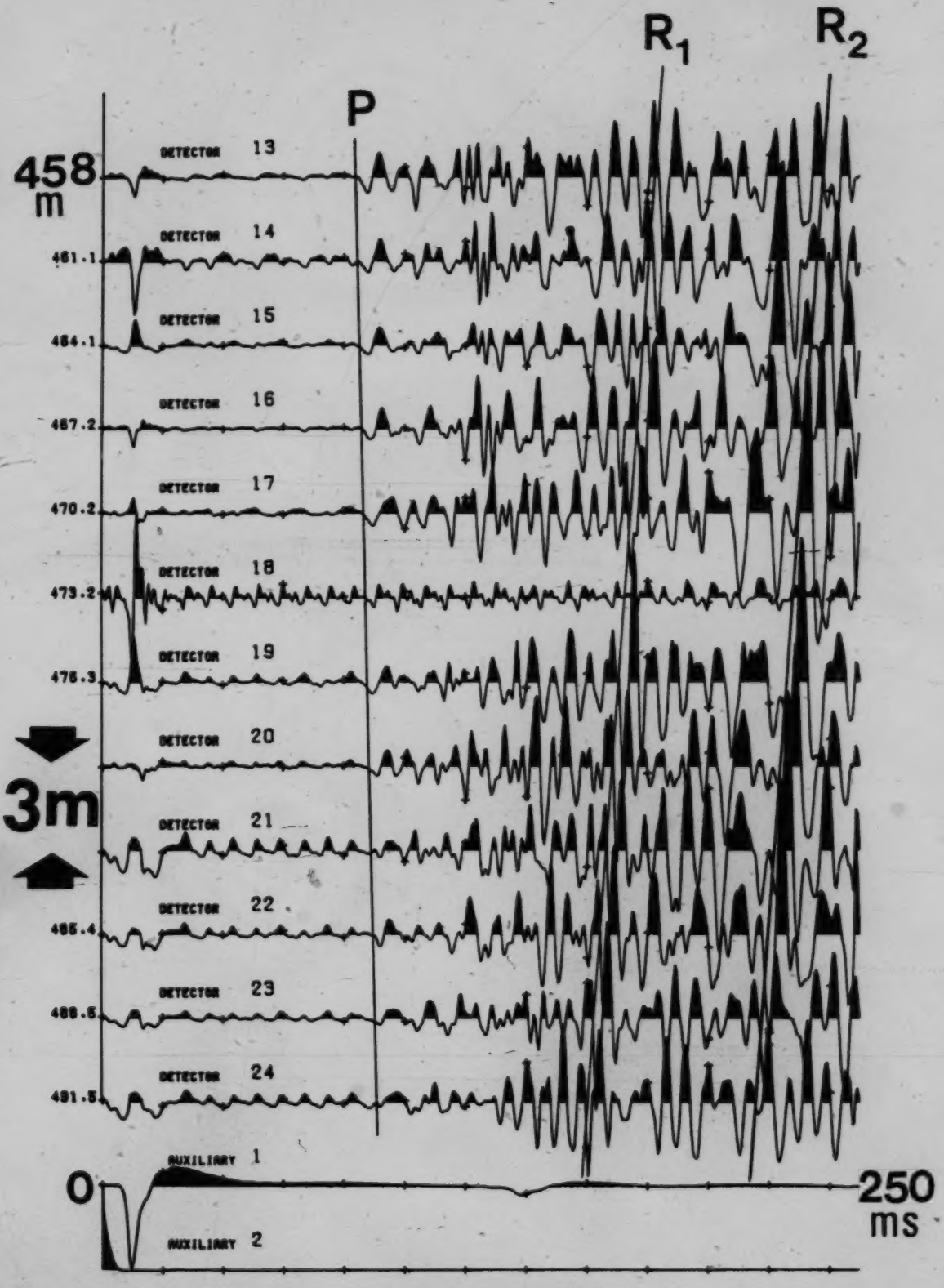
R1
R2
P
458 m
DETECTOR 13
DETECTOR 14
461.1
DETECTOR 15
464.1
DETECTOR 16
467.2
DETECTOR 17
470.2
DETECTOR 18
473.2
DETECTOR 19
476.3
DETECTOR 20
3m
DETECTOR 21
DETECTOR 22
485.4
DETECTOR 23
488.5
DETECTOR 24
491.5
AUXILIARY 1
AUXILIARY 2
0
250 ms

Figure 26.... Recorded seismograms-up to 700 ms- showing tube wave arrivals (A,B,C,D). a):Source at depth of 405.3 m; b)same as in a) but for source depth of 432.7 m Notice the smaller time interval separating events A,B,C,D.

$V_{TUBE} = 1{,}370 \pm 70$ m/s

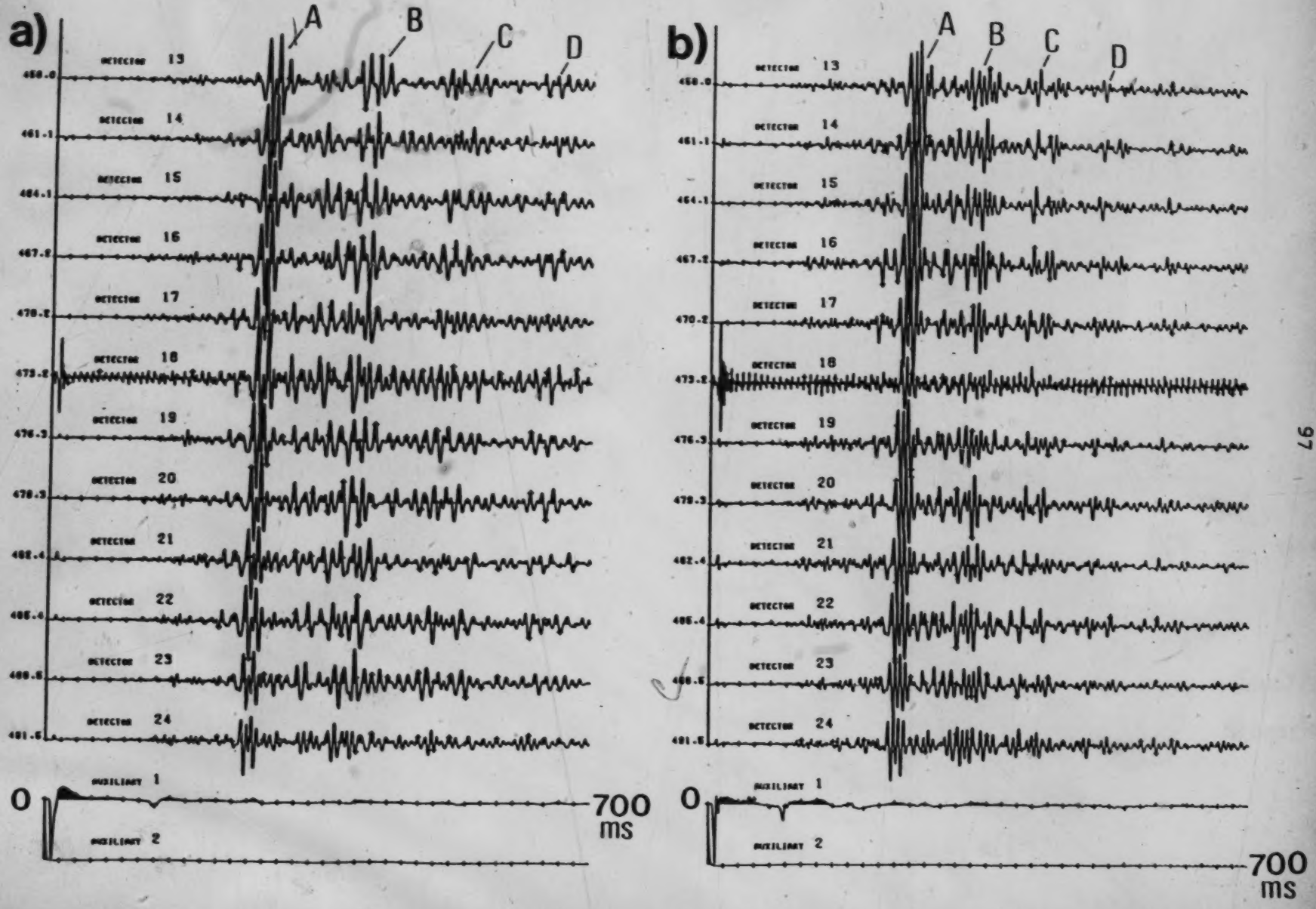

airgun -which completely fills the boreholeand is reflected back downwards. These reverberations of the tube wave within the well give rise to multiple events indicated by 'B','C',and 'D' in our records-see Figure 26 - separated by a constant time interval. This time interval represents the two way time the tube wave takes to travel from the bottom of the well to the position of the airgun and decreases as the airgun is positioned deeper within the source well. Notice also the rapid fall-off of amplitude of these events after each reverberation.

Events R1 and R2 of Figure 25 have been given a slightly different interpretation. They start as S body waves generated at the source, which are reflected at the basement and the top of the Paleozoic and then generate an upgoing tube wave at the bottom of the receiver well. According to our calculations, an S-S reflection at the basement is associated with the R2 events and an S-P conversion at the top of the Paleozoic is associated with the R1 events. It should be pointed out that radiation pattern calculations for a downhole source (Balch and Lee, 1982) indicate that at angles close to 45^0 with respect to the axis of the borehole, S wave amplitudes can be considerably greater than P-wave amplitudes.

The depths of the layers below the Clearwater as well as their interval velocities have been established in the area by deep sonic logs which are included in the Appendix. Reflections from these layers were weak and difficult to identify in the records. This is unfortunate in view of the fact that these events can provide additional sampling of

the region of the reservoir around the injector well. Reflections from the Paleozoic probably do not encounter the heated zone -see for example the P-P reflections in Figure 27. However, notice that the associated rays (they will have zero delay times after steam injection) cross the edges of the reconstruction space within the Clearwater. As a result, several pixels are illuminated from angles that are unattainable from the transmission data. We conclude therefore that reflections from deeper horizons could be used to increase the angular coverage and provide additional constraints for the reconstruction problem even in the case they do not sample directly the heated zone within the reservoir.

A final comment with respect to the tube waves is in order. As mentioned, they were found to propagate within the boreholes at a speed of 1370±70 m/s. This is close to the shear wave velocity in the Clearwater which is 1250 m/s (Poisson's ratio is 0.30). It has been found (Lee and Balch, 1982) that when the tube wave velocity is close to the shear wave velocity in the medium surrounding the well, the effect of the borehole fluid on the body wave radiation pattern can be substantial. Hence it is recommended that in the post-steam experiment the same type of fluid be used in the source well for an effective duplication of the radiation pattern.

Tube waves are usually considered as an annoying type of noise in seismic records. However, as it has already been

Figure 27.... Ray diagram for primary (P-P) reflected events.Layer velocities and depths in the model have been established by deep sonic logs in the area.

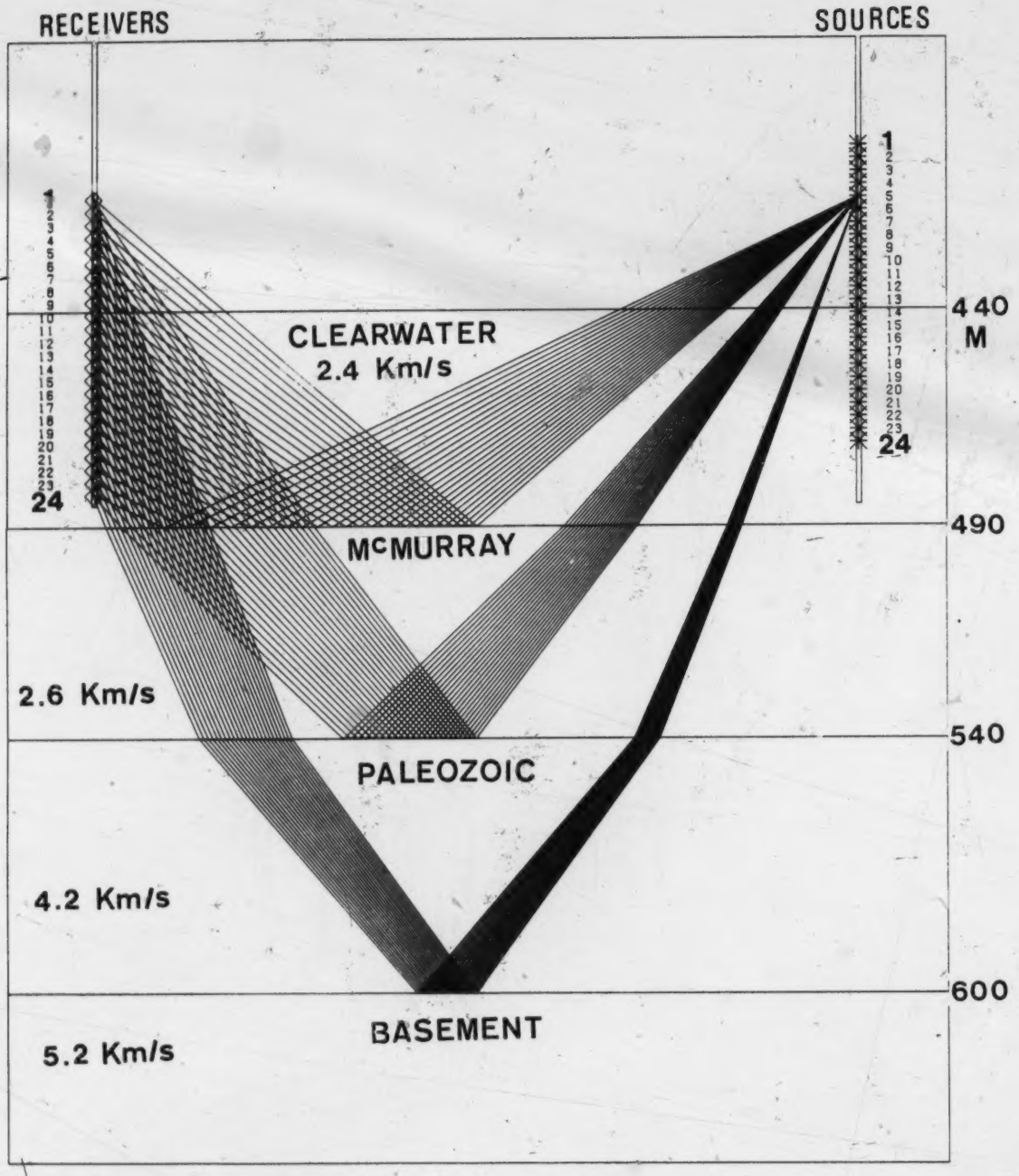
RECEIVERS
SOURCES
1
24
1
24
CLEARWATER
2.4 Km/s
440
M
McMURRAY
490
2.6 Km/s
PALEOZOIC
540
4.2 Km/s
BASEMENT
600
5.2 Km/s

demonstrated in chapter #2, they can be valuable for the purposes of normalizing the pre and post-steam data sets. The mechanisms responsible for the generation of tube waves can vary widely from one experiment to another. However, the important point remains that their ray paths are such that they avoid the relatively small region within the reservoir that is affected by the heat injection.

B. Data processing

Let us now discuss the data processing scheme we propose for the recorded data set. The first step was to apply a low cut filter of 50-500 Hz .The purpose was to eliminate very prominent low frecuency noise in the records caused by oscillations of the string of hydrophones within the receiver well. The second step was to carry out stacking of the records of the repeat shots-which we called external (or vertical) stacking. As many repeat shots as possible (within time and cost limitations) were taken in the field. It was found that repeat shots were quite helpful for stacking purposes because repeatability of the air gun was excellent. This was in contrast with our previous experience with dynamite which showed rather poor repeatability. The next step one would like to be able to take is to carry out stacking between the various channels recorded for the same shot. In order to do that one of course must carry out moveout corrections. However,these moveout corrections for the P waves are expected to be in the order of 0.1 ms, much

smaller than the sampling interval of 0.5 ms. In order to get around this problem, redigitization of the recorded signals was carried out by applying a Fourier tranform technique: first the data were Fourier tranformed using a standard FFT routine. Then,in the frequency domain, they were padded with the desired number of zeros and an inverse Fourier tranform was applied to recover the time series. The resulting redigitized traces had a sampling interval equal to 0.1 ms which was adequate for our purposes. It must be mentioned at this point that extra care must be exercised when padding with zeros in the frequency domain in order to preserve the properties of the digital Fourier tranform (Stanley et al.,1974). After redigitization had been carried out, moveout corrections with respect to the first channel of the shot gather were applied to the P arrivals. These moveout corrections were calculated assuming an average velocity of 2.4 km/s as given by the sonic logs. Then, stacking -internal stacking- was carried out choosing a window of 50 ms. The result was a high quality trace for each shot, showing a clear first arrival P, (Figure 28). Then this P event was cross-correlated with the original P events of all the channels of the shot gather. A typical example of the results of the cross correlation are shown in Figure 29. There is a clear shift, from channel to channel, of the peak of the cross correlation function. This shift could be measured easily and provided an effective means of an accurate determination of the first arrivals.

Figure 28.... Trace resulting after internal and external stacking.

FILTER 50 - 500 Hz

External stacking (2-fold)

Redigitization $f' = 5 \cdot f_o = 10{,}000$ Hz

Internal stacking (12-fold)

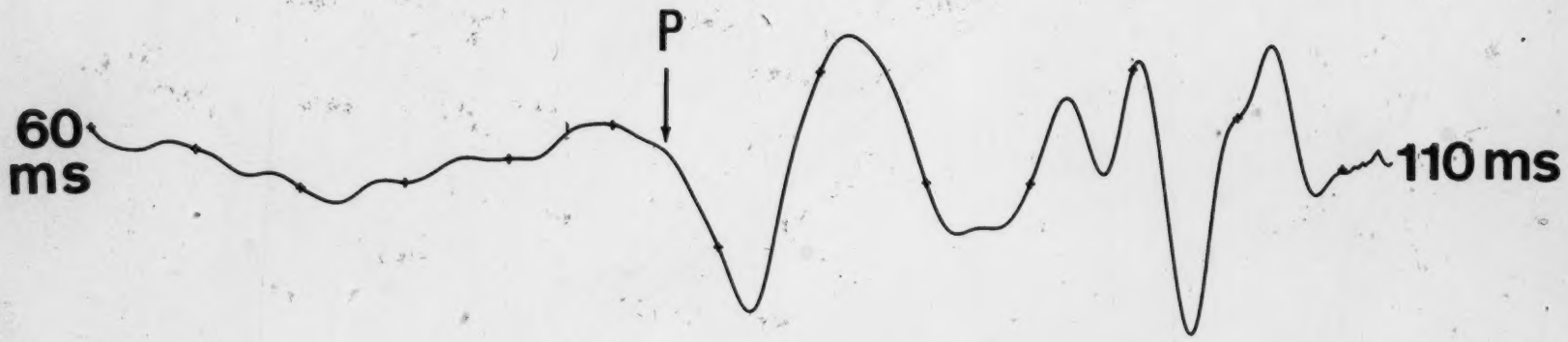

4 ms between markers

Figure 29.... Cross-correlation of trace in figure 28 with channels 1 to 12 from source #1.

Cross Correlation

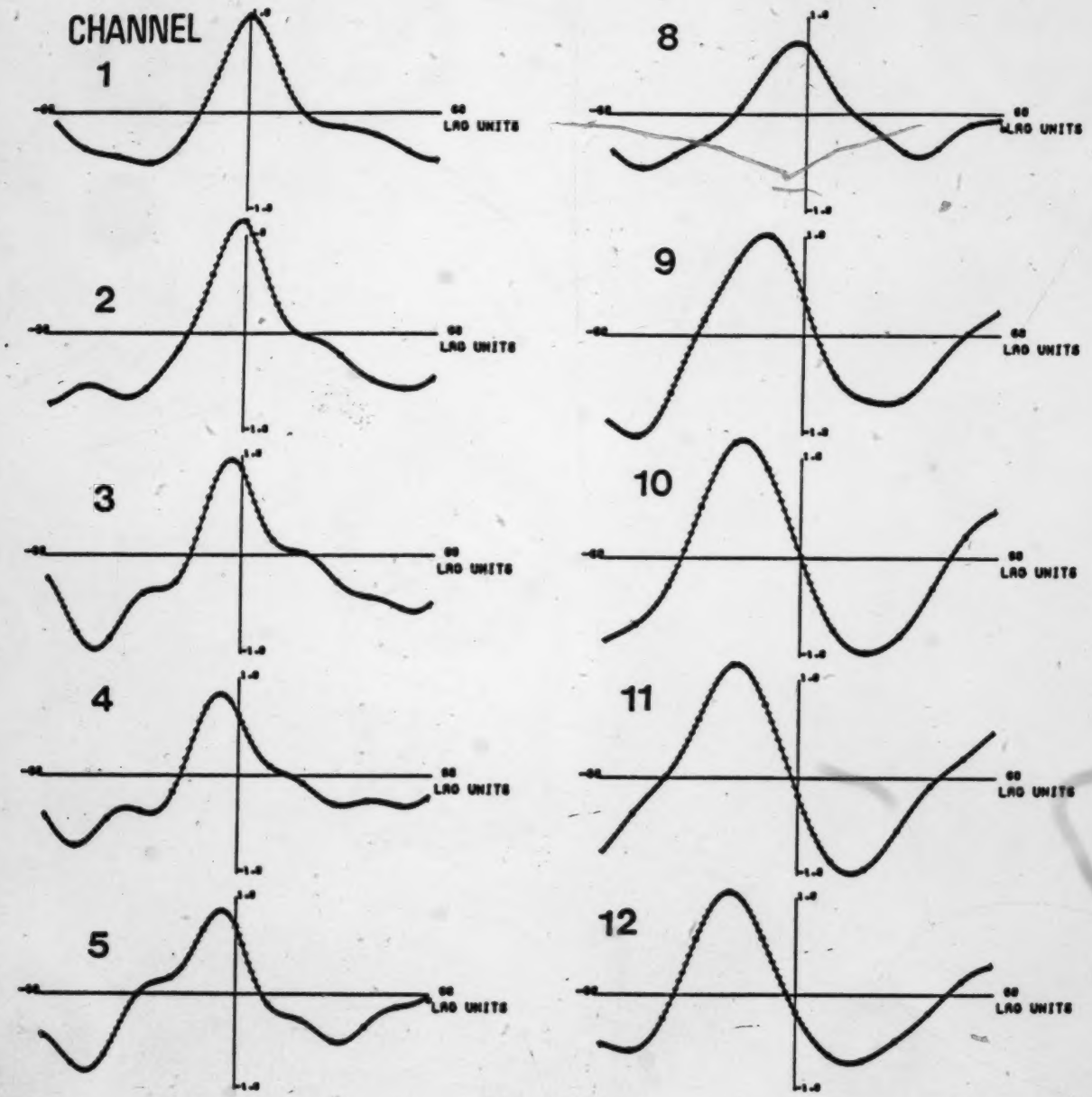

C. Inversion of the presteam data

After the first arrival times had been determined, the next step was to invert them in order to establish the distribution of the velocity field between the two boreholes, and for testing the performance of our reconstruction algorithm with real data. The mechanics of the inversion are basically along the lines described in earlier paragraphs with the exception that, due to the absence of post-steam data, absolute P-arrival times instead of delay times must be inverted. Hence, the reconstruction quantity is the slowness field instead of the differential slowness field. Furthermore, in this case one has to reconstruct the entire space between the two boreholes. We decided, for the purposes of the inversion, to consider only the high quality rays in which it was possible to determine first arrivals with an accuracy of ±0.5 ms equal to the sampling interval. The result is that some rays are missing in the ray diagram of Figure 30 However still a large number of rays (359) criss crossing the area under investigation is obtained and a smaller number (139) of pixels to determine, the pixel size being chosen to be 10 m.

The results of the reconstruction indicated one particularly interesting feature: The inversion velocities of the pixels adjacent to the two wells were consistently lower than the velocities obtained from the sonic logs at the same locations. The inversion suggested an average velocity of 2.36 km/s for the column of pixels adjacent to

Figure 30.... Ray diagram of the presteam experiment. Rays of low signal-to noise ratio are not included in the diagram.

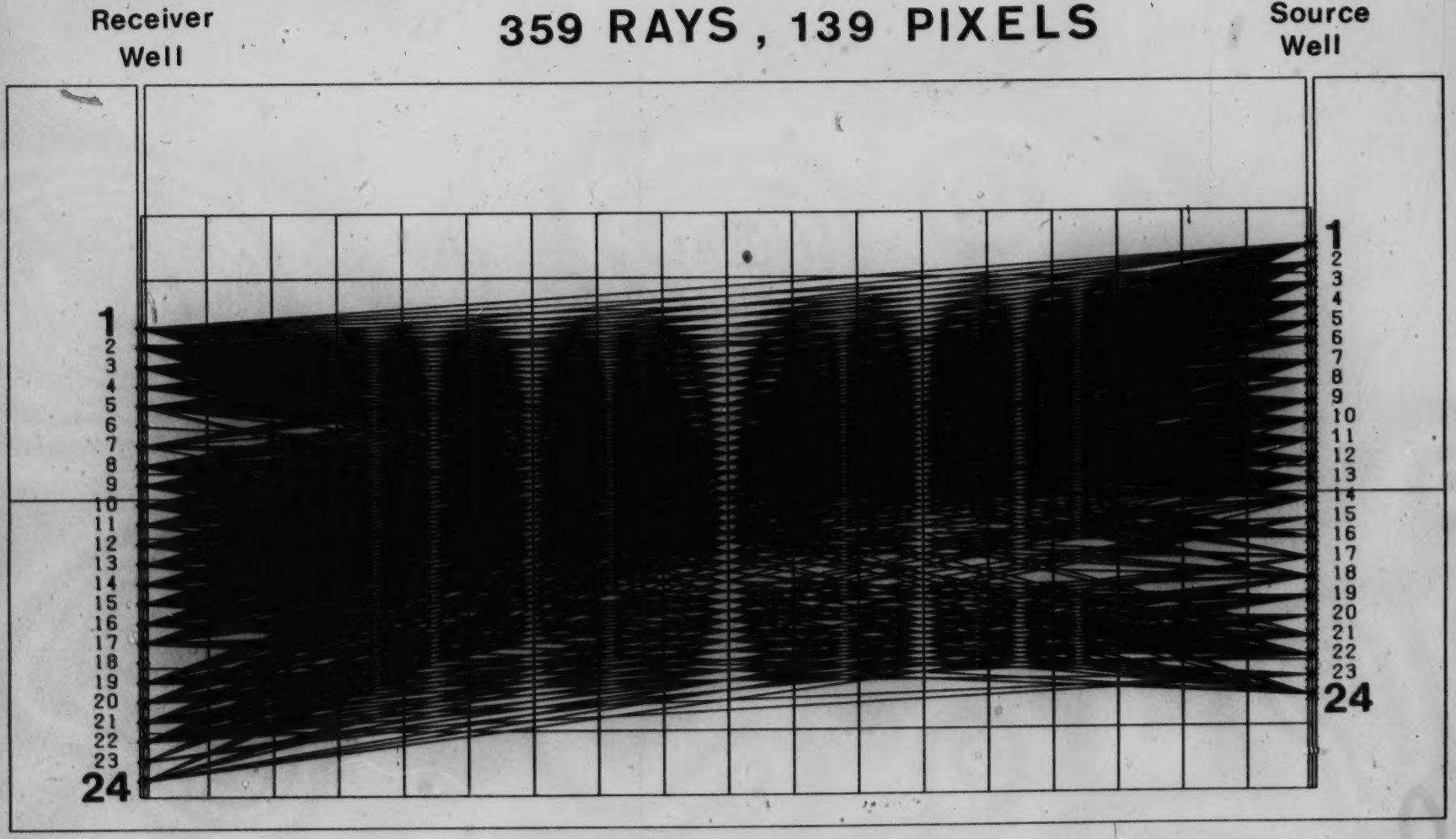

PIXEL SIZE 10 m

the receiver well in contrast to an average sonic log velocity of 2.42 Km/s at the same column. The corresponding values for the source well were $V_{inversion}$ =2.36 km/s and V_{sonic}=2.45 Km/s. These differences between sonic log velocities and velocities determined from the seismic inversion should be attributed to dispersion effects. Similar discrepancies between seismic and sonic velocities, due to dispersion, have been reported by Stewart et al. (1984).

Dispersion is a necessary phenomenon in every attenuating medium. Neglecting dispersion would result in the presence of non-causal seismic arrivals. A variety of attenuation laws have been proposed in the literature (Azimi,1968, Aki and Richards,1980, Futterman,1962, Kjartansson,1979) from which dispersion effects have been determined. The results show clearly that dispersion decreases with increasing Q and that higher frequencies propagate with greater velocity. This explains the fact that our sonic velocities are greater than the inversion velocities. Sonic logs were obtained at frequencies around 20 KHz much higher than the observed frequencies of our seismic arrivals.

The next step was to estimate the dimensionless attenuation factor Q of the medium , using Azimi's law of attenuation:

$$V(f_1)/V(f_2)=1+(\pi Q)^{-1}Ln(f_1/f_2) \qquad (1)$$

The assumption behind this derivation (Aki and Richards,1980) is that there is a linear dependence of attenuation with frequency. This can be a questionable assumption, if a very wide frequency band is considered, but a useful first approximation. In equation (1), f_1=20,000 Hz, and f_2 of the observed seismic pulses, used in the inversion, was approximately 125 Hz. $V(f_1)$ and $V(f_2)$ are the sonic and inversion velocities respectively. Before substituting the known parameters in equation (1), one word of caution is in order: Inversion velocities were obtained from rays which travelled mostly horizontally, while sonic log velocities were obtained from vertical ray paths. Hence a negative anisotropy correction must be applied to the inversion velocities before inserting them in equation (1). The purpose of the correction is to take into account the observation that seismic velocities along bedding planes are typically a few percent greater than velocities measured perpendicularly within the same lithologic unit (Thomsen,1986). The obtained Q values plotted versus anisotropy corrections up to 5% are shown in Figure 31. A Q value equal to 30 is supported by the results of chapter 4. Notice that a Q equal to 30 corresponds to a 3% anisotropy according to Figure 32.

Given this value of attenuation a second pass to the inversion algorithm was performed according to the following procedure: The sonic log velocities for the columns of pixels adjacent to the two wells were corrected for

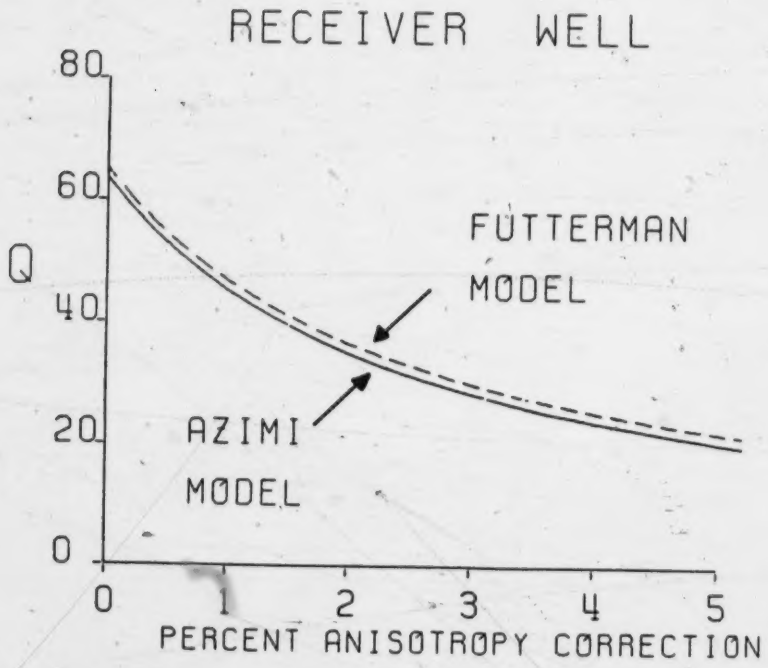

Figure 31....Q calculations versus percent anisotropy corrections for Azimi and Futterman attenuation laws.

dispersion using equation (1) and according to Q=30. These corrected velocities were incorporated as a priori knowledge in the image and were not altered during the iterative inversion process. The iterations were stopped upon convergence of the reconstruction error and the solution was selected to be the one with the smallest Euclidean distance. Then the reconstruction was subjected to radial smoothing along the lines suggested earlier in the thesis, in the computer simulation examples. The final result is shown in Figure 32 which makes use of a color scale for displaying the reconstructed velocities. Convergence was obtained after three iterations. This reconstruction (Euclidean distance=0.49) represents an improvement over the initial inversion which had a Euclidean distance of 0.61 ms and was obtained without incorporating sonic log information and without smoothing. We also experimented with smoothing after each iteration instead of smoothing the solution obtained after the last iteration. However these efforts provided inferior results (Euclidean distance greater than 0.49 ms).

The dominant velocity range , in the reconstruction shown in Figure 32, is from 2.30 to 2.38 Km/s (yellow color) although there are regions with higher velocity (green color). There is also a localized lower velocity zone (red color) at the bottom of the Clearwater.

It should be pointed out that the assumption underlying the choice of the Euclidean distance (L_2 norm) as a measure of discrepancy, is that the errors in the measurements obey

Figure 32. Inversion of the recorded presteam P-arrivals using ART (Algebraic Reconstruction Technique). The result shown was obtain after three iterations and radial smoothing. The two columns close two the source and receiver wells indicate the sonic log velocities. These corrected for dispersion, on the basis of Q=30, were incorporated as a priori knowledge in the solution.

Q= 30 E= 0.49 MS

PIXEL SIZE
10 M

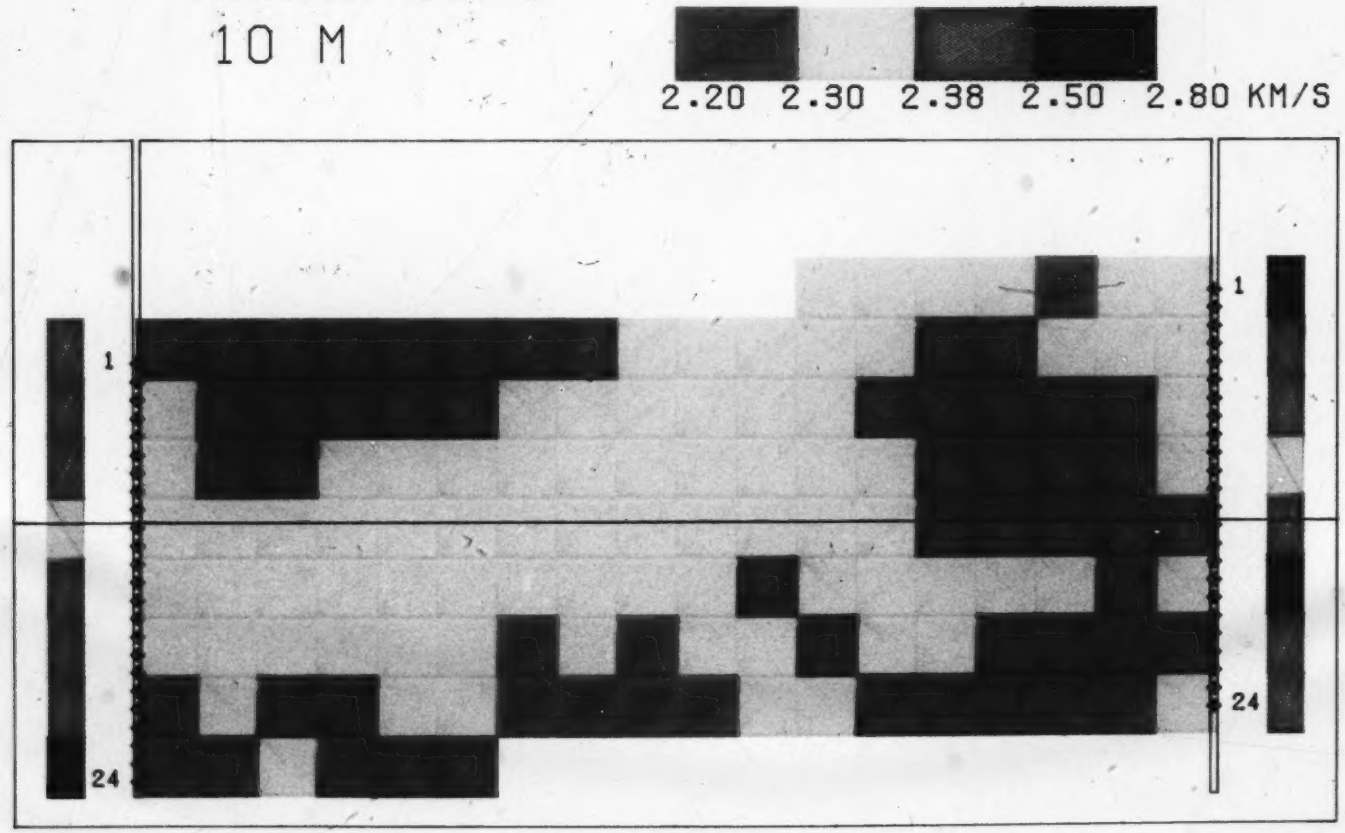

the Gaussian distribution. For long-tailed non-Gaussian distributions, other criteria based on minimization of the sum of absolute residuals (L_1 norm) may be more effective. A histogram plot of the residuals of the above reconstruction of the tomography data, plotted at intervals of 0.1 ms versus their population number, revealed a fairly good agreement with a Gaussian distribution. Large positive or negative residuals (0.7-0.8 ms) had a population of 5 while the population of small residuals (-0.1 to 0.0 ms or 0.0 to 1.0 ms) was as large as 36. These results seem to justify our choice of the Euclidean norm criterion.

V. CHAPTER 4

A. Introduction

Seismic attenuation properties of rocks can be investigated by laboratory studies. Such studies employ frequencies in the kilo and megahertz range in order to determine physical properties of very small samples, but interpreting these results in terms of behavior at seismic frequencies is problematic. The reason is that the mechanisms responsible for attenuation at ultrasonic frequencies may be entirely different from those in the seismic band. In addition, one would like to have information on the spatial variation of attenuation without having to obtain core samples. Therefore, of more interest are in situ studies of seismic attenuation.

In this chapter we will present Q values calculated by a variety of techniques using the well-to-well seismic measurements that have already been presented in this thesis.

B. Q measurements from the presteam tomography experiment

a) Using the spectral ratio method

Our procedure for measuring attenuation involved the spectral ratio method. The technique requires the choice of a reference downhole pulse and the construction of spectral

ratios between this and another downhole pulse. It has been applied successfully for measuring attenuation from vertical seismic profiles, (Hauge, 1981).

Applying the same technique to our hole-to-hole seismic profiles can be more problematic. Due to the geometry of the experiment, see Figure 23, the range over which the various distances between source and receiver vary is limited. As a consequence, the success of the spectral ratio method will rely heavily on the good match between the frequency responses of the receivers. However, the use of a string of hydrophones receiving seismic pulses from a single shot is in favor of meeting this requirement.

Let us call x_0 the distance a seismic ray travels from source #1 to receiver #1 and x the distance between the same source and receiver #24. The sonic logs indicate that there is no velocity contrast between the Clearwater formation and the formation above it (Grand Rapids). Hence no refraction of seismic rays is expected to occur at the interface. The amplitude of the seismic pulse at distance x_0 will be given by

$$A(x_0)=G(x_0)\exp(-\pi f x_0/v_p Q) \quad (1)$$

and the amplitude at distance x will be

$$A(x)=G(x)\exp(-\pi f x/v_p Q) \quad (2)$$

where f is frequency (in Hz), v_p is the phase velocity of the P-wave and Q is the quality factor of the medium characterizing its intrinsic attenuation. G(x) is a frequency independent function incorporating the effects of: 1) Spherical divergence, 2) dependence of the pulse amplitude on impedance,(Treitel and Robinson,1966), 3) source strength and recorder's gain, and 4) angular dependence of the radiation pattern, (Fehler and Pearson,1984).

In order to construct spectral ratios between the two pulses we take the logarithm of the ratio of the two amplitudes at each frequency, choosing the pulse at x_0 as reference. Then:

$$\mathrm{Ln}\{A(x_0)/A(x)\}=\mathrm{Ln}\{G(x_0)/G(x)\}+(x-x_0)\pi f/Qv_p \qquad (3)$$

A plot of $\mathrm{Ln}\{A(x_0)/A(x)\}$ versus frequency f will yield a linear graph from the slope of which the value of Q can be calculated. The implication is that Q and v_p are frequency independent. This can be a questionnable assumption if a wide range of frequencies is considered but a useful first approximation for our purposes. As mentioned in Chapter 1, Liu et al. (1976) have shown that a superposition of 12 different relaxation mechanisms can in fact yield a constant Q over seismic frequencies. The power spectral estimates for the two P-wave pulses and their spectral ratios plotted versus frequency are shown in Figure 33. From the slope of

Figure 33.... Power spectra and spectral ratios of the P-wave pulses recorded at receivers #1 and #24 from source #1 of the presteam tomography experiment.

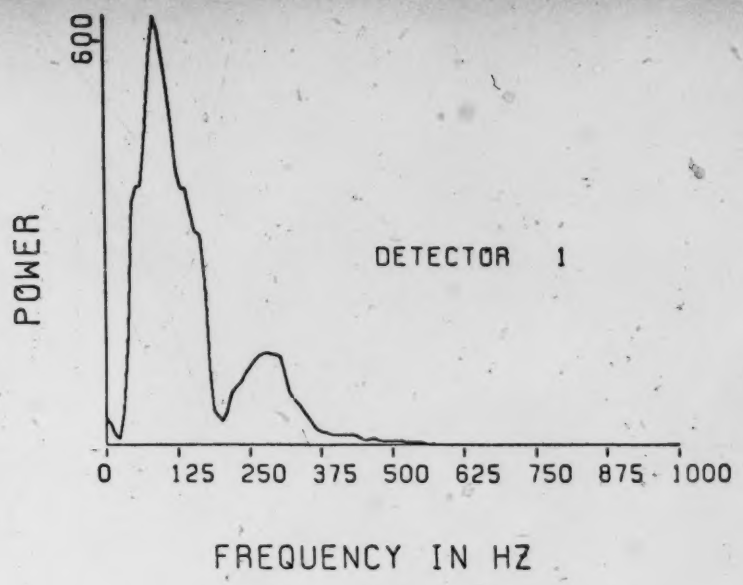
600
POWER
DETECTOR 1
0 125 250 375 500 625 750 875 1000
FREQUENCY IN HZ

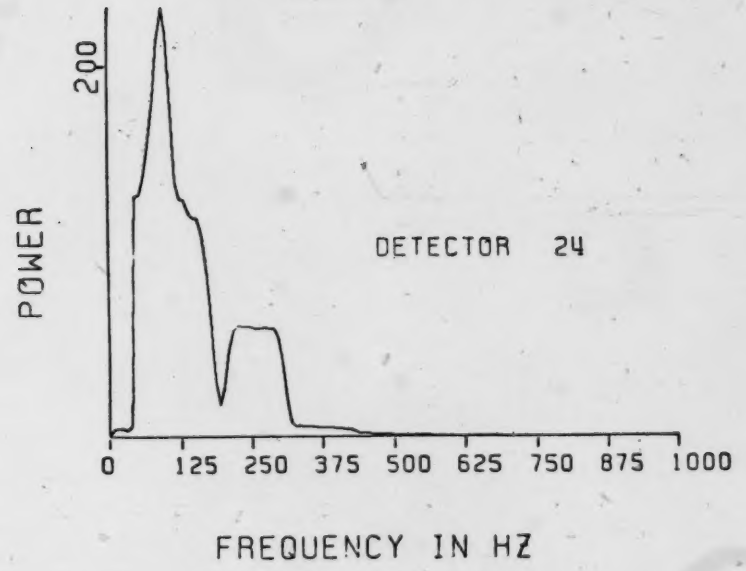
200
POWER
DETECTOR 24
0 125 250 375 500 625 750 875 1000
FREQUENCY IN HZ

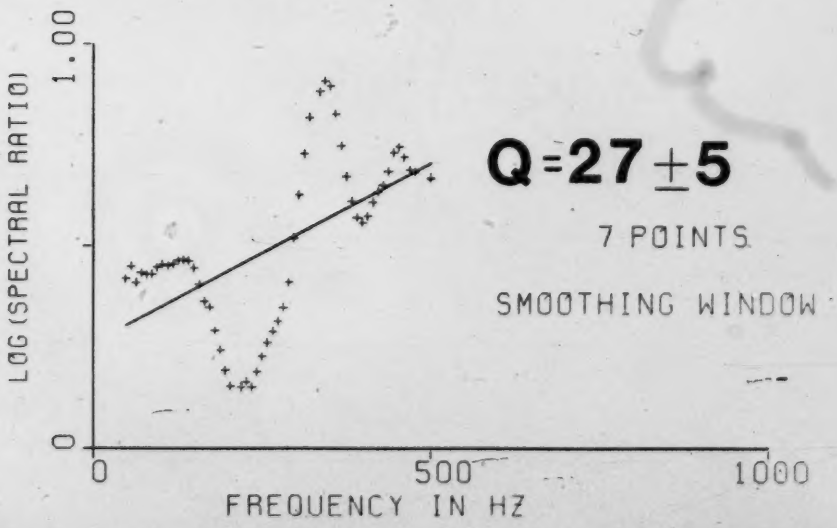
1.00
0
LOG (SPECTRAL RATIO)
0
500
1000
FREQUENCY IN HZ
Q=27±5
7 POINTS
SMOOTHING WINDOW

the spectral ratio graph the value of Q was found to be equal to 27±5. The various steps that were taken for reaching this result are summarized as follows:

1) A cosine bell taper window 80 points long (40 ms) was applied to the P-wave phases. Tapering is particularly essential for the study of individual phases in seismology in order to minimize the effects of other phases and to avoid large discontinuities that may occur at the beginning and the end of the data vector, (Kanasewich, 1981). Prior to this operation the low frequency noise -up to 40 Hz- which was prominently present in the records was eliminated through bandpass filtering.

2) The data vector was padded with zeros until the total number of points in the time series was equal to $N'=256(=2^8)$. The D.C. component of the time series was removed and the power spectrum was calculated using a Fast Fourier transform and a Daniell (1946) window in the frequency domain. The result is given by

$$P(W)=\{N'/N(2m+1)\}\sum_{j=-m}^{j=+m}\{F(W-j)F^*(W-j)\} \qquad (4)$$

$$W=0,1,2,\ldots N'/2$$

where N=80, N'=256 and m was chosen equal to 4. The star indicates a complex conjugate .

3) Statistical analysis of the spectral ratios was carried out in order to determine the probable error of the distribution. Then, any data points with residuals exceeding

five times the probable error were discarded, (Margenau and Murphy, 1955). However, very few measurements qualified for such a rejection. Subsequently, the spectral ratio versus frequency graph was smoothed using a moving average window 7 points wide. Then a linear least squares fit was applied to the data. A Q value of 27±5 was obtained from the slope of the linear trend and equation (4). V_p was 2400 m/s .

At frequencies higher than 150 Hz the spectral ratios oscillate around the linear trend of the graph. This is probably caused by geological interference. For instance, although velocity contrast at the top of the Clearwater is zero, impedance contrast may be different than zero. Hence, very low amplitude reflections are possible from that interface interfering with the spectral estimates of the P-wave pulse arriving at receiver #1. Other interference is possible in the form of intrabed multiples from a number of high velocity carbonate stringers present in the Clearwater. These are clearly visible in the sonic logs. They are rather randomly distributed within the formation and are laterally discontinuous. They are quite thin-about 2 m- hence they will be visible only to the high frequencies of the seismic energy. The fact that oscillations of the spectral ratios occur at high frequencies indicates that they are possibly caused by interference from these high velocity carbonate stringers. If one wants not to include the oscillatory portion of the spectral ratios in the calculation of Q, in which case the frequency range from 40 Hz to 150 Hz is to be

considered, then the Q value obtained is 37±7.

It is of interest to mention that Schoenberger and Levin (1978) have tested and confirmed the effect of geological interference on spectral ratio calculations by constructing synthetic seismograms from sonic and density logs.

b) Using the concept of average frequency

Due to preferential absorption of higher frequencies, the shape of a travelling seismic pulse changes with distance from the source. Hauge (1981) has shown that the rate of change is dependent upon the attenuation according to the formula

$$d\langle f\rangle_x/dx=-(2\pi/Qv)\{\langle f^2\rangle_x-\langle f\rangle_x^2\} \qquad (5)$$

where $\langle f\rangle_x$ is the average frequency of the pulse at distance x from the source. The quantity in the bracket in equation (5) is equivalent to the variance function $\sigma_x^2=\langle(f-\langle f\rangle_x)^2\rangle_x$ which is always a positive number . Hence the rate of change of $\langle f\rangle_x$ in equation (5) is always negative. In addition, at greater attenuation (smaller Q) the rate of change will be increased. Notice that the $\langle f\rangle_x$ curve does not depend upon a reference depth. Furthermore, the $\langle f\rangle_x$ curve makes use of information obtained from many channels unlike the spectral ratio method which involves the analysis of only two pulses.

A plot of P-pulse average frequency versus shot-to-receiver distance-for source #1 of the experiment - is shown in Figure 34 The average frequency for each pulse was calculated according to the definition given by Sheriff (1973):

$$\langle f\rangle_x = \Sigma_i f_i \{A_x(f_i)\}^2 / \Sigma_i \{A_x(f_i)\}^2 \quad (6)$$

where $\{A_x(f_i)\}^2$ is the power spectrum of the pulse at distance x from the source. The summation was carried over all the discrete frequencies f_i up to the Nyquist frequency.

According to equation (5) $\langle f\rangle_x$ must be a monotonically decreasing function of the shot-to-receiver distance otherwise negative values of Q will be encountered. From the slope of the function the value of the attenuation can be calculated at each point of the graph. For the data shown in Figure 34, the closest curve to give a monotonic decrease of $\langle f\rangle_x$ is a straight line . This was calculated according to a least squares fit. In this case $d\langle f\rangle_x/dx$ is a constant equal to the slope of the linear trend. Hence σ_x^2 must be a constant too, provided Q is a constant, and was taken to be equal to the average variance of all the 24 recorded pulses originating from source #1. Alternatively one could let σ_x^2 be a variable in which case a different Q value would be obtained from each point of the $\langle f\rangle_x$ versus x graph. Then one can compute an average Q for the examined depth interval. However, Q is not expected to to vary

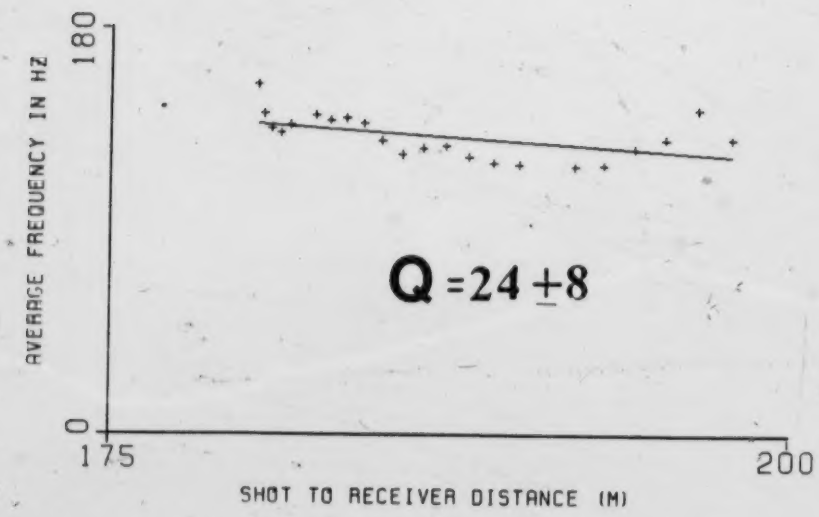

Figure 34.... Downhole pulse average frequency versus shot to receiver distance for source #1 of the presteam tomography experiment.

significantly within the depth range considered.

From the values of the slope=-0.80 $(s\ m)^{-1}$, the average variance =7300, and the P-wave velocity of 2400 m/s, a value of Q equal to 24±8 was obtained . This is in good agreement with the value of Q which was obtained by the spectral ratio method.

C. Calculation of Q within the steam zone

Our intention is to make use of the seismic data obtained from the before and after steam injection experiment of chapter 2.

Our purpose here is to show that a modified spectral ratio technique can be used in order to calculate values of seismic attenuation in the steam invaded zone. Let us consider the ray path to receiver #1 of the 'before' and 'after' experiment of Figure 3 (chapter 2). The 'before' amplitude of the P-wave pulse will be given by

$$A_x(f)=G(x)\exp(-\pi fx/Q_p v_p) \qquad (7)$$

where x is the distance between source and receiver. G(x) has the same meaning as in equation (1). Q_p is the intrinsic P-wave attenuation of the medium through which the seismic ray has travelled. In the post-steam case the seismic ray will travel a certain distance Δx through the steam zone. Then the 'after' amplitude of the pulse, assuming the total

length of the raypath is still x, will be given by :

$$A_x'(f)=G'(x)\exp\{-\pi f(x-\Delta x)/Q_p v_p\}\exp\{-\pi f\Delta x/Q_p' v_p'\} \qquad (8)$$

Notice that G(x) will not necessarily be identical to G'(x) mainly because of the reflectivity at the boundary of the steam zone. Hence the spectral ratio graph is expected to show a small positive intercept with the $\mathrm{Ln}\{A_x(f)/A'_x(f)\}$ axis, after normalization of source strength and recorder's gain has been performed. Taking the ratio of equations (7) and (8) and simplifying we obtain:

$$\mathrm{Ln}\{A_x(f)/A_x'(f)\}=\mathrm{Ln}\{G(x)/G'(x)\}+\pi\Delta x\{(1/Q_p' v_p')-(1/Q_p v_p)\}f \qquad (9)$$

where Q_p, V_p and Q_p', V_p' denote the values of seismic attenuation and velocity outside and inside the steam zone respectively. Then, from a plot of $\mathrm{Ln}\{A_x(f)/A_x'(f)\}$ versus frequency f, the value of Q_p' could be calculated from the slope of the graph, provided the values of V_p, V_p', Δx and Q_p are known. V_p was close to 2400 m/s. Q_p was found in the previous paragraphs to be close to 30. A drop of 20% in the P-wave seismic velocity is assumed to occur within the steam-zone,(Tosaya et al.,1984), hence V_p'=2000 m/s. Then from the observed P-phase delay of 1 ms at receiver #1 and from

$$\Delta T_p=\Delta x(1/v_p'-1/v_p) \qquad (10)$$

Δx was found to be equal to 12 m. A plot of logarithm of amplitude ratio of the 'before' and 'after' pulses at receiver #1 versus frequency is shown in Figure 35. Attenuation was calculated from

$$Q_p' = \pi \Delta x Q_p v_p / \{(a Q_p v_p + \pi \Delta x) v_p'\} \qquad (11)$$

where a is the slope of the least squares linear trend of the graph. Substitution of the known parameters in (11) gave $Q_p' = 7 \pm 2$. The frequency band considered was 30-240 Hz. We repeated the above calculation for the 'before' and 'after' seismic pulses arriving at receiver #2. In this case ΔT_p was 2 ms hence $\Delta x = 24$ m. The plot of spectral ratios versus frequency is also shown in Figure 35. The frequency band considered was from 30 to 220 Hz. The calculation gave a value of Q_p' equal to 8 ± 2 .

These low values of Q_p' suggest considerable amounts of attenuation of the seismic signals through the steam zone. This could be explained by the increased saturation of viscous fluids (mobilized heated bitumen) as well as less viscous ones (steam condensate) within the zone affected by the steam injection. It should be emphasized that the bitumen in the Clearwater is immobile under undisturbed reservoir conditions and from a hydrological point of view can be considered as part of the skeleton because it reduces the permeability of the formation to water by a factor of at least 100 with respect to the permeability of clean sands

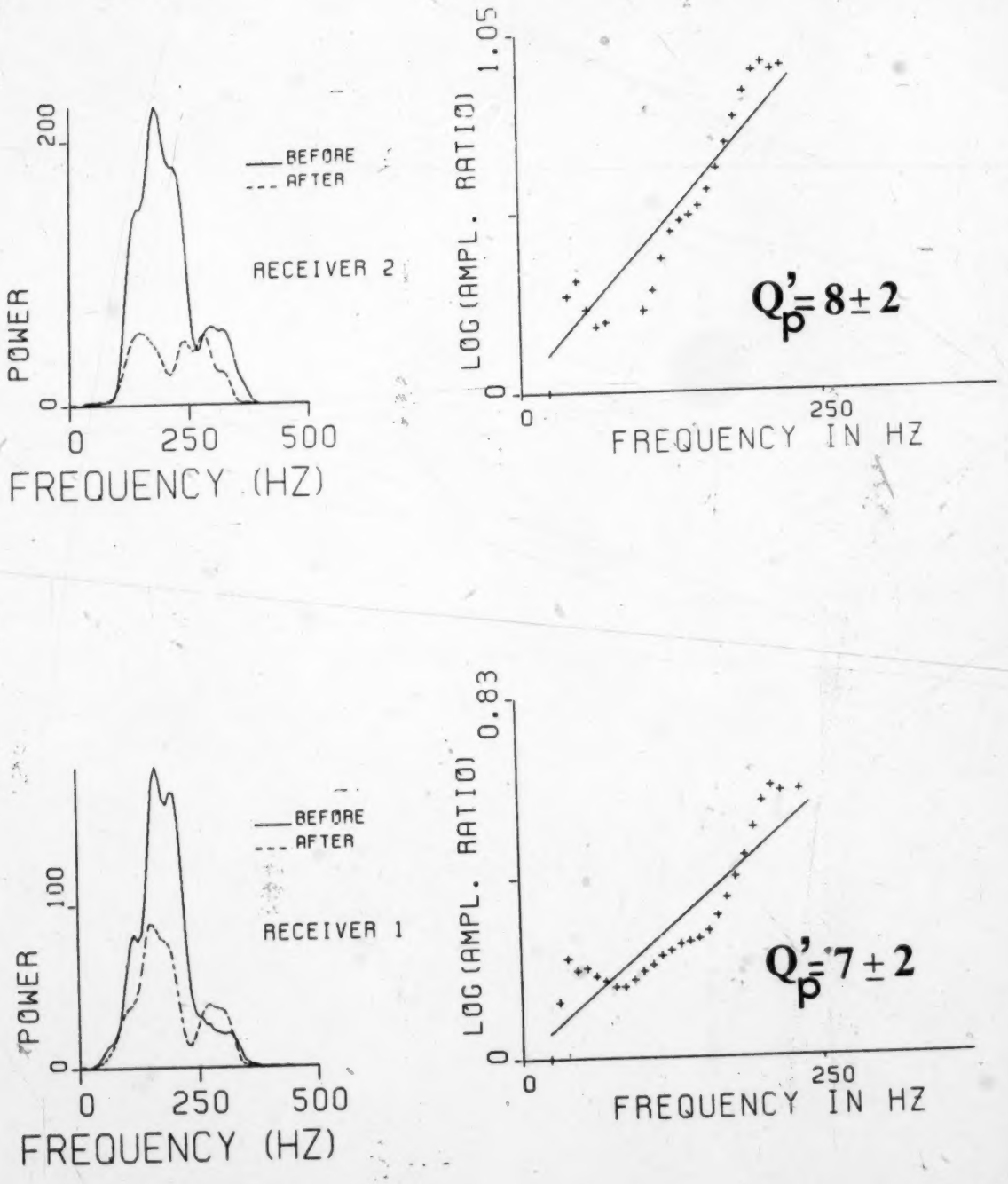

Figure 35.... Before and after power spectra of the P-pulses at receivers #1,#2, and their spectral ratios plotted versus frequency.

similar to the McMurray Formation (Harris and Sobkowicz,1977).

Normally, since attenuation Q^{-1} is proportional to viscosity , one should expect a drop in attenuation at higher temperatures. However, at elevated temperatures bitumen is able to flow with the result that permeability increases dramatically. This could explain our low Q values in the heated zone , in view of the fact that attenuation increases with permeability, as mentioned in Chapter 1. In addition, the increased microcrack porosity created in the heated zone by the injection of highly pressurized steam is expected to further contribute to an increase of attenuation in the anomalous zone.

Notice, in figure 35, that in the frequency range of 140-200 Hz, the spectral ratios indicate a linear regression trend with greater slope, hence lower Q and higher attenuation. This might come in support of recent theoretical and experimental results showing evidence of an absorption peak at high frequencies beyond which attenuation decreases, (Winkler and Nur, 1982, Jones and Nur, 1983). This peak is theoretically predicted for a single relaxation time or a very narrow distribution of relaxation times. According to results reported by Jones (1986) this absorption peak is expected to occur, for a tar sand material at temperature of 200 ^{0} C, at frequencies close to 300 Hz. At normal reservoir temperatures the characteristic frequency is shifted towards much lower values, (around 3

Hz).

Additional evidence of increased fluid saturation in the steam zone was provided by the following calculation: Clear 'before' and 'after' S-wave pulses have been observed in the records of receiver #2, in addition to the P-waves (see Figure 5). While P-wave delay after injection was 2 ms in these records, the delay for the S-pulse was 10 ms. From these time delays, a known Poisson's ratio σ=0.30 in the undisturbed formation, and equations (10),

$$\Delta T_s = \Delta x (1/v_s' - 1/v_s) \qquad (12)$$

and

$$v_s'^2/v_p'^2 = (0.5-\sigma)/(1-\sigma) \qquad (13)$$

the Poisson's ratio σ' within the steam invaded zone was found to be as high as 0.40 .

It may appear at first sight that the logic behind this calculation is circular: Equations (10) and (12), from which v_s' is derived, form a system of two equations with three unknowns: v_s', v_p',and Δx. Therefore, one has to start with an assumption for v_p'. For v_p' 20% less than v_p we found σ'=0.40 . For lower values of v_p', σ' increases. For example, for v_p' 30% less than v_p, σ' was 0.42 . Hence, our calculations are weakly dependent on the choice of v_p', and consistently lead to high Poisson's ratios within the zone

of interest. Poisson's ratio is an excellent indicator of the presence or absence of steam within a porous medium. This statement is supported both by theoretical and experimental studies (Domenico,1974). There is good evidence of Poisson's ratios as low as 0.16 in steam-dominated geothermal fields, (Majer and McEvilly,1979). The high Poisson's ratios we have identified in our steam invaded zone indicates that the zone is dominated by steam condensate rather than steam. This in fact is not surprising in view of the relatively small injection period (48 days) and the fact that the seismic measurements were taken during the first cycle of the steam stimulation program.

Finally, we carried out spectral analysis of the 'before' and 'after' S-wave pulses at receiver #2 in order to estimate the S-wave attenuation within the steam zone. We employed the technique we discussed earlier for calculating Q_p'. For the S case, v_p, Q_p, and v_p' in eqn. (11) should be replaced by v_s, Q_s and v_s'. Hence:

$$Q_s' = \pi \Delta x Q_s v_s / \{(a Q_s v_s + \pi \Delta x) v_s'\} \qquad (14)$$

V_s was calculated from the presteam Poisson's ratio to be 1200 m/s and v_s' was found from eqns (10) and (12) to be 800 m/s for v_p'=2,000 m/s.

Q_s could not be determined from our seismic experiments: Direct S-arrivals were not recorded in the presteam tomography experiment and were severely disturbed

by reflections from reflectors below the Clearwater in records #7 to #10 of the 'before' and 'after' experiment. However, we found that the calculation of Q_s' is only weakly dependent on Q_s in (14). For Q_s=60 we found Q_s'=10.4 while for Q_s=30 Q_s' was 9.5 . For v_p'=1,800 m/s we obtained Q_s=8.3 and 7.6 respectively. These values of Q_s' are close to the values we obtained for Q_p'. This may be another indicator of high fluid saturation within the steam zone. Murphy (1983) has provided experimental evidence that Q_p is roughly equal to $0.5Q_s$ for fluid saturations less than 90% (in agreement with the theoretical results of Mavko and Nur (1979)), and that Q_p is approaching Q_s at higher saturations. The spectra of the 'before' and 'after' S pulses at receiver #2, as well as their spectral ratios are shown in Figure 36. Notice the shift of the spectra towards lower frequencies, compared to the spectra of the P-waves of figure 35.

Both, figure 35 and figure 36 show some evidence of a frequency dependence of attenuation in the heated zone . A possible interpretation is that the spectral ratios in these diagrams indicate a system characterized by 2 or 3 attenuation mechanisms -see for example the enveloppes with gashed lines superimposed on the spectral ratios of figure 36.

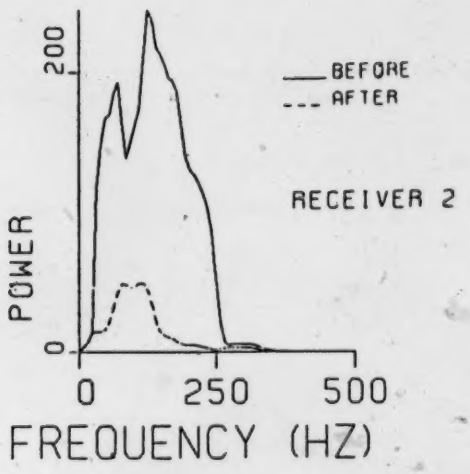

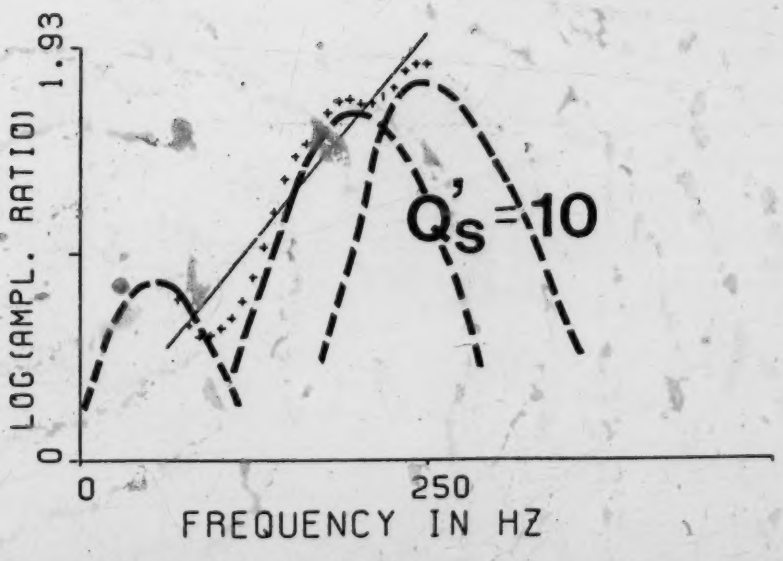

Figure 36.... Before and after power spectra of the S-pulses at receiver #2 and their spectral ratios plotted versus frequency. A possible interpretation indicates a system of 3 attenuation mechanisms.

VI. CONCLUSIONS

Seismic well-to-well tomography appears to be an attractive technique for high resolution imaging of the medium between boreholes. It should be pointed out that this is the first study of its kind in the application of seismic tomography methods to oil sands projects. The first in-situ Q and Poisson's ratios measurements during a thermal recovery process are also presented here. Our particular interest is in accurate delineation of seismically anomalous zones introduced into a formation after it has been subjected to steam stimulation. Before and after steam injection seismic experiments are recommended in order to reduce the dimension of the inversion problem.

Extra care must be exercised when designing the experiments: The spacing of the sources and receivers must be less than five meters to ensure that coverage of the target zone is as dense as possible. The sampling interval must be preferably 0.5 ms or less for accurate detection of small time delays of the seismic pulses after injection. Sources should be developed with a broad bandwidth content (100 to 1000 Hz) and a good reproducibility under borehole conditions.

The seismic data analyzed in this thesis were collected from two experiments: 1) A 'before' and 'after' well-to-well survey which used an small explosive source and 2) a presteam tomography experiment employing an air gun source within the source well and a string of receiving hydrophones

positioned in the receiver well. The two wells were separated by a distance of 180 m. The dynamite source provided excellent signal to noise ratio, poor repeatability, and high frequency content. The air gun source, at pressure of 2,300 PSI, provided excellent repeatability,lower frequency content and lower signal to noise ratios. It was found that at greater depths considerable operational problems can be encountered if the instrument is not adequately sealed. Pressures as high as 3,000 PSI would be highly desirable at such depths to avoid deterioration of signal to noise ratio and reduce the need for repeat shots. This,in turn, could reduce the time and cost of the operation, but it can also put severe demands of miniaturization on the design of the instrument.

The use of dynamite source for tomography studies can provide excellent quality of data on one hand but with no guarantee on the physical integrity of the borehole in view of the large number of shots required in a tomography survey. Futhermore, the time required to conduct the experiment can be ten times greater than with an air gun source.

Strong tube waves were recorded in our experiments and were used for normalizing the presteam with the poststeam seismic data.

Data processing in the form of frequency filtering, redigitization,stacking, and cross-correlation was carried out and provided help for proper identification and

enhancement of the events of interest. Spectral analysis showed significant changes after fluid injection. The results cannot be readily quantified but there is strong evidence of scattering from the steam zone.

Computer simulation of the poststeam geometry was carried out using a simple straight ray path approach and a variety of steam zone shapes. Inversion of the synthetic P-wave delay times was by a solution of an overdetermined system of linear equations. The reconstruction quantity was the differential slowness within the solution space. A direct least squares inversion provided acceptable results but superior reconstructions were obtained by using a fully constrained algebraic reconstruction approach employing the method of projections. This is a very attractive technique for limited angle tomography problems and it allows one to incorporate apriori knowledge and constraints on the solution. The error induced by space discretization can be reduced if an optimum size of pixels is chosen. When the above technique was combined with data interpolation and radial smoothing, improved results were obtained and the reconstruction algorithm was able to successfully reconstruct different regions within the steam zone. The resolving power of the method is intimately linked to the density of coverage, hence to the spacing of sources and receivers. Other parameters that can favorably affect the resolution are high frequency content of the recorded signals, small sampling interval, and as great an angular

coverage as possible, under the existing geological constraints.

Inversion of the presteam tomography data revealed dispersion effects from which the in-situ intrinsic attenuation of the Clearwater Formation was estimated. Independently, attenuation was obtained by employing the spectral ratio method and the concept of average frequency . The obtained values of Q_p were close to 30. By analyzing data from the 'before' and 'after' experiment, considerably lower values of Q_p and Q_s were found within the steam zone. These are attributed to large amounts of viscous dissipation of the seismic energy in the fluids introduced within the pore space as a result of the process of steam stimulation. Normally, one should expect higher Q at higher temperatures. The observed low Q values in the heated zone were explained in terms of the dramatic increase of permeability in the heated zone, due to bitumen mobilization. If this is true it is entirely possible that one could use an accurate mapping of Q for the purposes of making in-situ measurements of permeability during enhanced heavy oil recovery operations.

Finally, by exploiting 'before' and 'after' S-wave arrivals it was possible to obtain the Poisson's ratio within the steam zone. This was found to be as high as 0.40 indicating the presence of large amounts of steam condensate within the zone of interest.

Field measurements were not optimized for determining attenuation or Poisson's ratio, so the results are

significant in establishing that it is possible to obtain such parameters. Optimization of recording techniques will certainly allow one to obtain the spatial variation of these variables. For example, the reconstruction technique suggested for transmission P-arrivals in chapter 2 could be repeated for S-waves. Then from the results of the two reconstructions one can immediately determine the distribution of the Poisson's ratio within the reconstruction space.

BIBLIOGRAPHY

Aki,K.,and Richards,P.G.,1980,Quantitative seismology-Theory and Methods, Freeman Co.

Azimi,S.A.,Kalinin,A.V., Kalinin,V.V.,and Pivorarov,B.L., 1968,Impulse and transient characteristics of media with linear and quadratic absorption laws, Izvestia (Earth Physics)42-54.

Bailey,N.J.L.,Jobson,A.M.,and Rogers,M.A.,1973,Bacterial degradation of crude oil: Comparison of field and experimental data:Chemical Geology,11,202-220.

Bergman,N., 1987, Ph.D. thesis, University of Toronto, Department of Physics.

Carrigy,M.A.,and Kramers,J.W.,1975,Geology of the Alberta Oil Sands:Proceedings of the first regional conference of the western region engineering institute of Canada,p.13-24.

Cheng,C.H. and Toksoz, M.N.,1982, Generation,propagation and analysis of tube waves in a borehole:SPWLA 23rd Annual Logging Symposium, paper P.

Chiu,S.K.L., Kanasewich,E.R. and Phadke,S., 1986, Three dimenional determination of structure and velocity by seismic tomography, Geophysics ,51, 1559-1571.

Coats,K.H., and Ramesh,A.B.,1977,Numerical modeling of

thermal reservoir behavior: The oil sands of Canada-Venezuela,CIM special volume 17, p.399-410.

Daniell,P.J.,1946, Discussion on symposium on autocorrelation in time series: Supplement to the J.Royal Statist. Soc.,8,88-90.

Demaison,G.J.,1977,Tar sands and supergiant Oil Fields: The oil sands of Canada-Venezuela,CIM special volume 17,p.9-17.

Dines,K.A., and Lytle,R.J.,1979, Computerized geophysical tomography: Proceedings of the IEEE, 67, 1065-1073.

Dobrin,M.B.,1976,Introduction to Geophysical Prospecting, chapter 10,McGraw-Hill Book Co.,third edition.

Domenico,S.N.,1974. Effect of water saturation on seismic reflectivity of sand reservoirs encased in shale:Geophysics,39, 759-769.

Dusseault,M.B.,1977,Stress State and Hydraulic fracturing in the Athabasca Oil Sands: The oil sands of Canada-Venezuela,CIM special volume 17,p.27-35.

Dusseault,M.B.,1977,The Geotechnical characteristics of the Athabasca oil sands, Ph.D. thesis, department of Civil Engineering, University of Alberta, Edmonton, Alberta, Canada.

ERCB,Reserve Report Series ERCB-18,Dec. 31/84.

Farouq Ali,S.M.,1974, Current status of steam injection as a heavy oil recovery method: J.Can.Pet.Tech.,120-145.

Farouq Ali,S.M.,1982,Elements of Heavy Oil Recovery, University of Alberta Press.

Fehler,M.,and Pearson C.,1984,Cross-hole seismic surveys:Applications for studying subsurface fracture systems at a hot dry rock geothermal site: Geophysics,49,37-45.

Finbow,R.G., and Koop,I.J.,1977,A sensitivity study of cyclic steam stimulation using a 2-D mathematical model : The oil sands of Canada-Venezuela,CIM special volume 17,p.419-433.

Flock,D.L.,and Lee,J.,1977,An experimental investigation of steam displacement of a medium gravity crude oil: The oil sands of Canada-Venezuela,CIM special volume 17,p.386-394.

Gardner,G.H.F.,Gardner,L.W.,and Gregory,A.R.,1974,Formation velocity and density:the diagnostic Basics for Stratigraphic Traps:Geophysics ,39,770-780.

Futterman,W.I.,1962,Dispersive body waves,J.Geophys.Research, 67,5279-5291.

Gordon,R.,1974, A tutorial on ART (Algebraic Reconstruction techniques): IEEE Trans. Nucl. Sci.,21,78-93.

Greenleaf,J.F. and Johnson,S.A.,1978. Measurement of spatial distribution of refractive index in tissues by ultrasonic computer assisted tomography: Ultrasound Med. & Biol.,3,327-339.

Han,D.,Nur.A. and Morgan,D., 1986, Geophysics,51, 2093-2107.

Hardage,B.A.,1981, An examination of tube wave noise in vertical seismic profile data: Geophysics,46,892-903.

Harris,M.C., and Sobkowicz,J.C.,1977,Engineering behavior of Oil Sand: The oil sands of Canada-Venezuela,CIM special volume 17,p.270-280.

Harrison,D.B.,Glaister,R.P., and Nelson,H.W.,1981, Reservoir description of the Clearwater oil sand,Cold Lake, Alberta,Canada. In: The Future of Heavy Crude and Tar Sands, McGraw-Hill, p.264-279.

Hauge.P.S.,1981,Measurements of attenuation from vertical seismic profiles:Geophysics,46,1548-1558.

Herman,G.,1980,Image reconstruction from projections:New York ,Academic Press.

Ivansson,S.,1986, Seismic borehole tomography-Theory and computational methods: Proceedings of the IEEE,74,328-338.

Jones,T.D.,1986. Pore fluids and frequency-dependent wave propagation,Geophysics,51,1939-1953.

Jones,T.D.,and Nur,A.,1983,Velocity and attenuation in sandstones at elevated temperatures and pressures,Geophys. Research Letters,10,140-143.

Kaczmarz,S.,1937,Angenaeherte auffloesung von systemen linearen gleichungen: Bulletin International de Sciences et de Lettres, Serie A:Sciences Mathematiques,355-357.

Kanasewich,E.R.,1981,Time sequence analysis in geophysics: The University of Alberta Press, (third edition).

Kjartansson,E.,1979,Constant Q-wave propagation and attenuation ,J.Geophys.Research,84,4737-4748.

Lawson,C.L. and Hanson,R.J.,Solving least squares problems: Prentice-Hall Inc.

Lee,M.W.,Balch,A.H.,and Parrot,K.R.,1984,'Radiation from a downhole airgun',Geophysics,49,27-36.

Liu,H.P., Anderson,D.L. and Kanamori,H.,1976, Velocity dispersion due to anelasticity, Geophysical journal of the Royal Astronomical Society,47, 41-58.

Macrides,C.G., Kanasewich,E.R. and Bharatha,S.,1985, Cross-borehole seismic imaging in steam injection projects, paper VV-5 presented at the C.S.E.G. National Convention.

Macrides,C.G., Kanasewich,E.R., and Bharatha,S.,1986, Seismic tomography in steam injection heavy oil recovery

projects, presented at the C.S.E.G. National Convention, paper IMG-3.

Macrides,C.G. and Kanasewich,E.R.,1987, Elastic attenuation and Poisson's ratios in oil sands from seismic tomography, presented at the C.S.E.G. National Convention, paper TOMO-1.

Mandl,G. and Volek,C.W.,1969, Heat and mass transport in steam-drive processes: SPEJ,9,59-79.

Majer,E.L.,and McEvilly, T.V.,1979,Seismological investigations at the Geysers geothermal field:Geophysics,44,246-269.

Margenau,H.,and Murphy,G.M.,1955,The mathematics of Physics and Chemistry,Van Nostrand Company Inc.

Marx,J.W. and Langenheim,R.H.,1959, Reservoir heating by hot fluid injection: Trans. AIME,216,312-315.

Mavko,G.M.,and Nur.A.,1979,Wave attenuation in partially saturated rocks,Geophysics,44,161-178.

McMechan,G.A., 1983, Seismic tomography in boreholes: Geophys. J.R. Ast. Soc.,74,601-612.

Menke,W.,1984,The resolving power of cross-borehole tomography: Geophysical research Letters, v.11,p.105-108.

Murphy,W.,1983, Effects of partial water saturation on

attenuation in Massillon Sandstone and Vycor porous glass,J.Acoust.Soc.Am., 71,1458-1468.

Nicholls,J.H., and Luhning,R.W.,1977,Heavy Oil Sand in-situ Pilot Plants in Alberta: The oil sands of Canada-Venezuela,CIM special volume 17,p.527-538.

Nur A.,Walls J.D.,Winkler K. and De Vilbiss,J.,1980, Effects of fluid saturation on waves in porous rock and relations to hydraulic permeability: SPEJ,20,450-458.

Nyland,E., 1982, Fireflood microseismic monitoring ; results and potential for process control, petroleum society of CIM, paper number 82-33-39, presented at the 33rd annual meeting of the petroleum society of CIM.

Nyland,E., 1985, Seismic attenuation in oil sand, AOSTRA journal of research, 2, 47-51.

O'Connel and Budiansky,1977, Viscoelastic properties of fluid saturated cracked solids:J.Geophysical Research,82,5719-5735.

Outtrim,C.P., and Evans,R.G.,1977,Alberta's Oil sands reserves and their evaluation: The oil sands of Canada-Venezuela,CIM special volume 17,p.36-66.

Palmer, I.D.,and Traviolia,J.L.,1980, Attenuation by squirt flow in undersaturated gas sands:Geophysics, 45,1780-1792.

Putnam,P.E., and Pedskalny,M.A.,1983, Provenance of Clearwater Formation Reservoir Sandstones, Bulletin of Canadian Petroleum Geology,31,148-160.

Rangayyan, R.M,1984, Computed tomography techniques and algorithms:a tutorial presented in international conference on computers and signal processing, Bangalore, India, December 10-12.

Rosenfeld,A. and Kak,A.,C.,1982, Digital picture processing :Academic Press,inc.,(2nd Edition).

Schoenberger,M. and Levin,F.K.,1974, Apparent attenuation due to intrabed multiples, Geophysics,43,730-737.

Shepp,L.A., and Logan,B.F.,1974,The Fourier reconstruction of a head section,Trans. Nucl. Sci.,21,21-43.

Sheriff,R.E.,1973,Encyclopedic dictionary of exploration geophysics:SEG,Tulsa.

Sommerfeld, A., 1964, Optics: Academic Press Inc.

Stanley,W.D.,Dougherty,G.R.,and Dougherty,R.,1984,Digital signal processing,REston Publishing Company.

Stewart,R.R., Huddleston,P.D., and Kan,T.K., 1984, Seismic versus sonic velocities: A vertical seismic profiling study, Geophysics, 49,1153-1168.

Tanabe,K.,1971, Projection method for solving a singular system of linear equations : Numer. Math.,17,203-214.

Thomsen,L., Weak elastic anisotropy, Geophysics,51,1954-1966.

Tosaya,C.A., Nur,A.M., and Da Prat,G.,1984, Monitoring of Thermal EOR Fronts by seismic methods:SPE 12744,179-186.

Treitel,S. and Robinson,E.A.,1966,Seismic wave propagation in layered media in terms of communication theory:Geophysics ,31,17-32.

Widess,M.B.,1973, How thin is a thin bed?, Geophysics,38, 1176-1180.

Winkler,K.W., and Nur,A.,1982,Seismic attenuation effects of pore fluids and frictional sliding :Geophysics,47,1-15.

Wong,J.,Bregman,N.,West,G. and Hurley,P., 1987, Cross-hole seismic scanning and tomography, Geophysics: the leading edge of exploration , January 1987.

APPENDIX

Introduction

Marx and Langenheim in 1959, and Mandl and Volek in 1969 developed the first successful mathematical models for steam injection. In spite of obvious limitations of the models (lack of multiphase flow for example) and the recent development of more sophisticated models (discussion of which is beyond the scope of this thesis) these are still of great value for preliminary calculations of steam or hot water injection. Therefore, we find it appppropriate to discuss the models here and to carry out calculations of steam zone volume under the conditions of the steam injection experiment of chapter 2. The obtained results are of interest for the purposes of a computer simulation of the after injection seismic tomography experiment.

The Marx-Langenheim model

When steam at temperature T_s (saturation temperature corresponding to the prevailing pressure P_s) is injected into the oil-bearing formation at temperature T_R, it mobilizes and displaces a certain fraction of the in-place oil while condensing and heating the rock and the fluids simultaneously. The condensate formed, still at temperature T_s, moves ahead of the freshly injected steam preheating the rock further ahead. Under idealized conditions (i.e. no

gravity segregation of steam, uniform formation thickness, injection over entire thickness, and no pressure drop -i.e. temperature drop- in the steam invaded zone) it could be postulated that the heated zone is at a constant temperature T_s, extending from the injection well to the point where the temperature abruptly drops from T_s to T_R. Marx and Langenheim (1959) first postulated such a picture for steam injection.

The heated zone, hereinafter called the 'steam zone', encompasses the volume of the rock and fluids heated to steam temperature T_s, regardless of the steam quality. The Marx-Langenheim treatment implies that the condensate tranfers the sensible heat over an infinitesimal distance which constitutes the so-called condensation front. The result is a step function temperature profile in which T_s drops to T_R. Under the assumptions described above, a heat balance at any time t gives:

Heat injection rate (Q_i)=Heat loss rate to overburden and underburden+Heating rate of the rock and the fluids to T_s.

or $$Q_i=Q_{ob}+Q_s \qquad (1)$$

This heat balance equation results in a differential equation the solution of which gives the steam zone volume V_s:

$$V_s=Q_i M_s h_t^2 F_1 / 4K_{hob} M_{ob} (T_s-T_R) \qquad (2)$$

We would like to calculate V_s under the conditions of the

steam injection experiment discussed in chapter 2. The heat injection rate Q_i is given in BTU/hour by:

$$Q_i=(350/24)i_{st}\{(h_v-h_R)+f_{st}L_v\} \qquad (3)$$

where i_{st} is the steam injection rate in B/D (water equivalent). This rate was 1,320 B/D in the experiment. The bottomhole steam quality f_{st} is typically about 70%. Steam was injected at a pressure of 10 MPa(=1,450 PSI). From steam tables we find that the corresponding temperature is $590^0F(=310^0C)$; h_v,h_R and L_v are enthalpies of saturated water,water at reservoir temperature and vaporization (latent heat). From these values, we calculated Q_i to be equal to 18,747,368 BTU/hour. The volumetric heat capacity M_s of the Clearwater Formation is 2,500 KJ/m^3-^0K (=37.3 BTU/ft^3-^0F). The thickness of the Clearwater at the location of the experiment was 50 m (=164 feet). The thermal conductivity K_{hob} of the overburden is $2.1W/m-^0K$ (=1.21 $BTU/hr-ft-^0F$) and the heat capacity of the overburden M_{ob}=2650 KJ/m^3-^0K (=39.5 BTU/ft^3-^0F). Reservoir temperature is $12^0C(=53.6^0F)$. F_1 is the so-called Marx-Langenheim function given by

$$F_1=\exp(t_D)\mathrm{erfc}(t_D)^{1/2}+2(t_D/\pi)^{1/2}-1 \qquad (4)$$

where erfc denotes the complementary error function (1-erf) and the dimensionless time t_D is proportional to the

injection time t :

$$t_D = 4K_{hob} M_{ob} t / M_s^2 h_t^2 \qquad (5)$$

Injection time was 48 days in the experiment. Substituting the above parameters in (5) we find t_D=0.00587. From tabular values of (4) we find F_1=0.00567. Then, substituting in (2) we find V_s=1,026,244 ft^3. This gives radius **R=13.6m** for the cylindrically shaped steam zone.

The Mandl-Volek model

The principal shortcoming of the Marx-Langenheim model, aside from neglecting gravity effects, is that the steam injected must supply the latent heat contained in the newly invaded formation as well as satisfy heat loss to adjacent formations. So long as the latent heat injection rate is greater than the rate of its consumption in this manner, the Marx-Langenheim model holds, (Farouq Ali,1982). However at a certain time, which Mandl and Volek call the critical time, this ceases to be so, and allowance must be made for convective heat transport by hot water ahead of the condensation front. The result is a gradual (instead of a step-like) drop of temperature within the condensation front. Mandl and Volek (1969) first recognized this situation and obtained the following set of equations which can be used in order to calculate the critical time t_c.

$$t_c = M_s^2 h_t^2 t_{DC} / 4K_{hob} M_{ob} \qquad (6)$$

The dimensionless time t_{DC} is found from tabular values of:

$$\exp(t_{DC}) \operatorname{erfc}(t_{DC})^{1/2} = (1+B)^{-1} \qquad (7)$$

$$\text{where } B = f_{st} L_v / (h_v - h_R) \qquad (8).$$

Substitution in (6),(7) and (8) of the known parameters gives : B=0.65, t_{DC}=0.27 and critical time t_c =6 years. It is of interest to calculate the steam zone volume for this time. Substitution in (5),(4) and (2) gives the radius of the heated zone equal to R=80 m. Notice that this is very close to the distance between the injection well and the seismic source and seismic receiver wells of our experiment . Hence we conclude that steam breakthrough might occur at these wells after an injection time of six years.

So long as the time is equal or less than the critical time, the Marx-Langenheim solution remains valid. For greater times the Mandl-Volek solution must be used. The equation giving V_s is identical to (2) with the exception that F_1 is replaced by F_3, the Mandl-Volek function. This is a rather complicated function of t_{DC}, t_D, and B. Notice (from equation 6) that the thicker the formation the longer the critical time . At times less than the critical time, the Mandl-Volek solution is identical to the Marx-Langenheim solution as F_3 becomes equal to F_1.

DEEP SONIC LOGS FROM THE COLD LAKE AREA, CENTRAL ALBERTA.

Well marked with an asterisk ('Imp May Lake') was the closest one to the location of the seismic experiments described in the thesis.

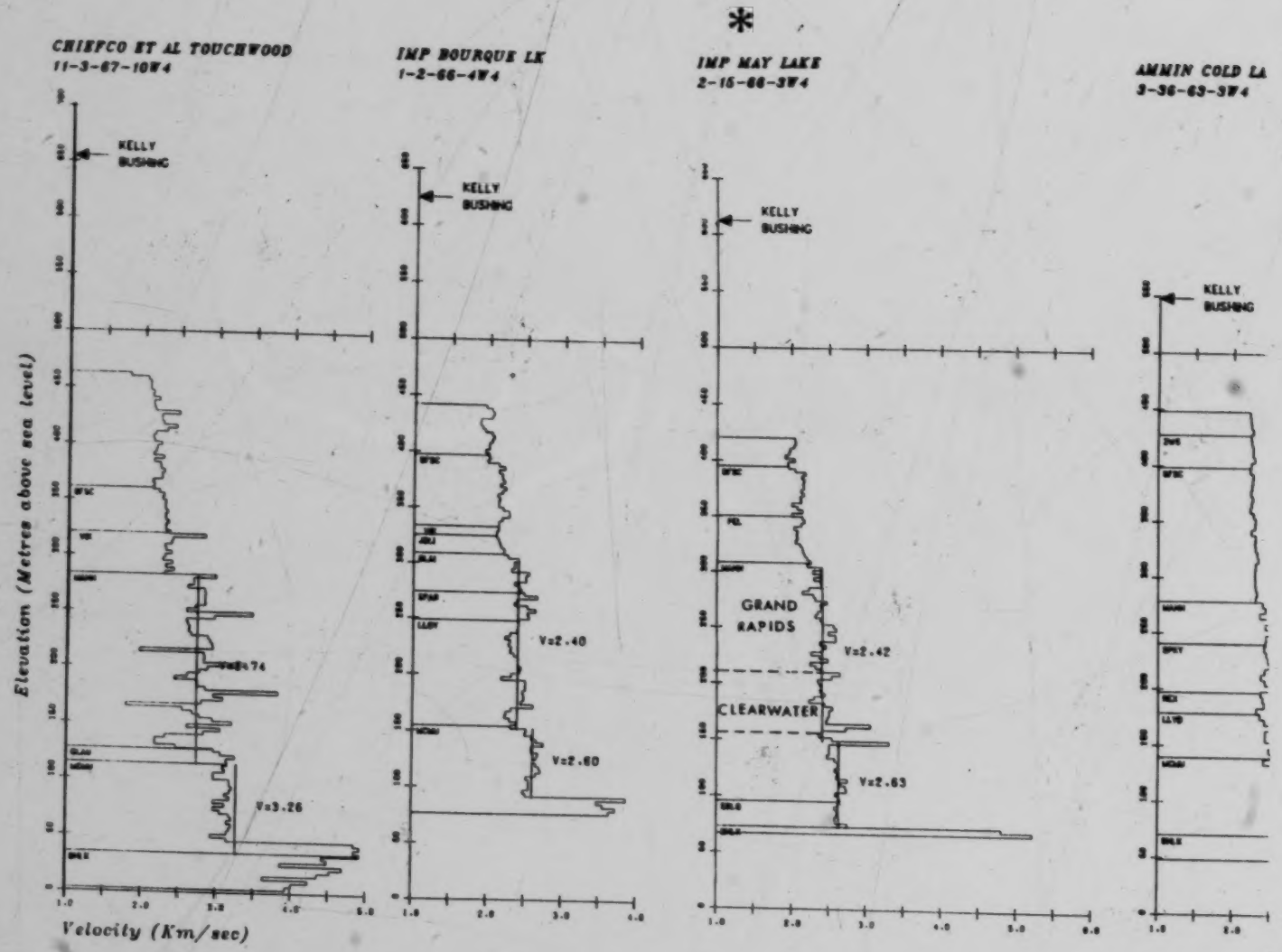
CHIEFCO ET AL TOUCHWOOD
11-3-87-10W4
IMP BOURQUE LK
1-2-66-4W4
IMP MAY LAKE
2-15-66-3W4
AMMIN COLD LA
3-36-63-3W4
KELLY BUSHING
KELLY BUSHING
KELLY BUSHING
KELLY BUSHING
GRAND RAPIDS
CLEARWATER
Vo3.26
Vo2.40
Vo2.60
Vo2.42
Vo2.63
Elevation (Metres above sea level)
Velocity (Km/sec)

GRT. PLNS. ET AL COLD
8-1-64-3W4

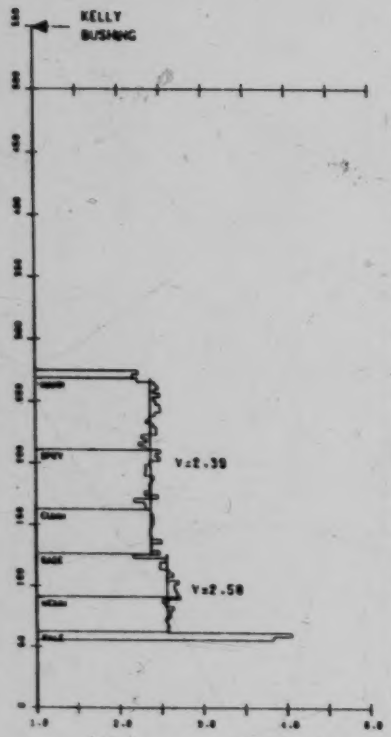

IMP BOURQUE
4-35-63-3W4

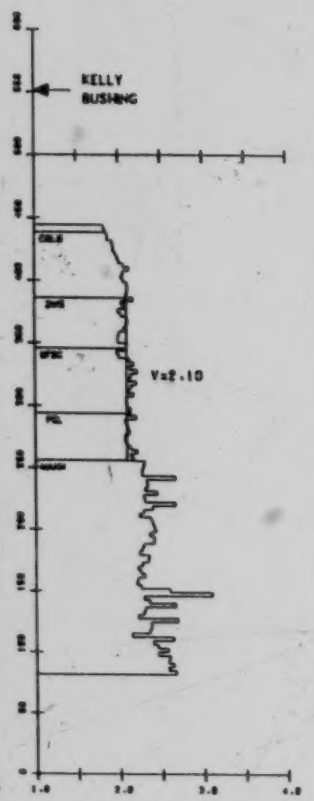

IMP MARIE LAKE
5-32-65-2W4

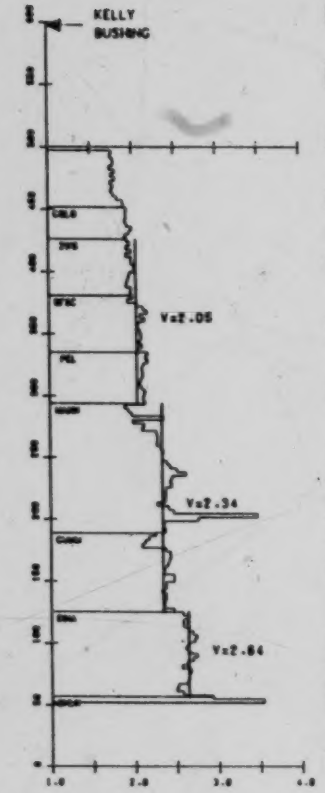

IMP 74 LEMING
6-9-65-3W4

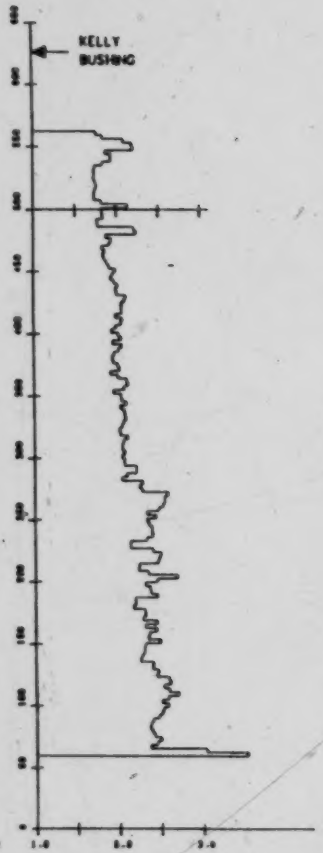

Sonic logs for the source well (OB-1) and receiver well (OB-4) of the tomography experiment of Figure 23 in Chapter 3.

Kelly Bushing elevation of OB-1 well was 626.2 m.

Kelly Bushing elevation of OB-4 well was 630.1 m.

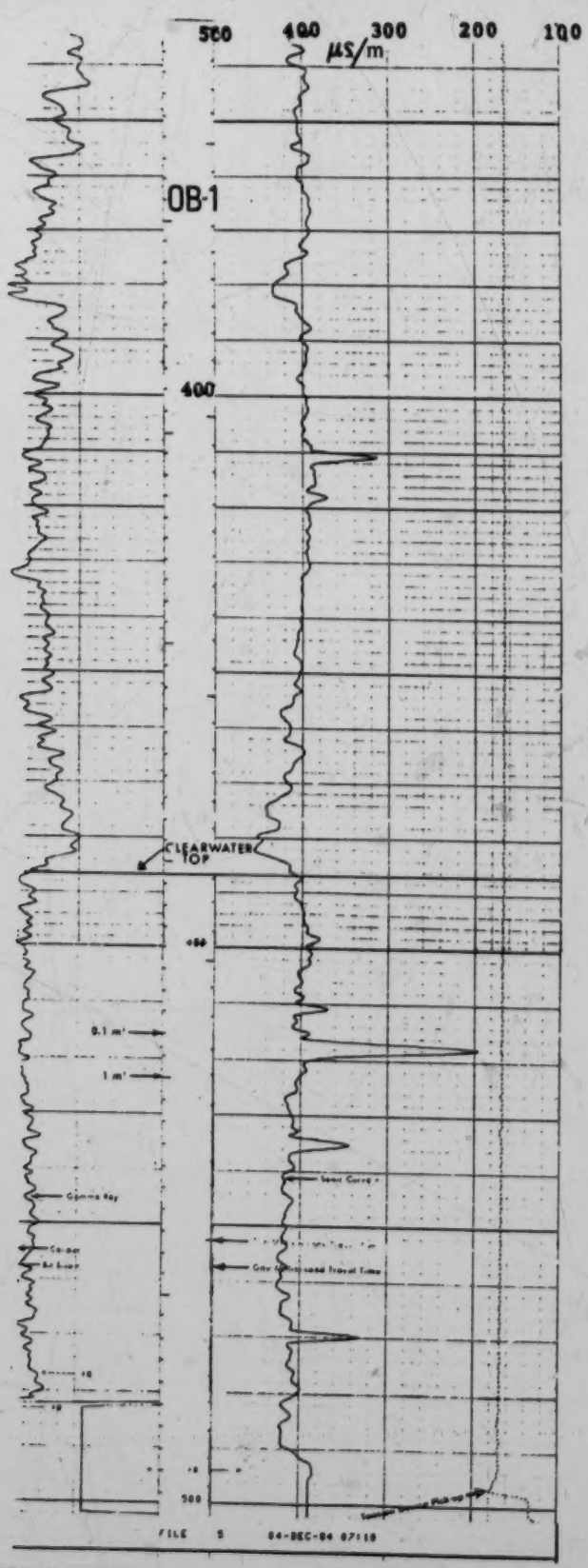
500
400
300
200
100
µS/m
OB-1
400
CLEARWATER
TOP
0.1 m'
1 m'
FILE 5 04-DEC-84 07:18

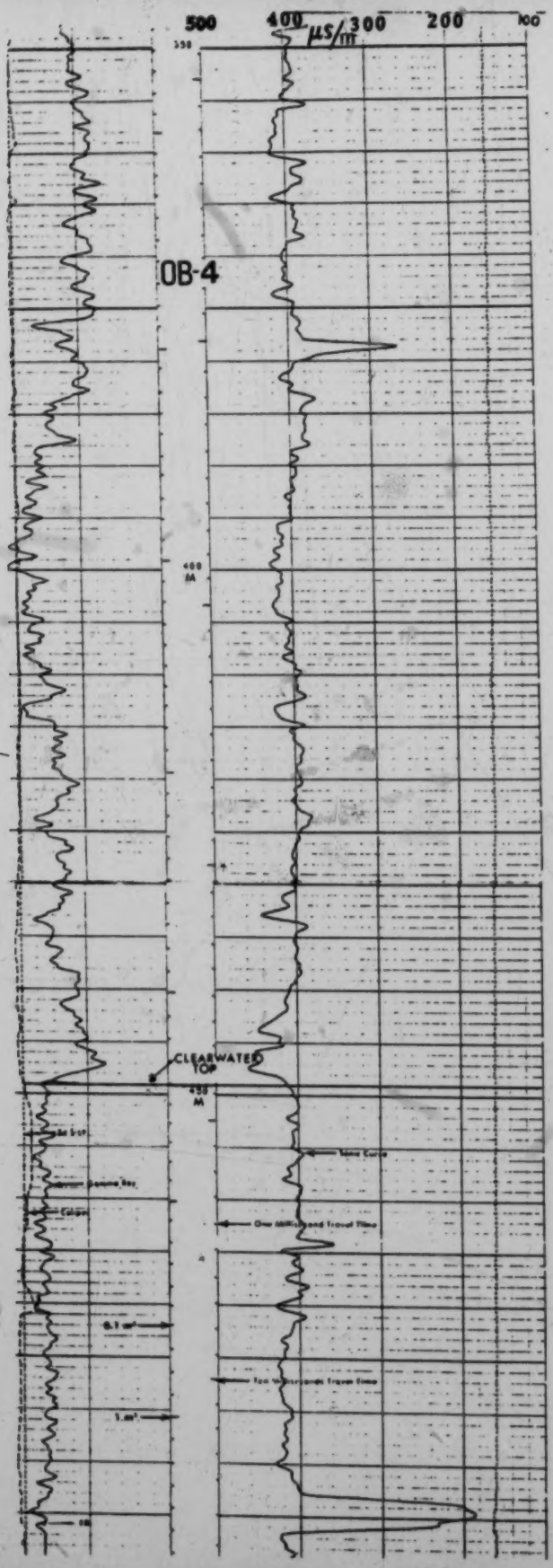
500
400
μs/m
300
200
100
OB-4
CLEARWATER TOP

```
C  This program inverts synthetic delay times
C  of a before and after experiment with geometry
C  identical to the geometry of the field tomography
C  experiment of May 29, 1985 in Cold Lake. The phantom
C  for the forward calculations consists of two ellipses.
C  The pixel size of the superimposed grid was 4 meters.
C  In order to define the reconstruction space and label
C  the pixels, program ELIPS must be run.
C  Program ELIPS produces a ray plot which shows
C  redundancy of penetrating and nonpenetrating rays.
C  Each ray penetrating the target provides a useful
C  equation for the inversion .
C
      DIMENSION AOR(586,171)
      DIMENSION SDEPTH(24),RDEPTH(24)
      REAL BDT(305),VELOC(171)
      DIMENSION AL(171),BL(171),ALFA(305),BETA(305)
      DIMENSION FINIT(171),F(10,171),V(171),FE(171)
      DIMENSION POS(24),TIME(24),C(23,3),BPAR(4)
      DIMENSION U(48),S(48),DTIME(586)
      DIMENSION ALF(586),BET(586)
C     ..... Pixel size 4m .....
      NX=45
      NY=20
      IPLOT=1
      SEARCH=0.0
      SMOOTH=1.0
      NELIPS=2
      VP=2.40
      INVERT=1
      ITER=10
      HSHIFT=0.0
      VSHIFT=0.0
C      Upper and lower bounds of the solution
      FMAX=0.16
      FMIN=0.013
      VMAX=2.4/(1+FMIN*2.4)
      VELMIN=2.4/(1+FMAX*2.4)
C   Reconstruction space consists of N pixels.
C   There are M rays penetrating the anomalous zone.
      N=171
C  M after interpolation
      M=586
      IA=M
C  DX   : The grid spacing in meters.
C  NPIX : Must be equal to N = number of columns in matrix A.
C  M    : The number of rows in the matrix
C  A    : Number of rays penetrating the target.
C  When positioning the grid make sure that a horizontal
C  Ray is not exactly at the horizontal boundary of a pixel.
C
C  DX and WSEP in meters
C
      DX=4.0
      NPIX=N
      WSEP=180.00
```

```
C  FX and FY are the coordinates on meters of the lower left
C  corner of the grid with respect to the origin coordinates.
      FX=0.0
      FY=-2.5
C  READ THE DEPTHS OF THE SOURCES AND RECEIVERS IN
C  TRUE DEPTHS IN METERS START FROM THE TOP.
      READ(5,133)SDEPTH
      READ(5,133)RDEPTH
 133  FORMAT(24F10.0)
C  Correct the depths of receivers to align Kelly Bushing
C  of the receiver well with that of source well OB-1
      DO 233 IT=1,24
      RDEPTH(IT)=RDEPTH(IT)-4.0
 233  CONTINUE
C
C  Define the coordinates of the lower left end of
C  each unknown pixel in the reconstruction space.
C  The origin of the coordinate system is receiver #24.
C  i.e. The deepest receiver in the receiver well.
C  FQX and FQY are the coordinates of the first pixel
C  in the reconstruction space.
      FQX=13.
      FQY=10.
      DO 39 K=1,9
      AL(K)=FQX
      BL(K)=FQY
      FQX=FQX+1.
  39  CONTINUE
      FQX=11.
      FQY=9.
      DO 40 K=10,22
      AL(K)=FQX
      BL(K)=FQY
      FQX=FQX+1.
  40  CONTINUE
      FQX=8.
      FQY=8.
      DO 41 K=23,42
      AL(K)=FQX
      BL(K)=FQY
      FQX=FQX+1.
  41  CONTINUE
      FQX=6.
      FQY=7.
      DO 42 K=43,67
      AL(K)=FQX
      BL(K)=FQY
      FQX=FQX+1.
  42  CONTINUE
      FQX=4.
      FQY=6.
      DO 43 K=68,96
      AL(K)=FQX
      BL(K)=FQY
      FQX=FQX+1.
  43  CONTINUE
```

```
      FQX=4.
      FQY=5.
      DO 44 K=97,127
      AL(K)=FQX
      BL(K)=FQY
      FQX=FQX+1.
 44   CONTINUE
      FQX=4.
      FQY=4.
      DO 45 K=128,152
      AL(K)=FQX
      BL(K)=FQY
      FQX=FQX+1.
 45   CONTINUE
      FQX=4.
      FQY=3.
      DO 46 K=153,171
      AL(K)=FQX
      BL(K)=FQY
      FQX=FQX+1.
 46   CONTINUE
C  Reconstruction space has now been defined
 8    FORMAT(1X,83F3.0)
      DO 120 J=1,NPIX
      AL(J)=AL(J)*DX+FX+HSHIFT
      BL(J)=BL(J)*DX+FY+VSHIFT
 120  CONTINUE
C  Initialize the matrix of coefficients
      DO 199 I=1,M
      DO 92 J=1,N
      AOR(I,J)=0.0
 92   CONTINUE
 199  CONTINUE
      DO 139 IKL=1,M
      DTIME(IKL)=0.00
 139  CONTINUE
C  Zero vector is the initial guess of the solution.
      DO 777 IJ=1,NPIX
      FINIT(IJ)=0.0
 777  CONTINUE
C
C        ****** FORWARD MODELLING ********
C  Define the rays and compute their delay times
C  (Synthetic data)by determining the intersection of
C  the straight ray path with the two (or one) ellipses
C  The model is a pair of ellipses.
C  Ellipse 1 - the outside one i.e. the condensate zone
C  Ellipse 2 - inside ellipse i.e. vapour dominated zone
C  VP1 is the background  reservoir velocity
C  VP2 is the velocity in the condensate zone
C  VP3 is the velocity in the steam zone.....
C  if NELIPS=1 then only the inside ellipse (ellipse 2) is
C  considered i.e. only the steam zone without any
C  condensation zone.....hence the outside ellipse is made
C  equal to the inside ellipse and VP2 is made equal to VP3
C  ************************************************************
```

```
      VP1=VP
      VP2=2.10
      VP3=1.80
      IF(NELIPS.EQ.1)VP2=VP3
C             Ellipse 1.(outside)
      X01=70.
      Y01=25.
      A1=30.
      B1=15.5
C             Ellpise 2. (inside)
      X02=70.
      Y02=25.
      A2=20.
      B2=10.
      IF(NELIPS.EQ.1)X01=X02
      IF(NELIPS.EQ.1)Y01=Y02
      IF(NELIPS.EQ.1)A1=A2
      IF(NELIPS.EQ.1)B1=B2
      LX=1
      INDEX=0
      DO 191 ISOU=1,24
      IL1=0
      DO 1191 JJ=1,24
      POS(JJ)=0.0
      TIME(JJ)=0.0
 1191 CONTINUE
      DO 1192 JT=1,48
 1192 U(JT)=0.0
C  BDT(LX) is the travel time of the LX ray.
C  Notice that since distances are in meters and velocities
C  are given in km/s ,BDT will be in msec.
C  ALFA is the slope of the ray and BETA its intercept with
C  respect to the origin.......
      DO 192 IRECVR=1,24
      ALFA(LX)=(RDEPTH(IRECVR)-SDEPTH(ISOU))/WSEP
      BETA(LX)=ABS(RDEPTH(IRECVR)-RDEPTH(24))
      AQ1=B1**2+(ALFA(LX)**2)*(A1**2)
      BQ1=2*ALFA(LX)*BETA(LX)*(A1**2)-2*X01*(B1**2)
     @-2*ALFA(LX)*Y01*(A1**2)
      CQ1=(B1**2)*(X01**2)+(A1**2)*(BETA(LX)**2)
     @+(A1**2)*(Y01**2)-2*BETA(LX)*Y01*(A1**2)
     @-(A1**2)*(B1**2)
      DELTA1=(BQ1**2)-4*AQ1*CQ1
      IF(DELTA1.LT.0.0)GO TO 192
      IL1=IL1+1
      POS(IL1)=FLOAT(IRECVR)
C  IF DELTA1.LT.0.0 then the ray Y=ALFA*X+BETA
C  does not intercept the outside ellipse
C  otherwise it does at the points (X1,Y1) (X2,Y2)
C  notice that X1 > X2.
      X1=(-BQ1+SQRT(DELTA1))/(2*AQ1)
      Y1=ALFA(LX)*X1+BETA(LX)
      X2=(-BQ1-SQRT(DELTA1))/(2*AQ1)
      Y2=ALFA(LX)*X2+BETA(LX)
      IF(NELIPS.EQ.1)BDT(LX)=SQRT((X1-X2)**2+(Y1-Y2)**2)
     @*((1/VP2)-(1/VP1))
```

```
      IF(NELIPS.EQ.1)WRITE(6,245)LX,BDT(LX),ISOU ,IRECVR
      IF(NELIPS.EQ.1)GO TO 30
      AQ2=B2**2+(ALFA(LX)**2)*(A2**2)
      BQ2=2*ALFA(LX)*BETA(LX)*(A2**2)-2*X02*(B2**2)
     @-2*ALFA(LX)*Y02*(A2**2)
      CQ2=(B2**2)*(X02**2)+(A2**2)*(BETA(LX)**2)
     @   +(A2**2)*(Y02**2)-2*BETA(LX)*Y02*(A2**2)
     @   -(A2**2)*(B2**2)
      DELTA2=(BQ2**2)-4*AQ2*CQ2
      IF(DELTA2.LT.0.0)BDT(LX)=SQRT((X1-X2)**2+(Y1-Y2)**2)
     @*((1/VP2)-(1/VP1))
      IF(DELTA2.LT.0.0)TIME(IL1)=BDT(LX)
      IF(DELTA2.LT.0.0)WRITE(6,245)LX,BDT(LX),ISOU,IRECVR
      IF(DELTA2.LT.0.0)GO TO 30
      XX1=(-BQ2+SQRT(DELTA2))/(2*AQ2)
      YY1=ALFA(LX)*XX1+BETA(LX)
      XX2=(-BQ2-SQRT(DELTA2))/(2*AQ2)
      YY2=ALFA(LX)*XX2+BETA(LX)
      DIST1=SQRT((X1-XX1)**2+(Y1-YY1)**2)
      DIST2=SQRT((XX1-XX2)**2+(YY1-YY2)**2)
      DIST3=SQRT((X2-XX2)**2+(Y2-YY2)**2)
      BDT(LX)=DIST1*((1/VP2)-(1/VP1))
     @+DIST2*((1/VP3)-(1/VP1))+DIST3*((1/VP2)-(1/VP1))
      TIME(IL1)=BDT(LX)
      WRITE(6,572)LX,DIST1,DIST2,DIST3,BDT(LX),ISOU,IRECVR
   30 CONTINUE
      LX=LX+1
  192 CONTINUE
  245 FORMAT('LX=',I3,' DEL TIME=',F4.1, 'SOURCE',I3,
     @' RECVR=',I3)
  572 FORMAT('LX=',I3,' DIST1=',F4.1,' DIST2=',F4.1,' DIST3
     @=',F4.1,'DEL. TIME=',F4.1,' SOURCE=',I3,' RECVR=',I3)
C                      Now interpolate
      LAST=IL1
      NSPLN=LAST
      IC=NSPLN-1
      MSPLN=2*NSPLN-1
      BPAR(1)=0.0
      BPAR(2)=0.0
      BPAR(3)=0.0
      BPAR(4)=0.0
      U(1)=POS(1)
      DO 10 ISPLN=2,MSPLN
      U(ISPLN)=U(ISPLN-1)+0.5
   10 CONTINUE
      DO 2651 IX=1,MSPLN
      WRITE(6,65)IX,U(IX)
 2651 CONTINUE
   65 FORMAT('U',I4,F6.1)
      CALL ICSICU(POS,TIME,NSPLN,BPAR,C,IC,IER)
      CALL ICSEVU(POS,TIME,NSPLN,C,IC,U,S,MSPLN,IER)
      I1=IFIX(POS(1))
      WRITE(6,1380)I1
 1380 FORMAT('I1=IFIX(POS(1))=',I4)
      DEEP=RDEPTH(I1)
      DO 5 K=1,MSPLN
```

```
      INDEX=INDEX+1
      ALF(INDEX)=(DEEP-SDEPTH(ISOU))/WSEP
      BET(INDEX)=ABS(DEEP-RDEPTH(24))
      DTIME(INDEX)=S(K)
      DEEP=DEEP+(3.05/2.)
    5 CONTINUE
  191 CONTINUE
      LXX=LX-1
      WRITE(6,490)LXX
  490 FORMAT('TOTAL NUMBER OF RAYS BEFORE INTERPOLATION',I5)
      WRITE(6,1490)INDEX
 1490 FORMAT('TOTAL NUMBER OF RAYS AFTER INTERPOLATION',I5)
      WRITE(6,1600)
 1600 FORMAT('INTERPOLATED DATA SET')
      DO 5100 IB=1,INDEX
      WRITE(6,2120)IB,DTIME(IB),ALF(IB),BET(IB)
 5100 CONTINUE
 2120 FORMAT(I4,3F9.1)
C  Determine the intersection of each ray with the pixels of
C  the grid. the equation of each ray is
C                    Y(L)=ALFA(L)*X+BETA(L)
C                    where L=1,2,3,...M.
      L=1
      DO 100 IROW=1,M
      DO 1 I=1,NPIX
      X1=AL(I)
      Y1=ALF(L)*AL(I)+BET(L)
      IF(ALF(L).LT.0.)GO TO 200
      IF(ALF(L).EQ.0.)GO TO 55
C               Case of positive ALF(L)
C  Notice that if BET(1) is at the level of the pixel
C  i.e. not below the pixel, then THETE and Z will be
C  negative and the parameter F2 will be incorrect unless
C  one takes the absolute value for Z. The same is true
C  later in the case of negative ALF and the parameter F4.
      F1=BL(I)+DX
      F3=AL(I)+DX
      IF(Y1.GE.F1)GO TO 1
C  XTEST1 is the intersection of the ray with the bottom
C  horizontal side of the pixel...
      XTEST1=(BL(I)-BET(L))/ALF(L)
      IF(XTEST1.LT.F3.AND.XTEST1.GE.AL(I))GO TO 3
      IF(XTEST1.GE.F3)GO TO 1
      X2=(BL(I)+DX-BET(L))/ALF(L)
      IF(X2.GT.F3)GO TO 32
      Y2=BL(I)+DX
      AOR(L,I)=SQRT((X2-X1)**2+(Y2-Y1)**2)
      GO TO 1
C                     Case of ALF=0. (The ray is horizontal)
   55 CONTINUE
      IF(Y1.LE.BL(I))GO TO 1
      IF(Y1.GE.(BL(I)+DX))GO TO 1
      Y2=Y1
      X2=AL(I)+DX
      AOR(L,I)=DX
      GO TO 1
```

```
  32  CONTINUE
C                       CASE 1A.
C     Ray exits from the right vertical side of pixel.
       X2=AL(I)+DX
       Y2=ALF(L)*(AL(I)+DX)+BET(L)
       AOR(L,I)=SQRT((X2-X1)**2+(Y2-Y1)**2)
       GO TO 1
   3  CONTINUE
C                       CASE 2.
C     Ray intersects the pixel from below.
       IF(ALF(L).EQ.0.)GO TO 1
       YCRIT=ALF(L)*(AL(I)+DX)+BET(L)
       IF(YCRIT.LE.BL(I))GO TO 1
       Y1=BL(I)
       X1=(BL(I)-BET(L))/ALF(L)
       X2=AL(I)+DX
       Y2=ALF(L)*(AL(I)+DX)+BET(L)
       AOR(L,I)=SQRT((X2-X1)**2+(Y2-Y1)**2)
       GO TO 1
 200  CONTINUE
C                       Case of negative ALF
C  XTEST is the intersection of the ray with the top
C  horizontal side of the pixel.
       IF(Y1.LE.BL(I))GO TO 1
       XTEST=(BL(I)+DX-BET(L))/ALF(L)
       F5=BL(I)+DX
       F6=AL(I)+DX
       IF(XTEST.LT.F6.AND.XTEST.GE.AL(I))GO TO 333
       IF(XTEST.GE.F6)GO TO 1
       X2=(BL(I)-BET(L))/ALF(L)
       IF(X2.GT.F6)GO TO 33
       Y2=BL(I)
       AOR(L,I)=SQRT((X2-X1)**2+(Y2-Y1)**2)
       GO TO 1
   33  CONTINUE
       X2=AL(I)+DX
       Y2=ALF(L)*(AL(I)+DX)+BET(L)
       AOR(L,I)=SQRT((X2-X1)**2+(Y2-Y1)**2)
       GO TO 1
  333  CONTINUE
C                       Case 4.
C      Ray is intersecting pixel from above.......
       Y1=BL(I)+DX
       X1=(BL(I)+DX-BET(L))/ALF(L)
       X2=AL(I)+DX
       Y2=ALF(L)*(AL(I)+DX)+BET(L)
       AOR(L,I)=SQRT((X2-X1)**2+(Y2-Y1)**2)
    1  CONTINUE
       L=L+1
  100  CONTINUE
       IF(INVERT.EQ.0)GO TO 660
C  Investigate if there are identical rows in the matrix
       IF(SEARCH.EQ.0.0)GO TO 1700
       DO 111 IJ=1,M
       DO 112 IRJ=1,M
       IF(IRJ.EQ.IJ) GO TO 112
```

```
      SUM=0.0
      DO 113 IRR=1,N
      SUM=SUM+ABS(AOR(IRJ,IRR)-AOR(IJ,IRR))
  113 CONTINUE
      IF(SUM.EQ.0.00)WRITE(6,229)IJ,IRJ
  112 CONTINUE
  111 CONTINUE
  229 FORMAT('THERE ARE IDENTICAL ROWS IN THE MATRIX: ROWS',
     @I4,' AND',I4)
C  Investigate if there are identical columns in the matrix
      DO 121 IJX=1,N
      DO 122 IRJX=1,N
      IF(IRJX.EQ.IJX) GO TO 122
      SSUM=0.0
      DO 123 IRRX=1,M
      SSUM=SSUM+ABS(AOR(IRRX,IRJX)-AOR(IRRX,IJX))
  123 CONTINUE
      IF(SSUM.EQ.0.0)WRITE(6,28)IJX,IRJX
  122 CONTINUE
  121 CONTINUE
   28 FORMAT('THERE ARE IDENTICAL COLUMNS IN THE MATRIX WL.
     &',I4,'AND',I4)
 1700 CONTINUE
      WRITE(6,171)FMIN,FMAX
  171 FORMAT(//,6X,F6.3,'< F <',F6.3,//)
      WRITE(6,172)VELMIN,VMAX
  172 FORMAT(6X,F6.3,'< P-VEL <',F6.3,//)
C  Exact implementation of Kaczmarz method of projections
      DO 201 K=1,ITER
      SUM1=0.0
      DO 2 IZ=1,N
      SUM1=SUM1+AOR(1,IZ)*FINIT(IZ)
    2 CONTINUE
      SUM2=0.0
      DO 161 IA=1,N
      SUM2=SUM2+AOR(1,IA)**2
  161 CONTINUE
      DO 399 IX=1,N
      F(K,IX)=FINIT(IX)-(SUM1-DTIME(1))*AOR(1,IX)/SUM2
C
C .....Impose bounds on the solution (first projection)..
C  in the differential slowness problem, if F is very small
C  i.e. smaller than FMIN,
C  It means that practically VPJ' = VP so that
C  FJ can be set equal to zero...
C  in the slowness problem the situation is somewhat
C  different because if F < FMIN it must be set equal
C  to FMIN - not equal to zero...
      IF(F(K,IX).LT.FMIN)F(K,IX)=0.0
      IF(F(K,IX).GT.FMAX)F(K,IX)=FMAX
  399 CONTINUE
      DO 101 J=2,M
      SUM1=0.0
      DO 11 JP=1,N
      SUM1=SUM1+AOR(J,JP)*F(K,JP)
   11 CONTINUE
```

```
      SUM2=0.0
      DO 12 JQ=1,N
      SUM2=SUM2+AOR(J,JQ)**2
   12 CONTINUE
      DO 13 ID=1,N
      F(K,ID)=F(K,ID)-(SUM1-DTIME(J))*AOR(J,ID)/SUM2
C             Impose bounds
      IF(F(K,ID).LT.FMIN)F(K,ID)=0.0
      IF(F(K,ID).GT.FMAX)F(K,ID)=FMAX
   13 CONTINUE
  101 CONTINUE
      IF(K.LT.ITER)GO TO 560
      WRITE(6,266)K,HSHIFT,VSHIFT
  266 FORMAT('PIXEL, SOLUTION F, VELOCITY, ITERATION',I5,
     &' HSHIFT=',F5.0,' VSHIFT=',F5.0,/)
      DO 559 IE=1,N
      VELOC(IE)=2.4/(1+(F(K,IE)*2.4))
      WRITE(6,391)IE,F(K,IE),VELOC(IE)
  559 CONTINUE
  560 CONTINUE
  391 FORMAT(I4,F9.3,F9.2)
C   Calculation of residuals and Euclidean distance
      WRITE(6,119)
  119 FORMAT(//,'RAY # , RESIDUAL T IN MSEC')
      SUMRES=0.0
      DO 1001 L=1,M
      SUMX=0.0
      DO 1002 J=1,N
      SUMX=SUMX+AOR(L,J)*F(K,J)
 1002 CONTINUE
      RESID=DTIME(L)-SUMX
      SUMRES=SUMRES+RESID**2
 1001 CONTINUE
      WRITE(6,223)K,SUMRES
  223 FORMAT(I4,' EUCLIDEAN DISTANCE IS',F9.1)
      DO 334 LQ=1,N
      FINIT(LQ)=F(K,LQ)
  334 CONTINUE
  201 CONTINUE
      DO 788 IG=1,NPIX
      V(IG)=2.4/(1+(2.4*F(ITER,IG)))
  788 CONTINUE
      IF(SMOOTH.EQ.0.0)GO TO 1820
C ********            SMOOTHING          ******************
C  After smoothing, the solution vector is the array
C          FE which has 171 elements
C Initialize FE(J) to be identical to F(ITER,J)
      DO 6200 IS=1,NPIX
      FE(IS)=F(ITER,IS)
 6200 CONTINUE
C               Pixels with 4 neighbours
C     Weighting factors - W1 and W2
      W1=0.20
      W2=0.20
      IQ1=1
      IQ2=28
```

```
      DO 4000 J=12,20
      FE(J)=W1*F(ITER,J)+W2*F(ITER,J-1)+W2*F(ITER,J+1)
     @+W2*F(ITER,IQ1)+W2*F(ITER,IQ2)
      IQ1=IQ1+1
      IQ2=IQ2+1
 4000 CONTINUE
      IQ1=10
      IQ2=48
      DO 4001 J=26,38
      FE(J)=W1*F(ITER,J)+W2*F(ITER,J-1)+W2*F(ITER,J+1)
     @+W2*F(ITER,IQ1)+W2*F(ITER,IQ2)
      IQ1=IQ1+1
      IQ2=IQ2+1
 4001 CONTINUE
      IQ1=23
      IQ2=72
      DO 4002 J=45,64
      FE(J)=W1*F(ITER,J)+W2*F(ITER,J-1)+W2*F(ITER,J+1)
     @+W2*F(ITER,IQ1)+W2*F(ITER,IQ2)
      IQ1=IQ1+1
      IQ2=IQ2+1
 4002 CONTINUE
      IQ1=43
      IQ2=99
      DO 4003 J=70,94
      FE(J)=W1*F(ITER,J)+W2*F(ITER,J-1)+W2*F(ITER,J+1)
     @+W2*F(ITER,IQ1)+W2*F(ITER,IQ2)
      IQ1=IQ1+1
      IQ2=IQ2+1
 4003 CONTINUE
      IQ1=69
      IQ2=129
      DO 4008 J=98,121
      FE(J)=W1*F(ITER,J)+W2*F(ITER,J-1)+W2*F(ITER,J+1)
     @+W2*F(ITER,IQ1)+W2*F(ITER,IQ2)
      IQ1=IQ1+1
      IQ2=IQ2+1
 4008 CONTINUE
      IQ1=98
      IQ2=154
      DO 4009 J=129,146
      FE(J)=W1*F(ITER,J)+W2*F(ITER,J-1)+W2*F(ITER,J+1)
     @+W2*F(ITER,IQ1)+W2*F(ITER,IQ2)
      IQ1=IQ1+1
      IQ2=IQ2+1
 4009 CONTINUE
C                    Pixels with 3 neighbours
C      Weighting factors WW1 and WW2
      WW1=0.25
      WW2=0.25
      IZ1=13
      DO 4004 J=2,8
      FE(J)=WW1*F(ITER,J)+WW2*F(ITER,J-1)+WW2*F(ITER,J+1)
     @+WW2*F(ITER,IZ1)
      IZ1=IZ1+1
 4004 CONTINUE
```

```
      IZ1=93
      DO 4005 J=122,125
      FE(J)=WW1*F(ITER,J)+WW2*F(ITER,J-1)+WW2*F(ITER,J+1)
     @+WW2*F(ITER,IZ1)
      IZ1=IZ1+1
4005  CONTINUE
      IZ1=129
      DO 4015 J=154,170
      FE(J)=WW1*F(ITER,J)+WW2*F(ITER,J-1)
     @     +WW2*F(ITER,J+1)+WW2*F(ITER,IZ1)
      IZ1=IZ1+1
4015  CONTINUE
      IZ1=116
      DO 4025 J=147,151
      FE(J)=WW1*F(ITER,J)+WW2*F(ITER,J-1)
     @     +WW2*F(ITER,J+1)+WW2*F(ITER,IZ1)
      IZ1=IZ1+1
4025  CONTINUE
      FE(24)=WW1*F(ITER,24)+WW2*F(ITER,24-1)
     @      +WW2*F(ITER,24+1)+WW2*F(ITER,46)
      FE(25)=WW1*F(ITER,25)+WW2*F(ITER,25-1)
     @      +WW2*F(ITER,25+1)+WW2*F(ITER,47)
      FE(11)=WW1*F(ITER,11)+WW2*F(ITER,11-1)
     @      +WW2*F(ITER,11+1)+WW2*F(ITER,27)
      FE(21)=WW1*F(ITER,21)+WW2*F(ITER,21-1)
     @      +WW2*F(ITER,21+1)+WW2*F(ITER,37)
      FE(39)=WW1*F(ITER,39)+WW2*F(ITER,39-1)
     @      +WW2*F(ITER,39+1)+WW2*F(ITER,61)
      FE(40)=WW1*F(ITER,40)+WW2*F(ITER,40-1)
     @      +WW2*F(ITER,40+1)+WW2*F(ITER,62)
      FE(41)=WW1*F(ITER,41)+WW2*F(ITER,41-1)
     @      +WW2*F(ITER,41+1)+WW2*F(ITER,63)
      FE(44)=WW1*F(ITER,44)+WW2*F(ITER,44-1)
     @      +WW2*F(ITER,44+1)+WW2*F(ITER,71)
      FE(65)=WW1*F(ITER,65)+WW2*F(ITER,65-1)
     @      +WW2*F(ITER,65+1)+WW2*F(ITER,92)
      FE(66)=WW1*F(ITER,66)+WW2*F(ITER,66-1)
     @      +WW2*F(ITER,66+1)+WW2*F(ITER,93)
      FE(69)=WW1*F(ITER,69)+WW2*F(ITER,69-1)
     @      +WW2*F(ITER,69+1)+WW2*F(ITER,98)
      FE(95)=WW1*F(ITER,95)+WW2*F(ITER,95-1)
     @      +WW2*F(ITER,95+1)+WW2*F(ITER,124)
      FE(97)=WW1*F(ITER,97)+WW2*F(ITER,68)
     @      +WW2*F(ITER,128)+WW2*F(ITER,98)
      FE(128)=WW1*F(ITER,128)+WW2*F(ITER,97)
     @       +WW2*F(ITER,153)+WW2*F(ITER,129)
C                    Pixels with 2 neighbours.
      WWW1=0.333
      WWW2=0.333
      FE(1)=WWW1*F(ITER,1)+WWW2*F(ITER,2)+WWW2*F(ITER,12)
      FE(9)=WWW1*F(ITER,9)+WWW2*F(ITER,8)+WWW2*F(ITER,20)
      FE(10)=WWW1*F(ITER,10)+WWW2*F(ITER,11)+WWW2*F(ITER,26)
      FE(22)=WWW1*F(ITER,22)+WWW2*F(ITER,21)+WWW2*F(ITER,38)
      FE(42)=WWW1*F(ITER,42)+WWW2*F(ITER,41)+WWW2*F(ITER,64)
      FE(43)=WWW1*F(ITER,43)+WWW2*F(ITER,44)+WWW2*F(ITER,70)
      FE(67)=WWW1*F(ITER,67)+WWW2*F(ITER,66)+WWW2*F(ITER,94)
```

```
      FE(68)=WWW1*F(ITER,68)+WWW2*F(ITER,69)+WWW2*F(ITER,97)
      FE(96)=WWW1*F(ITER,96)+WWW2*F(ITER,95)+WWW2*F(ITER,125)
      FE(126)=WWW1*F(ITER,126)+WWW2*F(ITER,125)
     @       +WWW2*F(ITER,127)
      FE(152)=WWW1*F(ITER,152)+WWW2*F(ITER,151)
     @       +WWW2*F(ITER,121)
      FE(153)=WWW1*F(ITER,153)+WWW2*F(ITER,154)
     @       +WWW2*F(ITER,128)
      FE(171)=WWW1*F(ITER,171)+WWW2*F(ITER,170)
     @       +WWW2*F(ITER,146)
      FE(23)=WWW1*F(ITER,23)+WWW2*F(ITER,24)
     @      +WWW2*F(ITER,45)
C                    Impose bound on smoothed solution..
      DO 1300 IR=1,NPIX
      IF(FE(IR).LT.FMIN)FE(IR)=0.0
 1300 CONTINUE
C   Calculation of residuals of the smoothed picture
      SUMRES=0.0
      DO 1501 L=1,M
      SUMX=0.0
      DO 1502 J=1,N
      SUMX=SUMX+AOR(L,J)*FE(J)
 1502 CONTINUE
      RESID=DTIME(L)-SUMX
      SUMRES=SUMRES+RESID**2
 1501 CONTINUE
      WRITE(6,224)SUMRES
  224 FORMAT(' EUCLIDEAN DISTANCE OF SMOOTHED',
     @       ' PICTURE IS',F9.1)
      DO 1788 IG=1,NPIX
      V(IG)=2.4/(1+2.4*FE(IG))
 1788 CONTINUE
      WRITE(6,634)
  634 FORMAT(/,'SMOOTHED SOLUTION',/)
      DO 5001 IT=1,NPIX
      WRITE(6,566)IT,V(IT)
 5001 CONTINUE
  566 FORMAT(I4,F9.2)
 1820 CONTINUE
      IF(IPLOT.EQ.0) GO TO 1400
C                    Display final solution on the grid.
      CALL PLOTS
      CALL METRIC(0)
      CALL PLOT(1.,2.,-3)
      REDUCE=2.0
      SCALE=0.1/REDUCE
C  Now put the values of the reconstructed velocity at -
C  the positions of the corresponding pixels.....-
C  assign an intensity of shading for each velocity range
C  use subroutine bar of plotlib
C  if using black and white use densities of 280,60,40,25
C  For color use 100(red),100(blue),39,22.
      IDENS1=280
      IDENS2=60
      IDENS3=40
      IDENS4=25
```

```
      FQX=13.*SCALE*DX
      FQY=10.*SCALE*DX
      DO 3910 KS=1,9
      I1=4
      IF(V(KS).GE.1.60.AND.V(KS).LE.1.95)I4=3
      IF(V(KS).GE.1.60.AND.V(KS).LE.1.95)I2=IDENS1
      IF(V(KS).GT.1.95)CALL NEWPEN(3)
      IF(V(KS).GE.1.60.AND.V(KS).LE.1.95)CALL NEWPEN(2)
      IF(V(KS).GT.1.95.AND.V(KS).LE.2.10)I2=IDENS2
      IF(V(KS).GT.2.10.AND.V(KS).LE.2.25)I2=IDENS3
      IF(V(KS).GT.2.25.AND.V(KS).LE.VMAX)I2=IDENS4
      IF(V(KS).GT.VMAX)GO TO 8203
      CALL BAR(FQX,FQY,0.0,DX*SCALE,DX*SCALE,DX*SCALE,I1,I2)
 8203 CONTINUE
      FQX=FQX+DX*SCALE
 3910 CONTINUE
      FQX=11.*SCALE*DX
      FQY=9.*SCALE*DX
      DO 3911 KS=10,22
      I1=4
      IF(V(KS).GE.1.60.AND.V(KS).LE.1.95)I4=3
      IF(V(KS).GE.1.60.AND.V(KS).LE.1.95)I2=IDENS1
      IF(V(KS).GT.1.95)CALL NEWPEN(3)
      IF(V(KS).GE.1.60.AND.V(KS).LE.1.95)CALL NEWPEN(2)
      IF(V(KS).GT.1.95.AND.V(KS).LE.2.10)I2=IDENS2
      IF(V(KS).GT.2.10.AND.V(KS).LE.2.25)I2=IDENS3
      IF(V(KS).GT.2.25.AND.V(KS).LE.VMAX)I2=IDENS4
      IF(V(KS).GT.VMAX)GO TO 8204
      CALL BAR(FQX,FQY,0.0,DX*SCALE,DX*SCALE,DX*SCALE,I1,I2)
 8204 CONTINUE
      FQX=FQX+DX*SCALE
 3911 CONTINUE
      FQX=8.*SCALE*DX
      FQY=8.*SCALE*DX
      DO 3912 KS=23,42
      I1=4
      IF(V(KS).GE.1.60.AND.V(KS).LE.1.95)I4=3
      IF(V(KS).GE.1.60.AND.V(KS).LE.1.95)I2=IDENS1
      IF(V(KS).GT.1.95)CALL NEWPEN(3)
      IF(V(KS).GE.1.60.AND.V(KS).LE.1.95)CALL NEWPEN(2)
      IF(V(KS).GT.1.95.AND.V(KS).LE.2.10)I2=IDENS2
      IF(V(KS).GT.2.10.AND.V(KS).LE.2.25)I2=IDENS3
      IF(V(KS).GT.2.25.AND.V(KS).LE.VMAX)I2=IDENS4
      IF(V(KS).GT.VMAX)GO TO 8205
      CALL BAR(FQX,FQY,0.0,DX*SCALE,DX*SCALE,DX*SCALE,I1,I2)
 8205 CONTINUE
      FQX=FQX+DX*SCALE
 3912 CONTINUE
      FQX=6.*SCALE*DX
      FQY=7.*SCALE*DX
      DO 3913 KS=43,67
      I1=4
      IF(V(KS).GE.1.60.AND.V(KS).LE.1.95)I4=3
      IF(V(KS).GE.1.60.AND.V(KS).LE.1.95)I2=IDENS1
      IF(V(KS).GT.1.95)CALL NEWPEN(3)
      IF(V(KS).GE.1.60.AND.V(KS).LE.1.95)CALL NEWPEN(2)
```

```
      IF(V(KS).GT.1.95.AND.V(KS).LE.2.10)I2=IDENS2
      IF(V(KS).GT.2.10.AND.V(KS).LE.2.25)I2=IDENS3
      IF(V(KS).GT.2.25.AND.V(KS).LE.VMAX)I2=IDENS4
      IF(V(KS).GT.VMAX)GO TO 8206
      CALL BAR(FQX,FQY,0.0,DX*SCALE,DX*SCALE,DX*SCALE,I1,I2)
 8206 CONTINUE
      FQX=FQX+DX*SCALE
 3913 CONTINUE
      FQX=4.*SCALE*DX
      FQY=6.*SCALE*DX
      DO 3914 KS=68,96
      I1=4
      IF(V(KS).GE.1.60.AND.V(KS).LE.1.95)I4=3
      IF(V(KS).GE.1.60.AND.V(KS).LE.1.95)I2=IDENS1
      IF(V(KS).GT.1.95)CALL NEWPEN(3)
      IF(V(KS).GE.1.60.AND.V(KS).LE.1.95)CALL NEWPEN(2)
      IF(V(KS).GT.1.95.AND.V(KS).LE.2.10)I2=IDENS2
      IF(V(KS).GT.2.10.AND.V(KS).LE.2.25)I2=IDENS3
      IF(V(KS).GT.2.25.AND.V(KS).LE.VMAX)I2=IDENS4
      IF(V(KS).GT.VMAX)GO TO 8207
      CALL BAR(FQX,FQY,0.0,DX*SCALE,DX*SCALE,DX*SCALE,I1,I2)
 8207 CONTINUE
      FQX=FQX+DX*SCALE
 3914 CONTINUE
      FQX=4.*SCALE*DX
      FQY=5.*SCALE*DX
      DO 3915 KS=97,127
      I1=4
      IF(V(KS).GE.1.60.AND.V(KS).LE.1.95)I4=3
      IF(V(KS).GE.1.60.AND.V(KS).LE.1.95)I2=IDENS1
      IF(V(KS).GT.1.95)CALL NEWPEN(3)
      IF(V(KS).GE.1.60.AND.V(KS).LE.1.95)CALL NEWPEN(2)
      IF(V(KS).GT.1.95.AND.V(KS).LE.2.10)I2=IDENS2
      IF(V(KS).GT.2.10.AND.V(KS).LE.2.25)I2=IDENS3 /
      IF(V(KS).GT.2.25.AND.V(KS).LE.VMAX)I2=IDENS4
      IF(V(KS).GT.VMAX)GO TO 8208
      CALL BAR(FQX,FQY,0.0,DX*SCALE,DX*SCALE,DX*SCALE,I1,I2)
 8208 CONTINUE
      FQX=FQX+DX*SCALE
 3915 CONTINUE
      FQX=4.*SCALE*DX
      FQY=4.*SCALE*DX
      DO 3916 KS=128,152
      I1=4
      IF(V(KS).GE.1.60.AND.V(KS).LE.1.95)I4=3
      IF(V(KS).GE.1.60.AND.V(KS).LE.1.95)I2=IDENS1
      IF(V(KS).GT.1.95)CALL NEWPEN(3)
      IF(V(KS).GE.1.60.AND.V(KS).LE.1.95)CALL NEWPEN(2)
      IF(V(KS).GT.1.95.AND.V(KS).LE.2.10)I2=IDENS2
      IF(V(KS).GT.2.10.AND.V(KS).LE.2.25)I2=IDENS3
      IF(V(KS).GT.2.25.AND.V(KS).LE.VMAX)I2=IDENS4
      IF(V(KS).GT.VMAX)GO TO 8263
      CALL BAR(FQX,FQY,0.0,DX*SCALE,DX*SCALE,DX*SCALE,I1,I2)
 8263 CONTINUE
      FQX=FQX+DX*SCALE
 3916 CONTINUE
```

```
      FQX=4.*SCALE*DX
      FQY=3.*SCALE*DX
      DO 3933 KS=153,171
      I1=4
      IF(V(KS).GE.1.60.AND.V(KS).LE.1.95)I4=3
      IF(V(KS).GE.1.60.AND.V(KS).LE.1.95)I2=IDENS1
      IF(V(KS).GT.1.95)CALL NEWPEN(3)
      IF(V(KS).GE.1.60.AND.V(KS).LE.1.95)CALL NEWPEN(2)
      IF(V(KS).GT.1.95.AND.V(KS).LE.2.10)I2=IDENS2
      IF(V(KS).GT.2.10.AND.V(KS).LE.2.25)I2=IDENS3
      IF(V(KS).GT.2.25.AND.V(KS).LE.VMAX)I2=IDENS4
      IF(V(KS).GT.VMAX)GO TO 8224
      CALL BAR(FQX,FQY,0.0,DX*SCALE,DX*SCALE,DX*SCALE,I1,I2)
 8224 CONTINUE
      FQX=FQX+DX*SCALE
 3933 CONTINUE
      FNORM=SQRT(SUMRES/FLOAT(M))
      CALL NEWPEN(1)
      CALL SYMBOL(10.*DX*SCALE,20.*DX*SCALE,0.40,'E=',0.0,2)
      CALL NUMBER(10.*DX*SCALE+1.0,20.*DX*SCALE,0.4,
     @            FNORM,0.0,2)
      CALL SYMBOL(10.*DX*SCALE+1.0+2.0,20.*DX*SCALE,
     @            0.4,'MS',0.,2)
      CALL SYMBOL(2*DX*SCALE,16.*DX*SCALE,0.3,
     @            'PIXEL SIZE 4M BY 4M',0.0,19)
      CALL NEWPEN(1)
C  Move the origin at receiver 24 to plot the two ellipses
C  receiver 24 located 2.5 m above the bottom of the well
      CALL PLOT(0.0,2.5*SCALE,-3)
      CALL ELIPS((X01+A1)*SCALE,Y01*SCALE,A1*SCALE,
     @           B1*SCALE,0.0,0.0,360.,3)
      CALL ELIPS((X02+A2)*SCALE,Y02*SCALE,A2*SCALE,
     @           B2*SCALE,0.0,0.0,360.,3)
      CALL NEWPEN(1)
      CALL PLOT(0.0,-2.5*SCALE,-3)
      CALL PLOT(0.0,0.0,999)
 1400 CONTINUE
  660 CONTINUE
      STOP
      END
```

Index

A Seismic tomography experiment, 87

APPENDIX, 151

BIBLIOGRAPHY, 142

Calculation of Q within the steam zone, 128

CHAPTER 1, 5

CHAPTER 2, 23

CHAPTER 3, 87

CHAPTER 4, 118

Computer simulation of the proposed experiments, 36

CONCLUSIONS, 137

Data processing, 103

Engineering aspects of Steam Injection, 14

Geology of the Cold Lake Deposits, 5

Hole to hole seismic profiling, 23

INTRODUCTION, 1, 118

Inversion of the presteam data, 107

Origin of the Oil Sands, 11

Q measurements from the presteam tomography experiment, 118

Spectral Analysis of the recorded signals, 31

Structure of the Oil Sands, 12

The effect of temperature and varying fluid and steam saturations on seismic waves in porous rocks, 18